SPINTRONIC DEVICES FROM CONVENTIONAL AND EMERGING 2D MATERIALS FOR PROBABILISTIC COMPUTING

by

Vaibhav Ostwal

A Dissertation

Submitted to the Faculty of Purdue University

In Partial Fulfillment of the Requirements for the degree of

Doctor of Philosophy

School of Electrical and Computer Engineering

West Lafayette, Indiana

December 2020

THE PURDUE UNIVERSITY GRADUATE SCHOOL
STATEMENT OF COMMITTEE APPROVAL

Dr. Joerg Appenzeller, Chair

School of Electrical and Computer Engineering

Dr. Zhihong Chen

School of Electrical and Computer Engineering

Dr. Supriyo Datta

School of Electrical and Computer Engineering

Dr. Dmitri Nikonov

Intel Corporation

Approved by:

Dr. Dimitrios Peroulis

Dedicated to my beloved parents
Raman Ostwal and Ujwala Ostwal

ACKNOWLEDGEMENT

TABLE OF CONTENTS

LIST OF TABLES

LIST OF FIGURES

ABSTRACT

Novel computational paradigms based on non-von Neumann architectures are being extensively explored for modern data-intensive applications and big-data problems. One direction in this context is to harness the intrinsic physics of spintronics devices for the implementation of nanoscale and low-power building blocks of such emerging computational systems. For example, a Probabilistic Spin Logic (PSL) that consists of networks of p-bits has been proposed for neuromorphic computing, Bayesian networks, and for solving optimization problems. In my work, I will discuss two types of device-components required for PSL: (i) p-bits mimicking binary stochastic neurons (BSN) and (ii) compound synapses for implementing weighted interconnects between p-bits. Furthermore, I will also show how the integration of recently discovered van der Waals ferromagnets in spintronics devices can reduce the current densities required by orders of magnitude, paving the way for future low-power spintronics devices.

First, a spin-device with input-output isolation and stable magnets capable of generating tunable random numbers, similar to a BSN, was demonstrated. In this device, spin-orbit torque pulses are used to initialize a nano-magnet with perpendicular magnetic anisotropy (PMA) along its hard axis. After removal of each pulse, the nano-magnet can relax back to either of its two stable states, generating a stream of binary random numbers. By applying a small Oersted field using the input terminal of the device, the probability of obtaining 0 or 1 in binary random numbers (P) can be tuned electrically. Furthermore, our work shows that in the case when two stochastic devices are connected in series, "P" of the second device is a function of "P" of the first p-bit and the weight of the interconnection between them. Such control over correlated probabilities of stochastic devices using interconnecting weights is the working principle of PSL.

Next my work focused on compact and energy efficient implementations of p-bits and interconnecting weights using modified spin-devices. It was shown that unstable in-plane magnetic tunneling junctions (MTJs), i.e. MTJs with a low energy barrier, naturally fluctuate between two states (parallel and anti-parallel) without any external excitation, in this way generating binary random numbers. Furthermore, spin-orbit torque of tantalum is used to control the time spent by the in-plane MTJ in either of its two states i.e. "P" of the device. In this device, the READ and WRITE paths are separated since the MTJ state is read by passing a current through the MTJ (READ path) while "P" is controlled by passing a current through the tantalum bar (WRITE path).

Hence, a BSN/p-bit is implemented without energy-consuming hard axis initialization of the magnet and Oersted fields. Next, probabilistic switching of stable magnets was utilized to implement a novel compound synapse, which can be used for weighted interconnects between p-bits. In this experiment, an ensemble of nano-magnets was subjected to spin-orbit torque pulses such that each nano-magnet has a finite probability of switching. Hence, when a series of pulses are applied, the total magnetization of the ensemble gradually increases with the number of pulses applied similar to the potentiation and depression curves of synapses. Furthermore, it was shown that a modified pulse scheme can improve the linearity of the synaptic behavior, which is desired for neuromorphic computing. By implementing both neuronal and synaptic devices using simple nano-magnets, we have shown that PSL can be realized using a modified Magnetic Random Access Memory (MRAM) technology. Note that MRAM technology exists in many current foundries.

To further reduce the current densities required for spin-torque devices, we have fabricated heterostructures consisting of a 2-dimensional semiconducting ferromagnet ($Cr_2Ge_2Te_6$) and a metal with spin-orbit coupling metal (tantalum). Because of properties such as clean interfaces, perfect crystalline nano-magnet structure and sustained magnetic moments down to the mono-layer limit and low current shunting, 2D ferromagnets require orders of magnitude lower current densities for spin-orbit torque switching than conventional metallic ferromagnets such as CoFeB.

1. INTRODUCTION

Since 1971, scaling of CMOS transistors have enabled exponential increase in number of transistors per integrated chip[1] consistent with Moore's law and led to better performance in terms of speed and power consumption. Even though advanced CMOS technology node is expected to scale down from current 7 nm to 5 nm or even 3 nm in coming year[2], such scaling is slowing down due to fundamental device physics, increased power densities and economic issues such as difficulties in cost-effective way for production etc[3]. At the same time, amount of data being generated by businesses, media, IOTs etc. is expected to double every two years[4]. Extracting relevant information from gathered data hold promise for achieving new levels efficiencies and products among various sectors such as finance, healthcare, manufacturing processes etc [5]. To this end, artificial intelligence, a branch of computer science has facilitated difficult pattern recognition, learning using large amount of data[6]. However, such data-centric computing is being implemented using von Neumann based computer architecture as shown in Figure 1.1, which separates memory and processing unit[7]. Limited bandwidth and huge energy required for frequent data transfer between the CPU and memory units are some of the limiting factors for efficient data-centric computation[8]. Faced with dual challenges of slow-down of CMOS scaling and emergence of data-centric computing, alternative non-von Neumann computing architectures with physically close processing and memory units such as neuromorphic computing[8], in-memory computing[9] etc have been extensively explored by researchers in recent years. Such unconventional computing systems offer significant benefits in-terms of performance (speed and power) for data-centric computing and has triggered extensive search for novel (i) logic devices such as spiking neurons, oscillators capable of performing more-than-Boolean operations and (ii) memory devices such as analog non-volatile memory which will become building-blocks for unconventional computing systems. Towards that goal, spintronic devices have emerged as potential candidates for both logic and memory units.
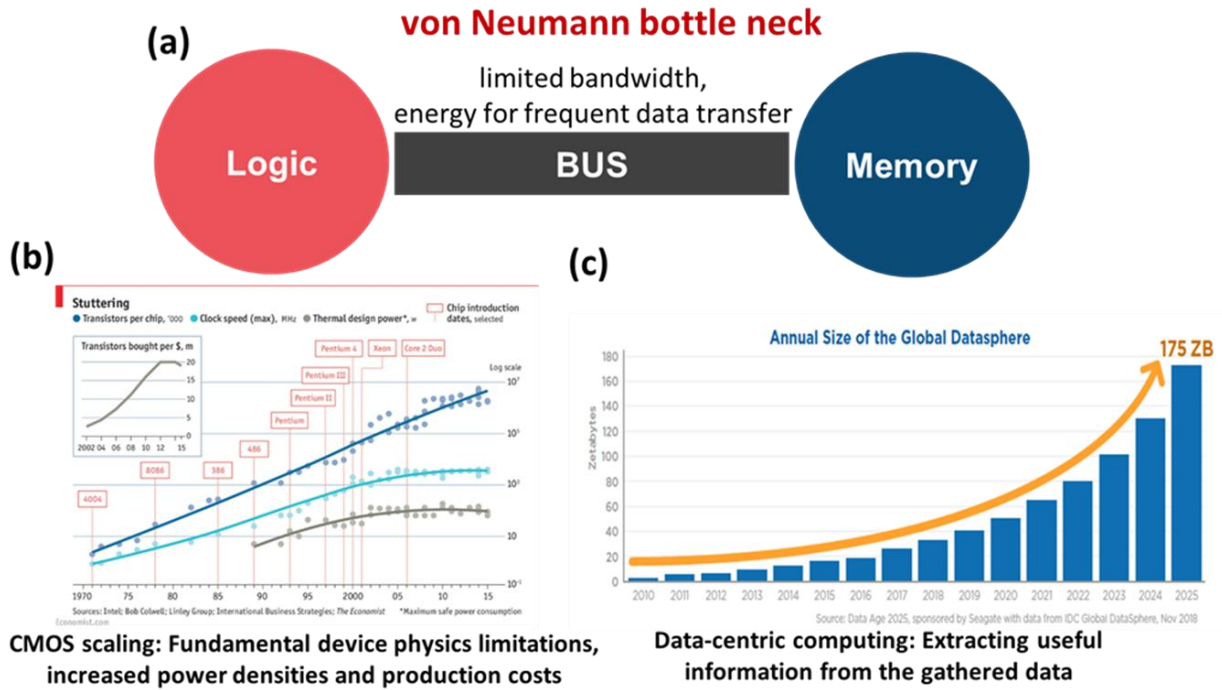
Figure 1.1: (a) von Neumann bottleneck: computer architecture with physically separated logic and memory units is inefficient for data-centric computing (b) Challenges faced by CMOS scaling i.e. logic units in recent years (Sources: Intel; press reports; Bob Colwell; Linley Group; IB consulting; The Economist). (c) Ever increasing data and need for efficient data-centric computing (Source: IDC #US44413318).

The identification of giant magnetoresistance (GMR)[10] and the proposal given by Datta and Das for spin transistor[11] are some of the milestones in 1980's which triggered research interest in the spin-based devices for memory and logic applications. Furthermore, discovery of large TMR with MgO tunneling layers[12], electrical switching of magnetic layer with Spin Transfer Torque (STT) [13] and perpendicular magnetic anisotropy[14] paved the way to realize nano-scale Magnetic Tunnel Junctions (MTJ) offering with advantages such as non-volatility, high endurance and speed[15]. Major semiconductor foundries have already demonstrated capability for volume manufacturing of MTJs integrated advanced CMOS node in STT-MRAM technology. Recently demonstrated spin-orbit torque switching can further increase endurance and speed of MRAM devices with additional benefit of separated WRITE and READ path desired for logic applications[16]. In addition, several proposals have predicted intrinsic physics of such spin-

devices can mimic neural, oscillatory, or synaptic functionalities[17]. This work mainly focuses on experimental demonstration of spin-devices mimicking such functionalities with potential of being building blocks for unconventional computing. In the following section, we will introduce probabilistic spin logic (PSL) proposed by Prof Datta's group[17] and will discuss implementation of device components required for PSL using MRAM type devices. Finally, newly discovered ferromagnetic 2-dimentional materials for future low-power spin-devices will be discussed.

1.1 Probabilistic Spin Logic

Probabilistic spin logic (PSL) is based on concept of probabilistic bits (p-bits) whose output fluctuate between 0 and 1 with probability of output being 0 or 1 is controlled by the input[17] as shown in Figure 1.2(a), unlike conventional CMOS digital bit whose output is deterministically either 0 or 1 depending on the input.
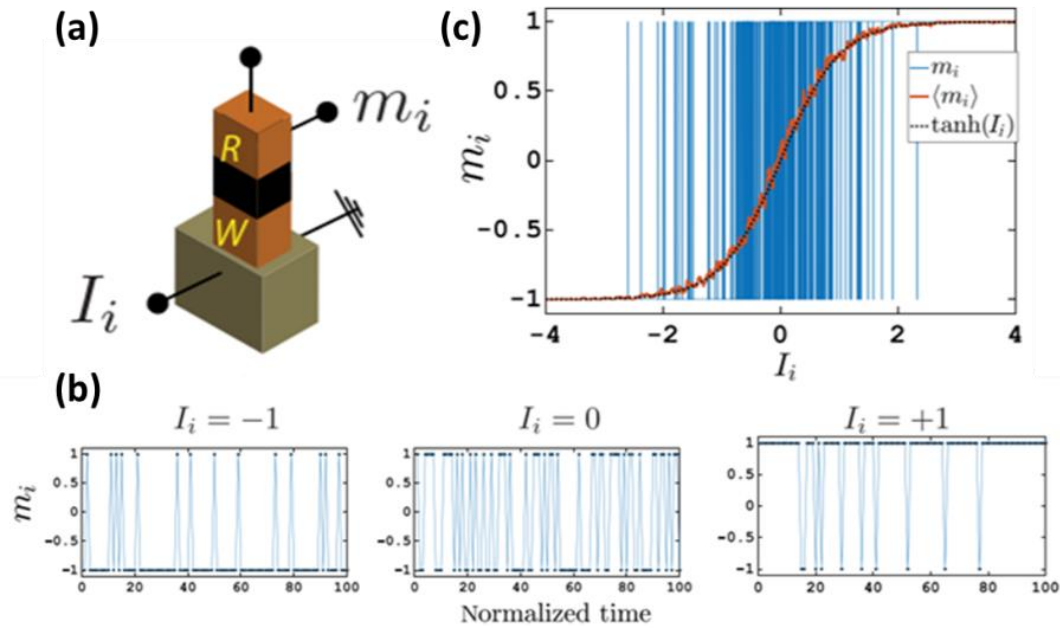
Figure 1.2: (a) Pictorial representation of p-bit consisting I_i controlled WRITE unit and READ unit with the output m_i. (b) For $I_i=0$, p-bit fluctuate between 0 and 1 spending equal time in both states, while (c) The time averaged value of m_i as a function of the I_i shows a sigmoidal curve. (Adapted from [17])

In p-bit, output state m_i is probabilistically controlled by the input bias I_i according to the behavioral equation,

$$m_i = sgn\left\{\tanh\left(I_i\right) + r\right\}$$

where r is a random number uniformly distributed between -1 and 1. Here, we are using bipolar variables $m_i = \pm1$ to represent the 0 and 1 states. From eqn. 1.1, for zero input bias i.e. $I_i = 0$, m_i randomly fluctuates between $+1$ and -1 with equal probability and hence time-average of m_i (represented by $\langle m_i \rangle$) is 0. However, for positive input bias ($I_i > 0$), m_i is more likely to be $+1$ than -1 resulting in $\langle m_i \rangle > 0$ (Figure 1.2(b)), while negative input bias ($I_i < 0$) results in $\langle m_i \rangle < 0$ (Figure 1.2(b)). Overall, as shown in Figure 1.2(c), $\langle m_i \rangle$ is sigmoidal function of input I_i meaning m_i can be pinned to either $+1$ or -1 using strong enough positive or negative bias respectively. Effectively p-bit is a three terminal tunable random generator with important property of input-output isolation analogous to Binary Stochastic Neuron (BSN)[5]. This allows construction of interconnected networks of p-bits according to the equation,

$$I_i = \sum W_{ij}m_j + h_i$$

where W_{ij} is the weight of the interconnect connecting output of jth p-bit to input of ith p-bit and h_i is the local bias. Such p-bit networks [18] (Figure 1.3) with correlated probabilities of p-bits established via weighted interconnects (analogous to synapses) have shown capabilities of Neuromorphic computing [19], Ising computing[20] , Bayesian inference[21] and Invertible
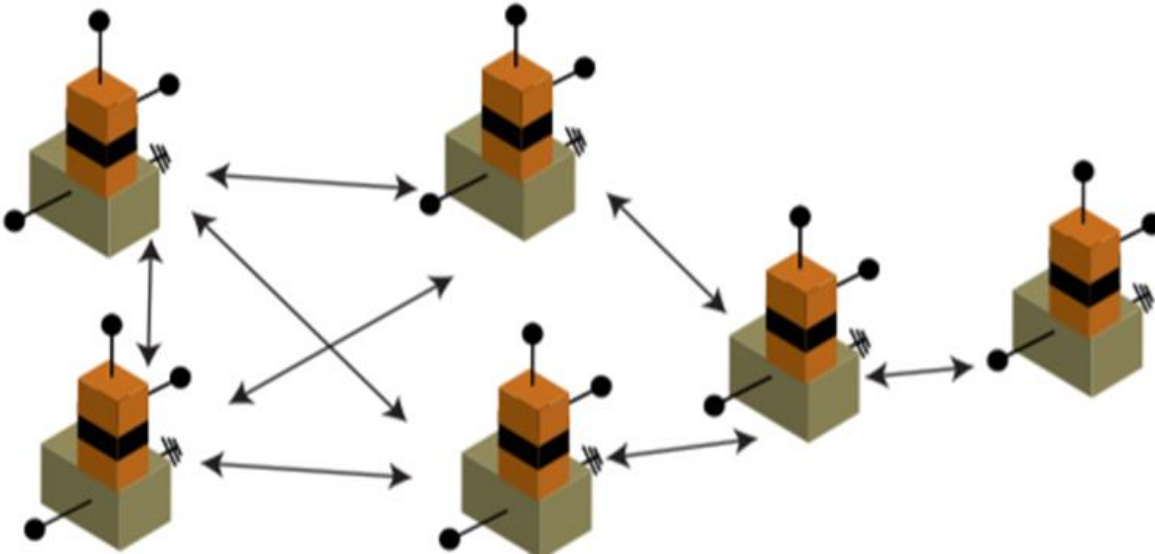
Figure 1.3: Interconnected p-bits (Adopted from [18], © [2020] IEEE): for implementation of Deep Belief Network to solve pattern recognition problems, Bayesian Networks for inference, Ising computer for solving optimization problems and Invertible logic.

logic[22]. In chapter 2, we demonstrate proof-of-concept three terminal spin-device capable of generating tunable binary random numbers with input-output isolation similar to a p-bit. Furthermore, we show correlated probability between two such devices controlled via resistive/weighted interconnect as required for implementation PSL.

1.2 Realization of device components (neurons and synapses) of PSL using stochastic MRAM type devices

A nanomagnet can stay in its magnetization state (either 0 or 1) for an average time period of τ, which is determined by the energy barrier separating those states: $\tau \sim \tau_0 e^{\left(\frac{E_B}{kT}\right)}$, where τ_0 typically has a typical value of few nanoseconds. Meaning, a nanomagnet with barrier of $E_B = 40kT$, will retain its magnetization state (0 or 1) for more than 10 years and can be used for non-volatile memory application. On the other hand, a nanomagnet with barrier of $E_B = 10kT$ would retain its magnetization state only for few $\mu secs$, resulting in random telegraphic fluctuation in time domain. Such control over magnetization retention time by means of energy barrier of a nanomagnet provides an opportunity to realize both p-bits (neurons) and weighted interconnects (synapses) using nanomagnets. For example, magnetization fluctuation in low barrier magnets (LBMs) sensed electrically using MTJ structures can generate time varying voltages which can be
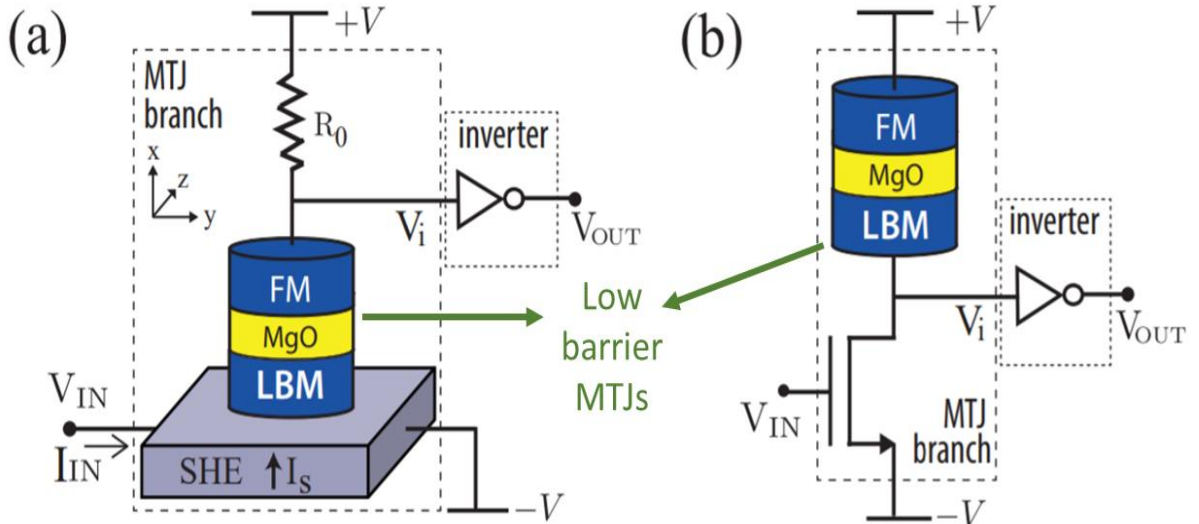
Figure 1.4: Two p-bits/BSN designs using low energy barrier MTJ with fluctuating resistance: (a) using SOT-MRAM type device (b) using STT-MRAM type device. (Adopted from [24], © [2019] IEEE)

used for random number generation. Several proposals have explored implementation of p-bits using such low-barrier nano-magnets in STT-MRAM or SOT-MRAM type devices [22][23][24]. Figure 1.4 shows two of such p-bit designs. By engineering low enough energy barrier, fluctuation rates in low-barrier MTJs can be in sub-nanoseconds timescale[25]. Since STT-MRAM is close to foundry scale production [15] and wafer-scale manufacturability has been shown even for SOT-MRAM[26], realization of neural device (p-bits) using MTJs is highly desirable.
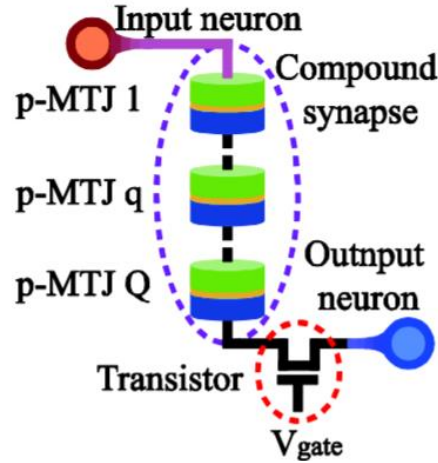
Figure 1.5: Synaptic devices using high barrier MTJs
(Adopted from [28], © [2015] IEEE).

On the other hand, synapses can be implemented using stochastic switching of high-barrier/stable MTJs [27], [28], similar to the one shown in Figure 1.5. Realization of both neurons and synapses using MRAM-type devices allows on-chip integration of p-bits and weighted interconnects for unconventional computing systems similar to the Deep Belief Network proposed in [29] (Figure 1.6). In chapter 3, we experimentally demonstrate SOT controlled low-barrier in-plane MTJ as a compact p-bit as proposed in [22] with isolated READ and WRITE path. In chapter 5, we will discuss progress made towards realizing low barrier out-of-plane MTJs and on-chip integration of CMOS elements required for p-bits. While in chapter 4, we use stochastic nature of SOT switching to realize multi-level synaptic behavior ensemble of stable nanomagnets.
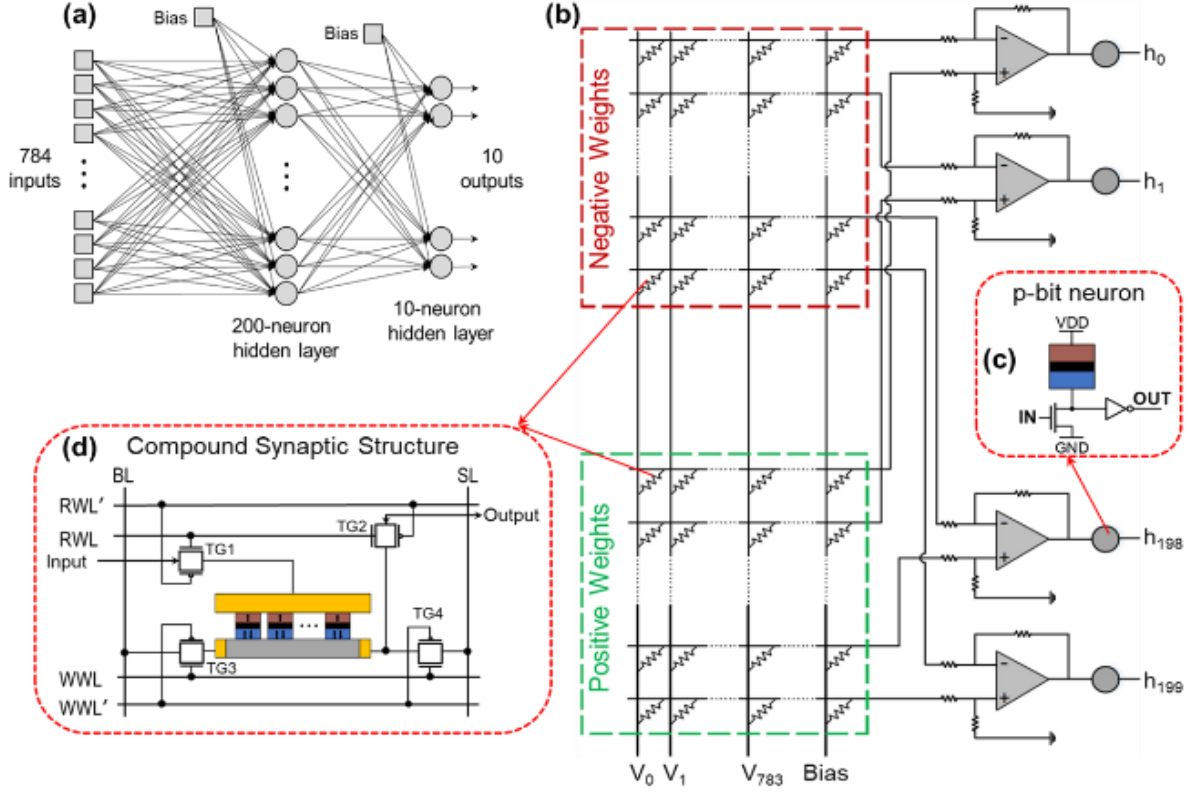
Figure 1.6: (a)&(b) Deep Belief Network using MRAM-type devices with equivalent circuit for the first layer using (c) p-bits as neurons and (d) compound synapses implemented with MRAM cells (Adopted from [28]).

1.3   2D materials for future spin-based devices

While novel spin-devices are being extensively studied for applications in unconventional computing, parallel research thrush is needed to discover novel materials beyond conventional materials to improve spin-devices. For example, improvements in switching speeds, energy consumptions (critical current densities) and read margin (Tunneling MagnetoResistance (TMR)) are essential for wide commercialization of MRAM technology. Hence, alternative material systems with larger TMR[30], spin orbit torques[31] or voltage controlled magnetism[32], are being extensively explored. With recent discoveries such as ferromagnetism[33], spin coupled valley Hall effect[34], long spin diffusion lengths[35] etc., 2-Dimensional (2D) materials have emerged as promising candidates for future spintronics devices.

Since first demonstration of an FET from a 2D semiconductor[36], such low-dimensional materials are being explored to replace silicon in advanced CMOS technology nodes. Properties

such as better electrostatic gate control due to the ultra-thin body of 2D materials and mobilities comparable to silicon have allowed to researchers to scale down transistors down to 1 nm channel lengths[37] with 2D materials. In chapter 4, we will demonstrate integrated 1T1MTJ device structure using 2D-FET.
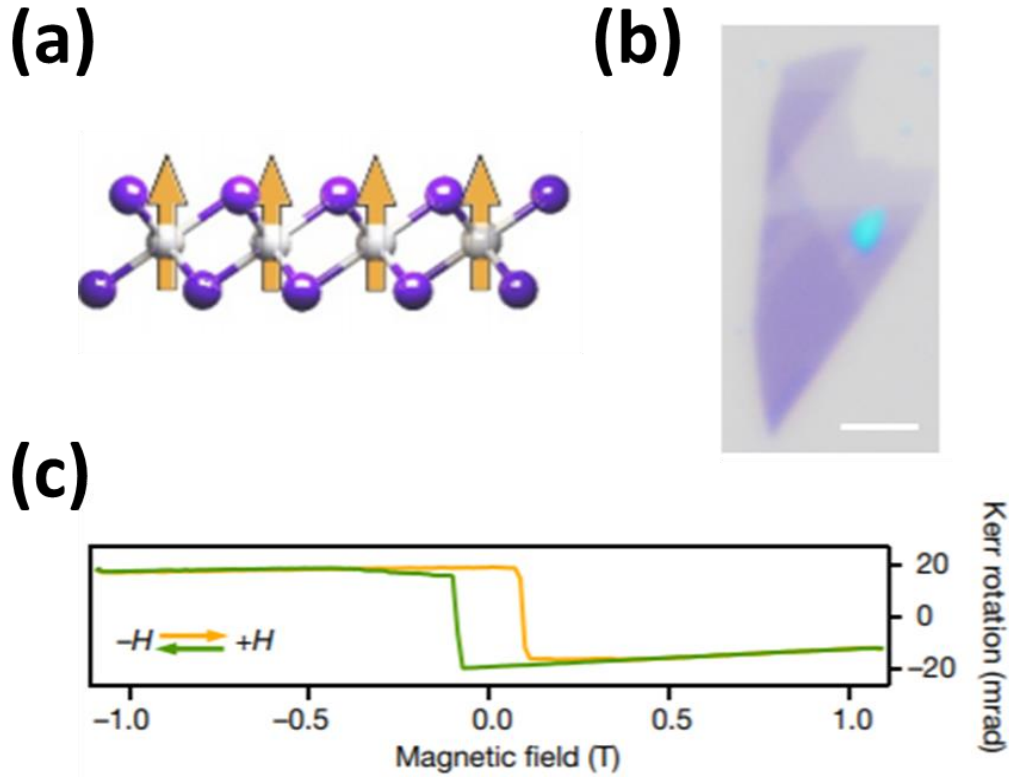
Figure 1.7: (a) CrI$_3$ crystal structure depicting the orientation of magnetic moment. (b) Optical image of a CrI$_3$ flake. (c) Polar MOKE signal of a thin bulk CrI$_3$ crystal. Reprinted with permission from Springer Nature Customer Service Centre GmbH: Bevin Huang et al, "Layer-dependent ferromagnetism in a van der Waals crystal down to the monolayer limit", Nature, 546(7657), 270-273. Copyright © (2017) Springer Nature

Beyond CMOS logic device applications, 2D materials have also shown great promise for implementing non-volatile memory devices for Resistive RAM (RRAM)[38], Magnetic RAM[39] and Ferroelectric Field-Effect Transistors (Fe-FETs)[40]. In 2017, researchers for the first time showed ferromagnetism in thin flakes of 2D materials namely VSe$_2$[41], Cr$_2$Ge$_2$Te$_6$ (CGT)[42] and CrI$_3$[43]. Figure 1.7 shows polar MOKE signal of ferromagnetic CrI$_3$ flake[42]. List of ferromagnetic 2D materials has been growing ever since to include semi-metallic Fe$_3$GeTe$_2$ (FGT)[44], semiconducting CrX$_3$ (X = Br, I)[45], CrSiTe$_3$[46] etc offering diverse magnetic

properties as well. For example, VSe_2 has in-plane anisotropy while $Cr_2Ge_2Te_6$[42] and CrI_3[43] possess perpendicular magnetic anisotropy. Furthermore, magnetic properties of semiconducting 2D ferromagnets such as Curie temperature or anisotropy can be manipulated using electrostatic fields[47]. With their ability to form 2D heterostructures, 2D materials provide unique opportunities to realize not just conventional spintronics devices such as MTJs but also novel logic and memory device concepts. For example, MTJs were experimentally demonstrated using a vdW heterostructure consisting of a FGT/hBN/FGT stack (Figure 4(a)) with FGT as FM and hBN as tunnel barrier[48] while S. Jiang et al. have successfully demonstrated a non-volatile spin-transistor i.e. gate-controlled tunnel conductance[49]. Furthermore, vdW heterostructures such as FGT/hBN/FGT with the perfect crystalline nature and potentially clean interfaces are expected to exhibit much larger TMR ratios (up to ~ 6250%)[50] compared to conventional CoFeB-MgO based MTJs.

Being able to electrically manipulate the magnetic properties in recently discovered 2D ferromagnets is essential for their integration in future spintronics devices. In chapter 5, the magnetization of a semiconducting 2D ferromagnet, namely CGT, is studied using the anomalous Hall effect in CGT/Tantalum heterostructures and we will also show SOT switching of such semiconducting 2D ferromagnet CGT with required switching current densities order of magnitude lower than conventional metal, underscoring potential of 2D materials for future spintronics devices.

2. PROBABILISTIC BIT USING HARD AXIS INITIALIZATION AND CORRELATED PROBABILITIES VIA WEIGHTED INTERCONNECTS

Emerging spintronic devices have recently attracted attention for efficient implementation of more-than-Boolean computational systems such as neural networks[52], Bayesian networks[53][54][55], Ising networks[56][55][57], and invertible logic[58]. Key to the implementation of such systems is the stochastic nature of the network building blocks[59][60][61] - nano-magnets in this demonstration – in response to an external stimulation. The desired output characteristics display a sigmoidal probability to find the nano-magnet in one or the other magnetization state – here as a function of an input current. One approach is to drive the nano-magnet into its metastable state through hard axis initialization and let it relax in the presence of an input current, which determines the probability of the nano-magnet settling to one of the states, $(+m_i)$ or $(-m_i)$[55][62]. Here, we will present proof-of-concept spin-devices that employ SOT for hard-axis initialization and a current induced Oersted field to control their output states. Spin devices using this approach emulate the functionality of a stochastic binary neuron with the average output modelled by equation $y = f(\sum_j w_{ij} x_j + b_i)$, where f is the sigmoidal function, w_{ij} is the synaptic weight corresponding to the input node x_i, and b_i is the default bias. Along this idea, directed networks consisting of spin devices with weighted interconnection can be demonstrated.

In heavy metal (HM)/ferromagnet (FM) systems, spin orbit torque (SOT) switching through the spin Hall effect (SHE) in the HM is an efficient method to control the magnetization of the FM[63]˙[64]. However, since the generated spin is always polarized along the surface plane, magnets with perpendicular magnetic anisotropy (PMA) cannot be deterministically switched. A symmetry breaking in-plane magnetic field is therefore required for SOT switching in HM/ PMA-FM stacks[63]. However, if deterministic switching is not required, currents at levels beyond those typically required for field-assisted switching can drive PMA magnets into their metastable in-plane magnetization states through SOT [65]˙[66]. Once the SOT current is removed, the PMA magnet can relax back to one of the two stable states, $(+m_i)$ and $(-m_i)$, with a 50%/50% probability

in a purely random fashion that is entirely determined by thermal noise. In this way, a true "random number generator" is created. On the other hand, if the SOT current is removed while a small external perpendicular magnetic field is present, a magnetization in the same direction as the applied field will be preferred with a probability distribution determined by the field strength. To generate a local, perpendicular Oersted field, a small metal loop that is isolated through a SiO_2 layer from the nano-magnet is used in our device layout as the input terminal. In this way, input-output isolation is ensured, which is one of the requirements to interconnect building blocks into networks for the applications proposed in[52][55]. In order to show that a spin device is a natural analogue to a stochastic binary neuron, two of these devices are interconnected in this article to form a directed network, and their basic operations are demonstrated.

2.1   Experimental Section

A material stack of Ta(7)/CoFeB(1)/MgO(2)/Ta(2) (numbers in brackets denote the respective film thicknesses in nm) was defined on a Si/SiO_2 substrate using a physical vapor deposition sputter system at a base pressure of $3*10^{-8}$ Torr. The CoFeB thickness of 1 nm was chosen to induce PMA and confirmed by measuring the magnetic moment (M) versus magnetic field (H) loop of an un-patterned film using a SQUID measurement set-up. The film stack was patterned into Hall bars by e-beam lithography using a bilayer resist stack of polymethyl methacrylate (PMMA) and hydrogen silsesquioxane (HSQ), followed by Argon (Ar) ion beam etching down to the SiO_2 surface. Next, elliptical PMA magnets of various sizes ranging from 0.5 um*1.2 um to 1 um*3 um were patterned using the same lithography and etching process as before until the bottom Ta (7 nm) layer was reached. Last, electrical contacts were defined using e-beam lithography and a lift-off process after depositing Ti (20 nm)/Au (100 nm) metal stacks. Figure 2.1(a) shows a scanning electron microscopy (SEM) image of a fabricated device as well as a schematic illustration of the device during the measurement procedure described in the previous paragraph. An elliptical shape was chosen so that the nano-magnet covered the width of the voltage arm entirely and at the same time was located far enough from the edges of the current arm of the Hall bar to minimize the out-of-plane Oersted field due to currents through the Hall bar. To detect the magnetization state of the PMA nano-magnet, the anomalous Hall effect (AHE) is used (Figure 2.1(b)).
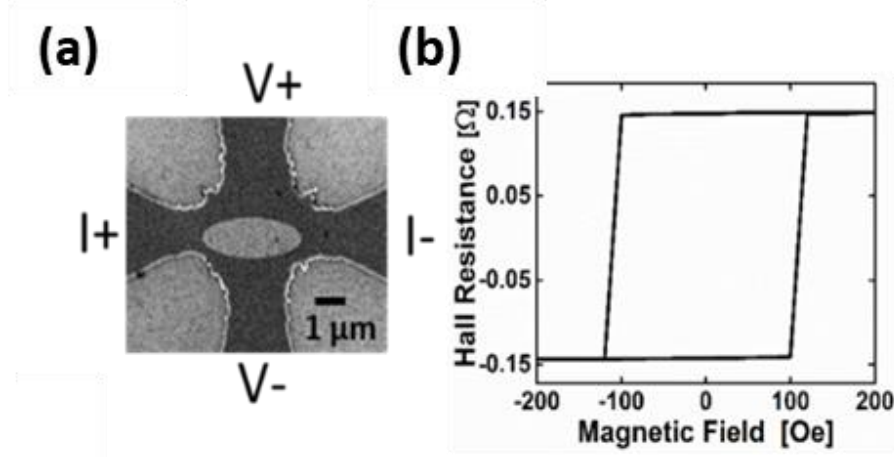
Figure 2.1: (a) SEM image of a fabricated device and (b) Out of plane magnetic field dependent AHE loop.

2.2 Deterministic and probabilistic SOT switching of PMA nano-magnets

SOT driven deterministic switching in the presence of an in-plane field was performed using quasi-static 100 us long dc pulses. The direction of the loop reverses (changes from clockwise to counter clockwise) when the magnetic field polarity is reversed as shown in Figure 2.2, which is a signature of SOT driven magnetization switching[63][67]. On the other hand, in
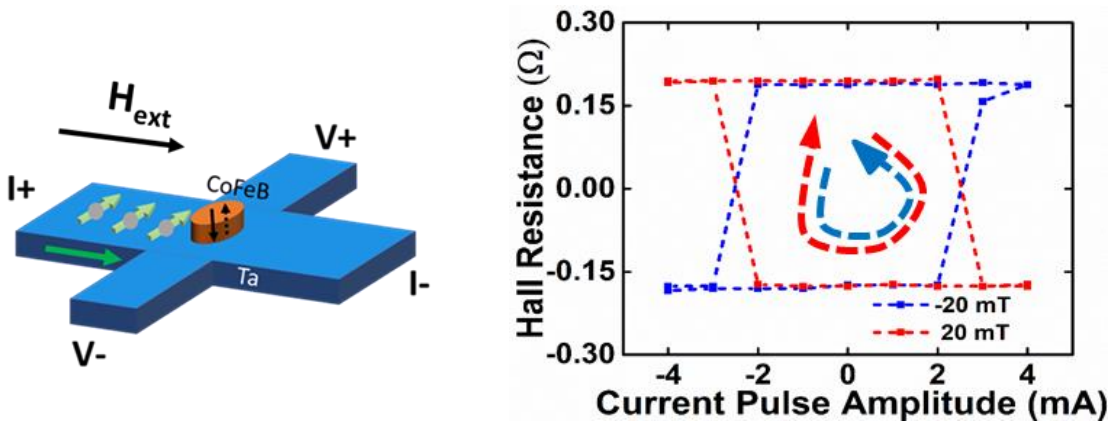
Figure 2.2: Measurement scheme and experimental results for in-plane magnetic field assisted SOT switching of a nanomagnet with PMA. SOT switching of a nanomagnet shows reversal of switching loop for positive and negative in-plane magnetic fields.

the absence of an in-plane magnetic field and with DC current pulses of 7 mA applied on Device 1, the nano-magnet retained its magnetization states with the AHE signal remaining the same after every pulse. This situation changes once the DC current levels reach 8mA (see Figure 2.4(a)). The AHE resistance is found to be positive or negative, corresponding to the magnetization pointing upwards (UP) or downwards (DN), respectively. In this can, SOT pulse pulls the magnetization of PMA nanomagnet in the plane and after removal SOT pulse, nanomagnet settles wither in UP or DN state as shown in Figure 2.3. In fact, performing 81 such measurements, the signal showed 39 times positive and 42 times negative values as shown in Figure 2.4(b), consistent with the expectation of a 50% probability to find the PMA after the SOT pulse in its UP or DN state. Moreover, only two distinct AHE values ($\pm 0.15\Omega$) were detected, implying that the PMA magnet
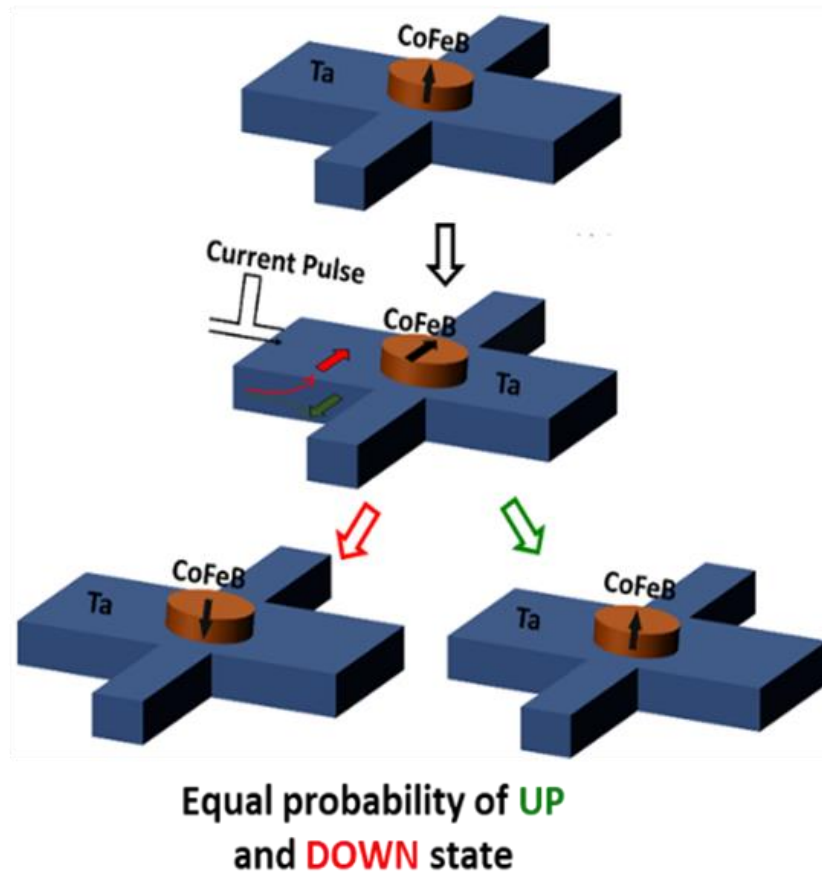
Figure 2.3: Device operation with SOT hard axis initialization.

28
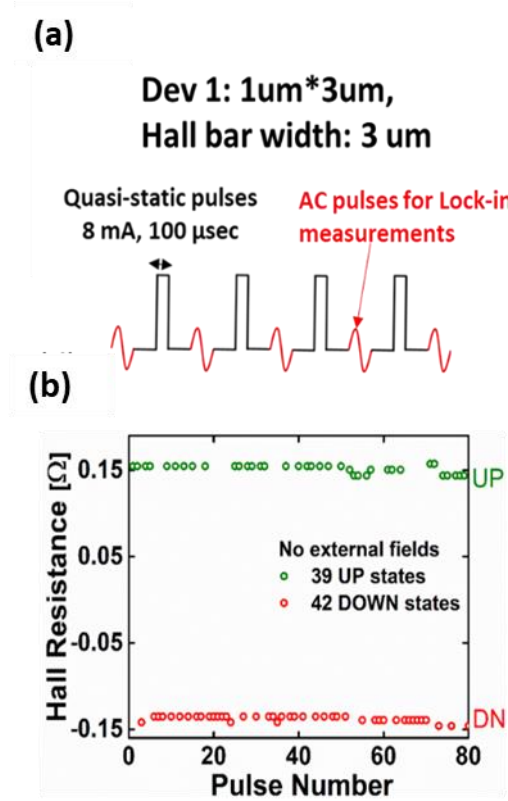
Figure 2.4: (a) Experimental measurement scheme consisting of a quasi-static current pulse through the Hall bar for hard axis initialization, followed by an AC current to measure the magnetization state. (b) Magnetization states of device 1, after each SOT pulse showing its stochastic nature.

responded as a "whole" rather than breaking into multiple magnetic domains during the pulsing procedure.

Figure 2.5 shows the magnetization states of another device (Device 2) with a nano-magnet of size $0.5*1.2$ um^2 after SOT pulses of 5 mA, 5.4 mA, 5.8 mA, and 6.4 mA with no external field applied. Similar to Device 1, a sufficiently large SOT current is needed to achieve the desired stochasticity. It is interesting to observe that the probability of switching (P_{SW}) increases with increasing SOT current amplitude but independent of its polarity. With sufficient statistics, P_{SW} eventually saturates at 50% when the threshold current for the meta-stable initialization is reached[65]. All current levels above this threshold level, generate random binary-states of the PMA magnet[65]. Note that the current required for initializing Device 2 is smaller than for Device 1 due to a smaller Hall bar width. While random choices of the two resistance states are
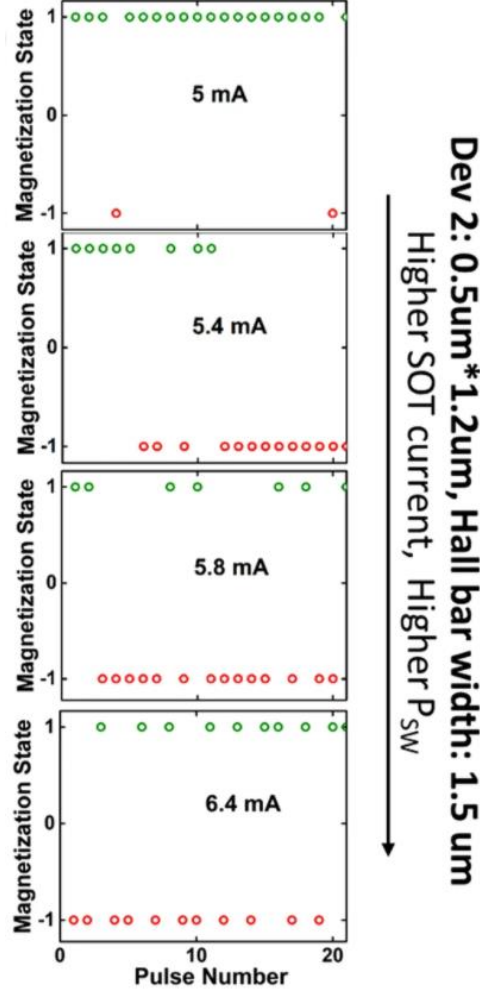
Figure 2.5: Magnetization states of device 2, after each SOT pulse for different current amplitudes in absence of in-plane magnetic fields

demonstrated here, it is understood that in order to apply this scheme to create a true random number generators (RNGs), the "NIST Statistical Test Suite" needs to be satisfied[68]. With the limited data size from our experiments, we are currently unable to perform all NIST tests, but can only employ those that are appropriate for small data sets. Even though we have used electrical pulses of 100 us, due to the details of our measurement set-up, devices can in principle achieve high operational speed and are expected to be able to operate with electric pulses of a few nanoseconds. Also note that other approaches of implementing RNGs, e.g. by means of Spin Transfer Torque (STT) Magnetic Tunneling Junctions (MTJs)[69], require "fine tuning" of individual devices to achieve a 50% P_{SW} and thus are expected to show significant device-to-

device variations. Moreover, MTJ-based devices typically require a "RESET" current pulse for re-initialization. On the other hand, our approach is robust in the sense that even though the threshold current for hard-axis initialization may vary from device-to-device, one can always choose a sufficiently large current to initialize all devices[65]

2.3   Tuning probability of SOT switching via input terminal

Next, the tunability aspect of our RNGs will be discussed. In order to impact the final probability of finding a device in its UP or DN state, a ring shaped Ti (10 nm)/Au (80 nm) metal
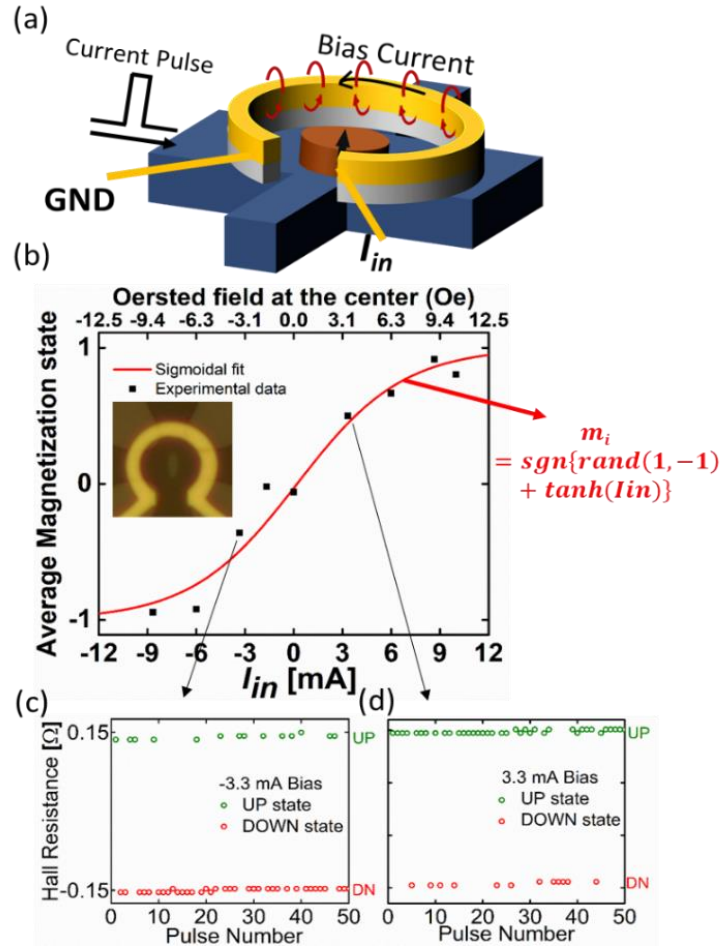
Figure 2.6: (a) Cartoon of an all-electrical device with Oersted field generating metal ring to control the final magnetization state after SOT pulse. (b) Average magnetization state of the device (Dev 1) for different currents (I_{in}) through the Oersted ring. (c) Magnetization states after each SOT pulse for I_{in} = -3.3 mA & +3.3 mA.

loop was designed around the nano-magnet as shown in Figure 2.6(a). This metal loop was isolated from the underlying Hall bar by a 120nm thick SiO_2 layer. Passing current through the loop was employed to generate a symmetry breaking Oersted field, which allows tuning the probability of the final magnetization state after releasing the SOT current. The out-of-plane Oersted field generated at the location of the nano-magnet is approximately given by $\mu_0 I / 2r$ $(eq. 1)$ and was kept "on" during the SOT pulses. ~12 Oe field could be generated by passing 10 mA current through the loop, which was sufficient to entirely pin the magnetization in the UP or DN state with a ~100% probability. Figure 2.6(b) shows the average magnetization (averaging over either 72 or 51 pulses) as a function of the current applied to the loop (I_{in}), displaying the expected sigmoidal shaped curve taking into account more than 600 measured data. Figure 2.6(c) and (d) show exemplary AHE states measured at I_{in} of -3.3 mA and +3.3 mA, which resulted in the respective data points in the main plot. To our knowledge, this is the first demonstration of a current controlled spin device with tunable stochasticity and input-output isolation! To complement the above demonstration, we also performed measurements where the tunability of the RNG was accomplished by means of an external out-of-plane magnetic field rather than the locally generated Oersted field. A schematic illustrating the measurement is shown in Figure 2.7(a). As expected, similar sigmoidal curves of the average magnetization as a function of external magnetic field were obtained for two different magnet sizes. Each data point in Figure 2.7(b) is a result of 41 independent measurements. For the nano-magnet with dimensions of 1um*3um, saturation of the average magnetization occurred at a magnetic field of ~+5/−5 Oe, while a field of +20/−20 Oe was required for the smaller magnet with dimensions of 0.5um*1.2um (Note that in some instances the device characteristics did not show a perfect symmetry relative to zero magnetic field presumably due to a slight misalignment of the nano-magnet relative to the tantalum Hall bar which results in an out-of-plane Oersted). While a perfect quantitative match is not expected, since the magnetic field lines at the nano-magnet location are not identical for the experiment with the Oersted ring and the global external magnetic field, the results in Figure 2.6(b) and 2.7(b) are in reasonable agreement.

To evaluate these findings, time-resolved simulations of mono-domain nano-magnets using stochastic Landau-Lifshitz-Gilbert (sLLG) equation have been performed. Even though for the magnet sizes used in the experiments, the sLLG assumptions, e.g. mono-domain behavior and abrupt "input current turn-of" do not strictly apply, the simulations provide valuable insights into how the sigmoid curve gets effected by magnetic properties such as volume (V), magnetization moment (M_s), and perpendicular magnetic anisotropic field (H_k). As in the experiment, a spin-current pulse is applied for a certain time (dashed red line in Figure 2.7(c)) to drive the magnet into its in-plane hard axis, while a small symmetry. breaking out-of-plane magnetic field is simultaneously applied (green dashed line in Figure 2.7(c)). Figure 2.7(c) shows the dynamic response of the nano-magnet's z-component of the magnetization, m_z, before and after the spin-
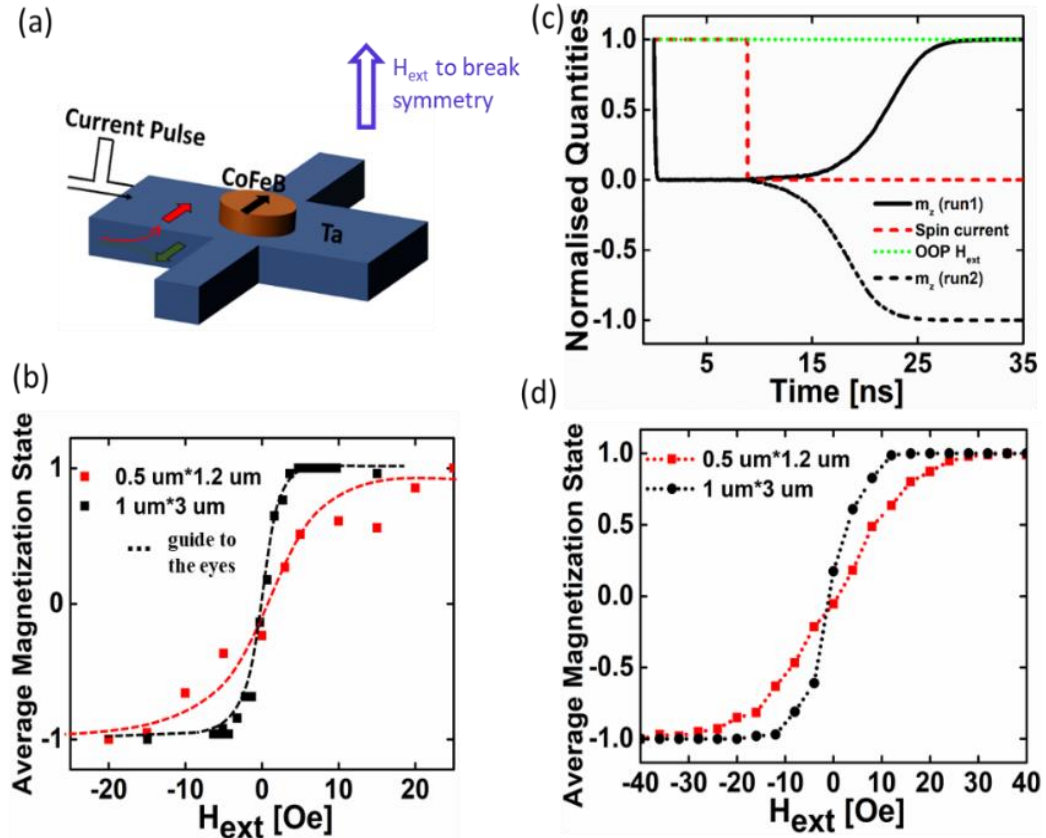
Figure 2.7: (a) Experimental set-up to measure average magnetization under external magnetic field (H_{ext}). (b) Average magnetization state of the device under H_{ext} -impact for two different magnet sizes. (c) sLLG simulations showing the magnetization dynamics. (d) sLLG simulation results for magnets of sizes as shown in (b).

current pulse has been removed. As apparent from the black solid and dashed line, different simulation runs do indeed show that for the same conditions – in terms of symmetry breaking magnetic field – the magnet can settle in the UP or DN state after initially having its magnetization in-plane. However, as shown in Figure 2.7(d) the probability depends critically on the exact H_{ext}-value. Parameters used in the simulation are M_s=1000 emu/cc, H_k=200 mT, nano-magnet thickness (t)=1nm and lateral sizes as shown in the figure legend. Each data point in Figure 2.7(d) represents an average of 200 sLLG simulation runs. Consistent with the experimental findings, smaller nano-magnets require a higher magnetic field to reach the condition that the magnet pins with a 100% probability to one of its two states (UP or DN).

2.4   Directed network for neuromorphic computing

Stochastic spin devices demonstrated above can be employed as stochastic binary neurons to be interconnected to form a neural network – similar to the ones proposed in ref. [70],[71],[72],
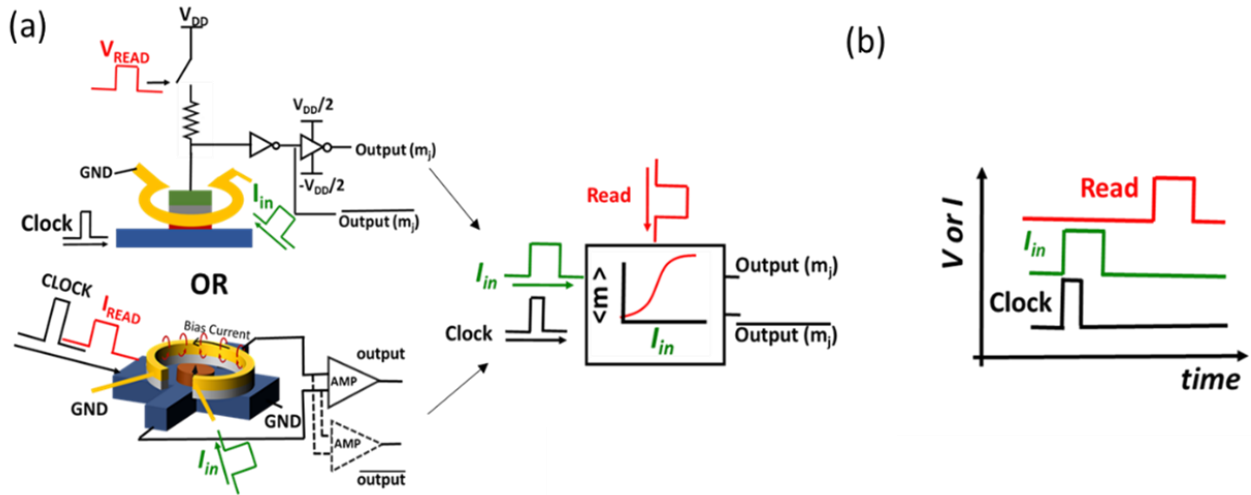
Figure 2.8: (a) Two stochastic spin devices as described in the text used as binary stochastic neurons. (b) Electrical inputs to the stochastic device, i.e. clock, I_{in} and READ.

with its nodal representation shown in in Figure 2.9. In such a network, each node (one spin device) will exhibit a sigmoidal activation function with inputs (in our case provided through the Oersted ring) from the nodes of previous layers as shown in Figure 2.10. Layers will be updated sequentially. Preferably, the magnetization state of the given node will be read using a magnetic tunnel junction (MTJ) in series with two inverters as shown in the top of Figure 2.8. While the

READ operation can also be performed using AHE, as we will demonstrate in the following experiment, it does require voltage amplification due to the relatively low achievable voltage amplitude. Two inverters in series (see Figure 2.8 top) provide $output$ and $\overline{output}$, which are both required to realize positive and negative weights in the network. Electrical inputs, i.e. clock,
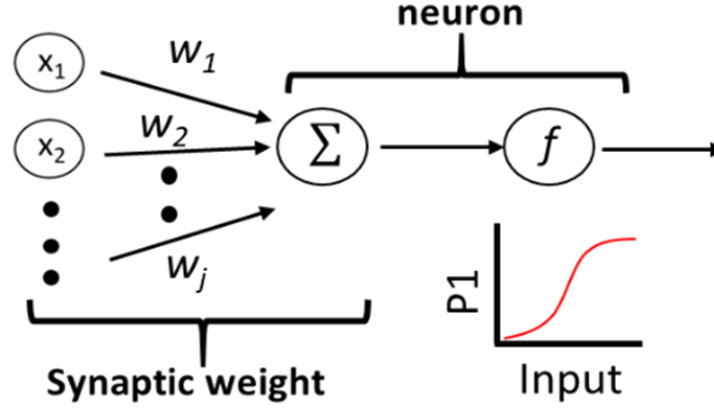
Figure 2.9: Nodal representation of the neural network.

I_{in} and READ of the given node were applied according to Figure 2.8(b). The clock (in our case an SOT pulse) is used to drive nodes (nano-magnets) into their metastable states in the given layer. During the SOT pulse, outputs from previous layers weighted by a resistance network (synaptic weights) are provided to the metal loops of the nodes in the current layer as an input. The input current from node "j" of the previous layer to node "i" of the next layer, connected through the resistance R_{ij} is defined by

$$I_{in-ij} = \frac{m_j * V_{dd}}{R_{ij} + r},$$

where r is the resistance of Oersted ring and m_j is the magnetization state of node j (+1 or -1). For the case of a low resistance Oersted ring (r) as in our experiment, this input current can be approximated as

$$I_{in-ij} \approx \frac{m_j * V_{dd}}{R_{ij}}.$$

Input currents from multiple nodes "j" will be added at the Oersted ring of node "i" providing a total input current of

$$I_{in-i} = \sum_j \frac{V_{dd} * m_j}{R_{ij}}.$$

If comparing this expression with the one for a stochastic binary neuron - $(\sum_j w_{ij} x_j + b_i)$, where w_{ij} is the synaptic weight corresponding to the input node x_j and b_i is the default bias, one

$$I_{in\_i} = V_{DD} * (\pm G_i + \sum_j G_{ij} * m_j) \quad ..eq\ 2$$

$$G_{ij} = \frac{1}{R_{ij} + r} \approx \frac{1}{R_{ij}}$$

$$m_i = sgn\{rand(1, -1) + tanh(I_{in\_i})\} \quad ..eq\ 3$$
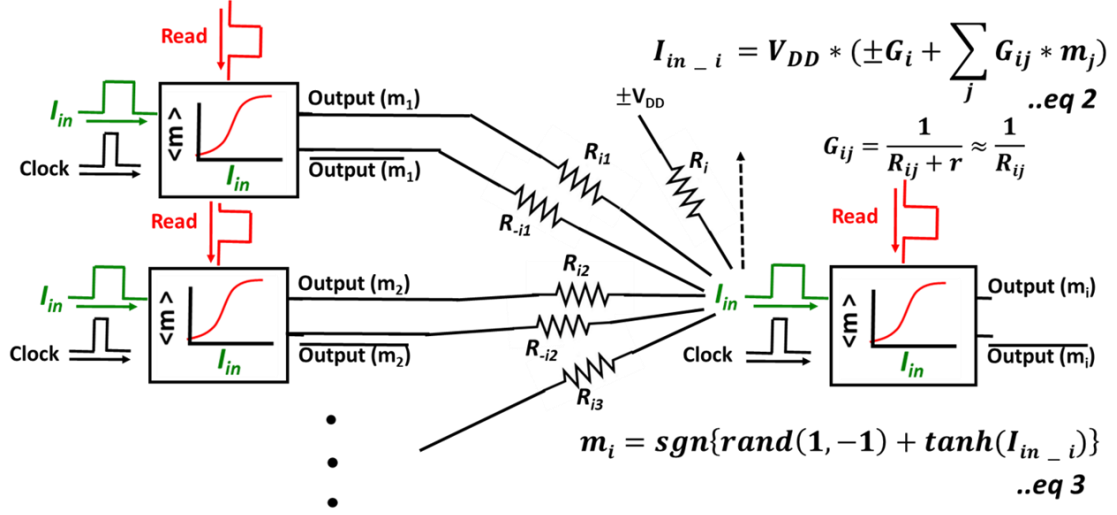
Figure 2.10: Neural network implementation with spin devices as stochastic binary neurons and resistive weight network.

can identify the synaptic weight between two neurons for the network shown in Figure 2.10 as $\frac{V_{dd}}{R_{ij}} = V_{dd} * G_{ij}$. Since both $output$ and $\overline{output}$ are available for the given nodes, negative weights can be realized by using the weight connection corresponding to $\overline{output}$. Equation 2 in Figure 2.10 describes the weighting and summation operation of inputs using the resistor network shown. Equation 3 in Figure 2.10 displays the sigmoidal activation function of the stochastic binary neuron using this weighted input. In principle one can envision more power efficient implementations of the above neurons by employing other spintronic phenomena, such as voltage controlled magnetic anisotropy (VCMA) and Spin Transfer Torque (STT). Compared to SOT, VCMA would potentially require a much lower energy for hard axis initialization of the nano-magnets as proposed in[70], while after the initialization, STT (instead of an Oersted field) could be used to efficiently tune the probability of the final magnetization state[71]. Based on the above neuromorphic system, we have demonstrated a two-node network to show the control of an output node by an input node and a weighted interconnection between them. The experimental set-up of the measurements performed is shown in Figure 2.11 where two stochastic spin devices were used. The input clock 1 was used for hard axis initialization of device N1. After the SOT pulse was
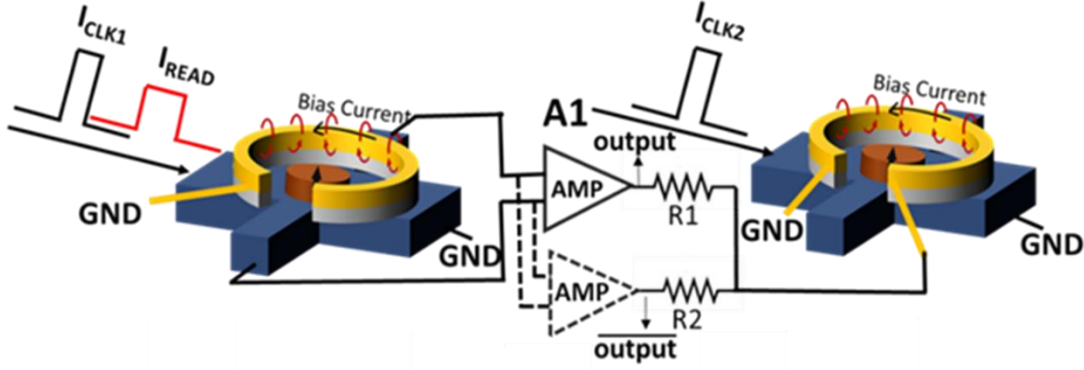
Figure 2.11: Experimental set up for two interacting devices.

removed (after the clocking 1 cycle ended), a small I_{READ} dc current was used to read the magnetization state of N1 using AHE. The AHE voltage corresponding to $\pm m$ is amplified to $\pm V_{dd}$ or $\mp V_{dd}$ using an amplifier A1 or A2, respectively. Next, the amplifier output voltage was applied to the input "Oersted ring" of the second node N2 through a resistor R1 or R2 as shown in Figure 2.11. While I_{READ} was on for node N1, the input clock 2 was applied to node N2 for the hard axis initialization, i.e. a SOT pulse was applied to node 2. Hence, node N2 received an input from the previous node N1 while being in its metastable state.

Using V_{dd} = 10V and R1=810 Ohm and R2=∞ corresponds to a current of ~10 mA in the Oersted ring. This input bias current resulted in a "strong" positive connection between the two neurons – see sigmoidal curve in Figure 2.6(b). Note that any resistance values of around 1000 Ohm will result in a strong connection. In other words, if the input from the previous node is "+1", the connection is strong enough to ensure that node 2 will be found in an average magnetization state of "+1" with a probability close to 100%. A negative weight connection is achieved by using R2=810 Ohm and R1=∞. As explained in the previous paragraph, the strength of the connection can be modified by changing the resistance used for the connection. This is obvious from the case of an infinite resistor R1 and R2 – which means zero weight connection between N1 and N2. Figure 2.12 has the nodal representation of the network for positive weight, negative weight and zero weight connections. As a result, the output of the node N2 is now a function of the input from the previous node N1 and the weight of the connection. For a positive connection, node N2 follows the magnetization state of node N1 as shown Figure 2.12(a) (COPY operation). For clock number 10, N2 doesn't follow the magnetization of N1 which means that the connection strength is not

strong enough to ensure a "perfect" correlation. For a negative weight connection, node N2 follows the opposite magnetization state of node N1 Figure 2.12(b), while for zero weight connection, the outputs of N1 and N2 become uncorrelated as shown in Figure 2.12(c). In other words, the experimental data in Figure 2.12 unambiguously show that the probability (P_{N2}) to find node N2 in a certain magnetization state is dependent on the probability (P_{N1}) of node N1 and the weight of
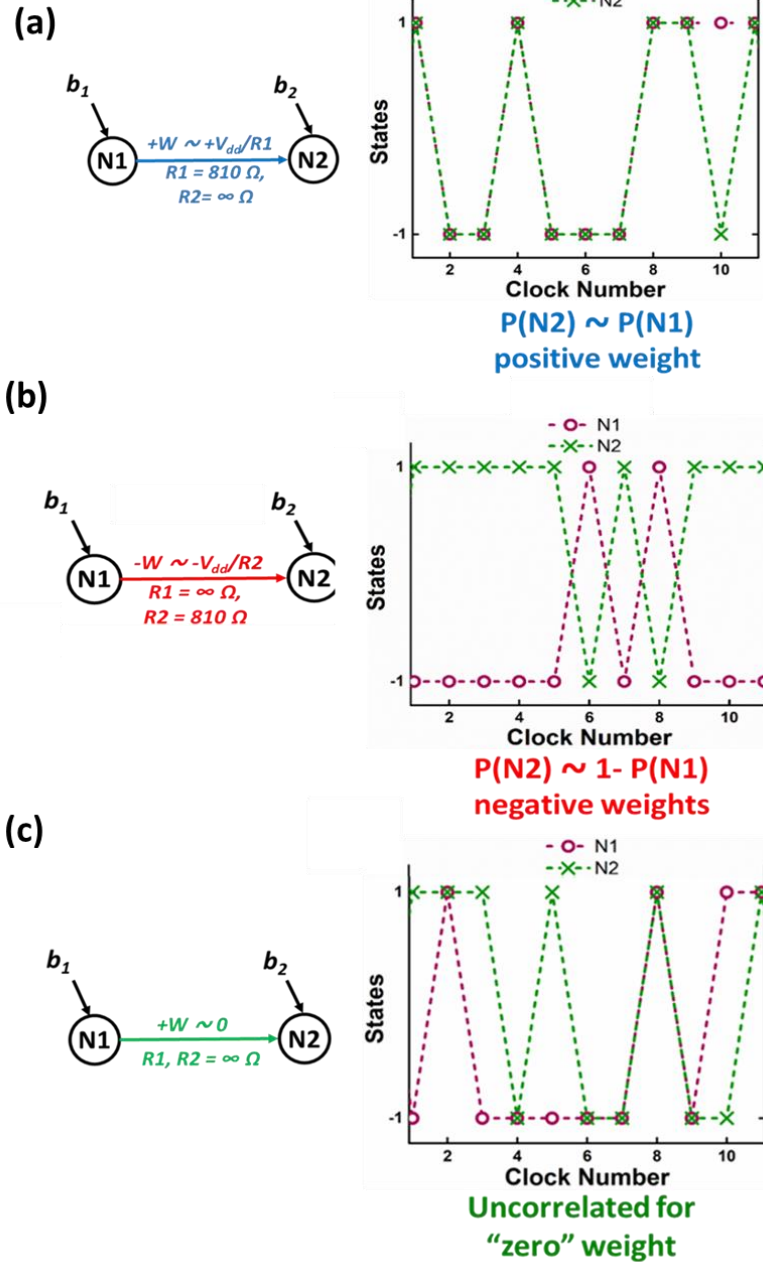
Figure 2.12: Nodal representation and experimental measurements for (a) "+" ve weight, (b) "-" ve weight and (c) 0 weight.

38

the connection. P_{N2} is approximately either P_{N1} or 1 - P_{N1}, depending on whether a strong positive or negative weighted connection is used.

Here we have experimentally demonstrated a new type of stochastic spin devices, which may become the building block for probabilistic computing. The unique properties of our devices, such as a current controlled probabilistic binary output state and input-output isolation can be exploited to perform a weighted summation of multiple input nodes like in stochastic binary neurons. Using these stochastic devices, we have demonstrated a two-node directed network in which the probability of the output node is a function of the input node and the weighted connection between them. This experimental demonstration shows the potential of stochastic spin devices as building blocks for directed networks with probabilistic outcomes such as Neural networks and Bayesian networks.

3. SPIN-ORBIT TORQUE CONTROLLED LOW BARRIER MTJ AS A P-BIT

In the previous chapter, we demonstrated probabilistic bit using hard axis initialization of stable/high barrier nanomagnet. However, to generate each bit of random numbers, current pulses to generate spin-torque and oersted field are required both of which are energy consuming processes. In this chapter, we have experimentally demonstrated that spin-torque control of low-barrier MTJ with device-structure similar to the one used in SOT-MRAM, is an energy efficient and compact way to implement p-bit. In this device, low barrier in-plane MTJ shows random telegraphic "hopping" between <+m> and <-m> magnetization states in time domain. Furthermore, spin orbit torque generated using charge current flowing through Tantalum controls the probability of MTJ being in <+m> and <-m> state. This device naturally provides input-output isolation required for implementation of p-bits due decoupled WRITE and READ path.

3.1 Experimental section

An MTJ stack of Ta/CoFeB/MgO/CoFeB/Ru/CoFe/ PtMn/Ru (Figure 3.1(a)) was sputtered onto a Si/SiO2 substrate using the Singulus Tool at SUNY ALBANY, where the CoFeB/Ru/CoFe stack acts as a synthetic anti ferromagnetic (SAF) fixed layer, while PtMn is an antiferromagnetic layer coupled to the SAF by means of exchange interaction. This stack is similar to the magnetic stack used in STT-MTJs with exchange coupled SAF as fixed layer[20][21], with the difference, however, that for our SOT-MTJs, the free layer CoFeB is located at the bottom of the stack, with a 5 nm Ta layer underneath[22]. MTJs were pattered using a two-step e-beam lithography approach and Ar ion-milling. In the 1st lithography step, the bottom electrode was patterned by etching down to the substrate, while in the second lithography step, the MTJ metal pillar was defined by etching until the bottom Ta layer was reached. The width and length of the Ta-channel are around 3 um

and 12 um respectively. Elliptical MTJs were patterned such that their easy axis is aligned perpendicular to the current flow direction in the Ta underlayer to ensure that no symmetry breaking magnetic field was required for SOT switching [23][24]. 90 nm of SiOx is used to electrically isolate the top and the bottom contact of the MTJs. Finally, contacts were formed using a lift-off process. MTJs were annealed at 300° C for an hour in a low-pressure Helium environment in the presence of an in-plane magnetic field of 1 T collinear with easy axis of the MTJs. DC current pulses or constant DC currents are used for SOT control of the MTJs with a measurement set-up as shown in Figure 3.2(b). Tunneling Magneto Resistance (TMR) was measured directly across the MTJ using an AC current of 2 µA at a frequency of 497 Hz employing lock-in technique with time constants of 10 ms as shown in Figure 3.2(b).
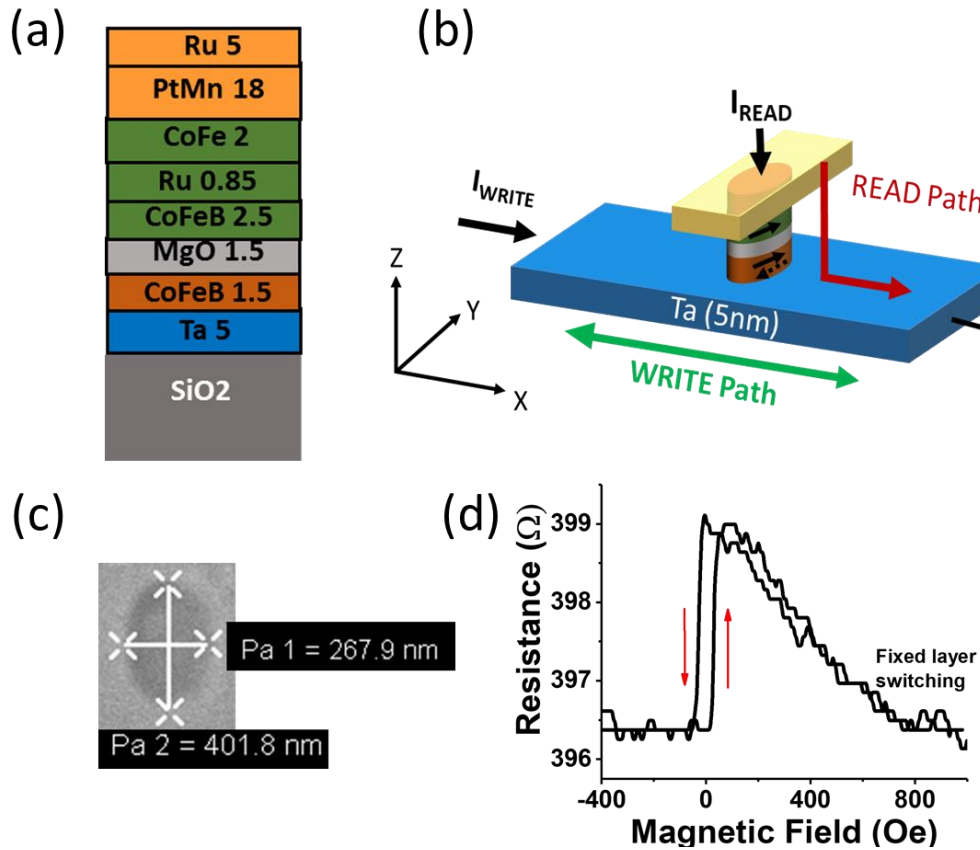
Figure 3.1: (a) Material stack for our SOT-MTJ. (b) Schematic of SOT controlled MTJ. (c) Scanning Electron Microscope (SEM) image of the MTJ and (d) major loop for TMR vs. magnetic field (sweep rate = 480 Oe/min) of device 1. Copyright © [2019] IEEE.

41

3.2 SOT switching of a thermally stable MTJ (device 1)

TMR vs. B-field major and minor loops of a thermally stable MTJ (device 1) (size~260*400 nm^2 shown in Figure 3.1(c)) are shown in Figure 3.1(d) and 3.2 (b). Information about the field sweep rate is provided in the figure caption. The minor loop for this device size exhibits an offset of ~4 Oe. As apparent from the major loop, the MTJ gradually settles to the P state at magnetic fields of around 1000 Oe due to the exchange coupled SAF switching, which is similar to STT-MTJs with exchange coupled SAF layer[74]. Note that our MTJs exhibit relatively low TMR and resistance-area products due to unintentional side wall metal re-deposition during the etching of our MTJ pillars[75]. This side-wall metal re-deposition around the MTJ structures shunts the current from flowing through the tunneling barrier and thus reduces the TMR signal.
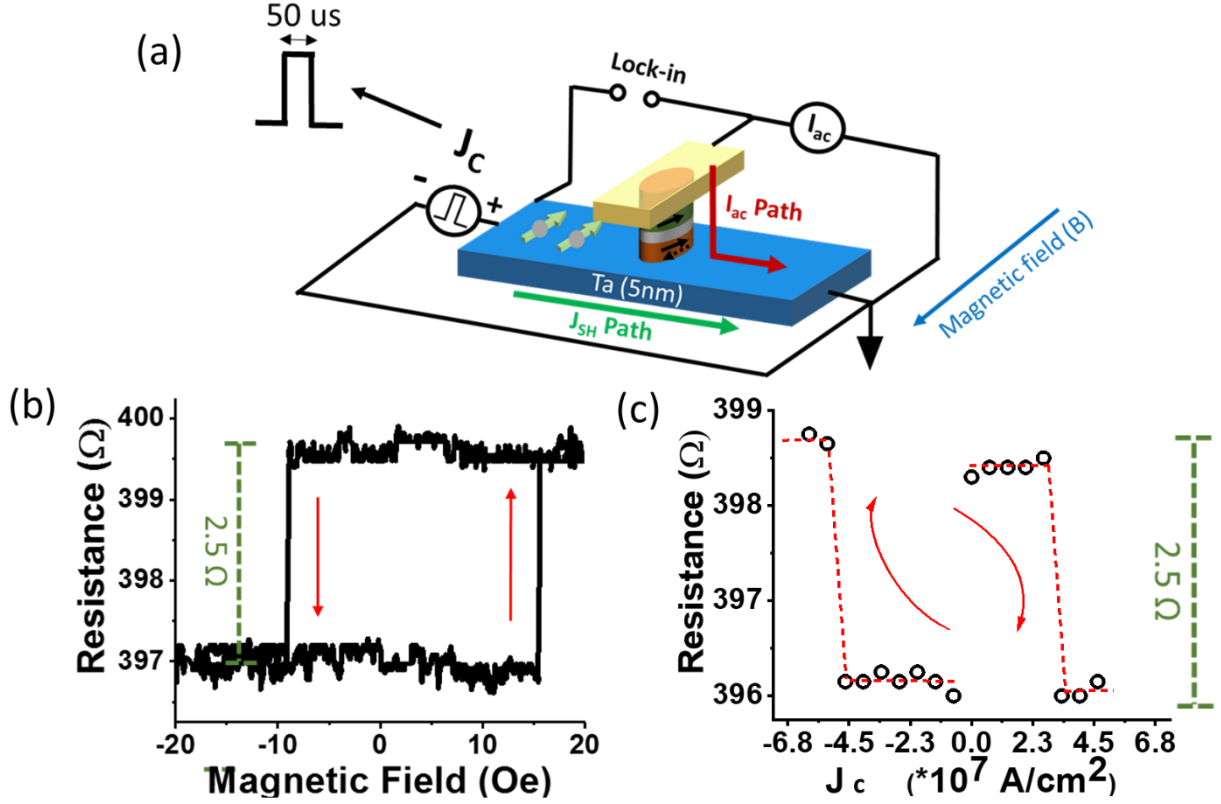
Figure 3.2: (a) MTJ measurement set-up for SOT switching. (b) Minor loop and (c) SOT switching of stable MTJ (device 1) with quasi-static current pulses (50 us wide) showing AP to P switching for positive and P to AP switching for negative current pulses. Copyright © [2019] IEEE.

Next, we used the GSHE in Ta to switch the magnetization of the free CoFeB magnetic layer of the MTJ by passing quasi-static current pulses of 50 us in width through the Ta bottom layer. Figure 3.2(c) shows GSHE current switching in the presence of an in-plane field of 4 Oe to compensate for the small offset observed in the minor B-field loop. The current density is calculated assuming that all current is passing through the 5 nm thick Ta with a channel width of 3 um. In the measurement set-up, positive currents will generate spins in the -x direction and hence a low-resistance parallel (P) state will be preferred by the system. Note that positive current pulses will create positive Oersted fields, and these Oersted fields will try to switch the MTJ to its high-resistance anti-parallel (AP) state. Hence, Oersted fields due to the applied current pulses can be excluded as the reason for the observed MTJ switching. In other words, the polarity of the switching in our experiment is consistent with the expected GSHE effect stemming from the current through Ta. For AP to P switching, the current density required is around $3.5*10^7$ A/cm^2, while P to AP switching requires a current density of around $4.5*10^7$ A/cm^2. To evaluate these numbers, we are calculating the intrinsic critical current density required for GSHE switching according to [76]:

$$J_{c0} = (\frac{2q}{\hbar})\mu_0 M_s t\alpha(H_k^{in-plane} + \frac{M_s}{2})\frac{1}{\Theta_{SHE}} \quad \text{...equation (1)}$$

where M_s is the saturation magnetization moment ($\approx$1100 emu/cc) [63], t is the thickness of the magnet (1.5 nm), α is the damping constant (0.01)[77], $H_k^{in-plane}$ is the in-plane anisotropy field and Θ_{SHE} is the spin Hall angle of Ta ($\approx$0.1)[78]. For the in-plane magnet, the $H_k^{in-plane}$ term can be neglected compared to $\frac{M_s}{2}$ (especially for MTJs with low aspect ratio as used in our experiments). From these numbers we obtain $J_{c0} = 3.46 * 10^7 \frac{A}{cm^2}$ from eq. (1). Considering the quasi-static (pulsed) switching we employed in our experiments, the critical current J_c can be calculated using the standard model for thermally activated switching [75] [76]:

$$J_c = J_{c0}\left[1 - \frac{k_B T}{E_b}\ln\frac{\tau}{\tau_0}\right] \quad \text{....equation (2)}$$

where τ_0 is the attempt time ($\approx$1ns) and τ is the pulse width of the GSHE current used (50 us). For stable MTJs assuming $\frac{E_b}{k_B T} = 40$, J_c is approximately $0.75*J_{c0} = 2.58 * 10^7 \frac{A}{cm^2}$. This value is in good agreement with our experimental findings, considering that any Oersted fields will oppose the SOT switching. We also note that these switching current densities are similar to those previously reported for in-plane MTJs[63][79].

3.3   SOT control of MTJ with low thermal stability (device 2)

Having demonstrated GSHE switching in thermally stable MTJs, we will next discuss similar measurements performed on a second type of MTJ, which has low thermal stability. The size of this MTJ is around $160*260$ nm^2 as apparent from the SEM shown in the Figure 3.3(a), and its smaller size is responsible for the different behavior if compared to device 1. During a slow magnetic field sweep near the minor loop this MTJ toggles between two states (AP and P), exhibiting telegraphic behavior as shown in Figure 3.3(a). The offset in the minor loop for this
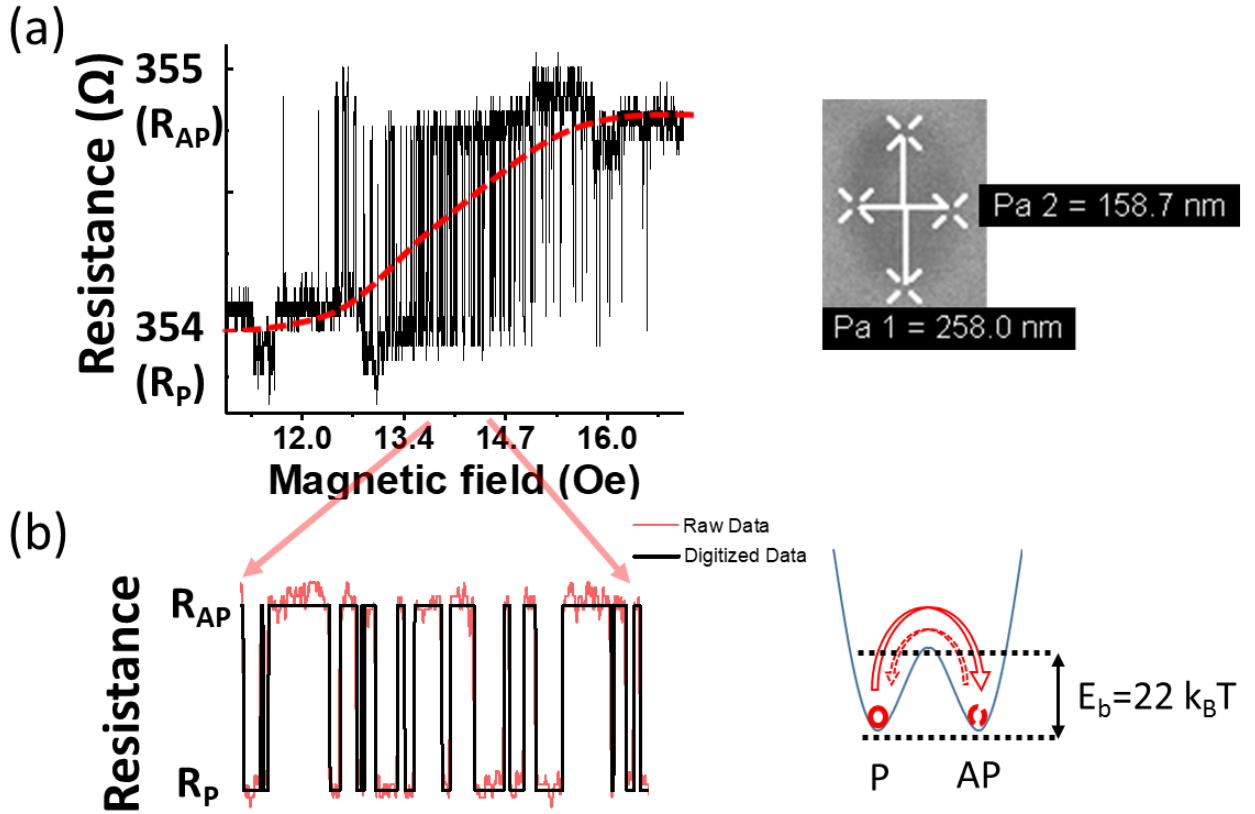
Figure 3.3: (a) Minor B-field loop (sweep rate= 0.4 Oe/min) for a MTJ with low thermal stability (device 2) with the SEM image. When the B-field is swept slowly during the minor loop measurement, the MTJ with low thermal stability shows random fluctuations between the AP and P states. The minor loop offset is around 14 Oe for this device size. (b) Zoom-in minor loop at H_{ext} of 14 Oe (to compensate for the minor loop offset at zero magnetic field) showing telegraphic switching between the AP and the P state (red curve) and digitized data (black curve) to infer the magnetization state of the free layer. Copyright © [2019] IEEE.

device size is around 14 Oe, which is a result of stray fields from the SAF or Neel dipolar orange-peel effect [77]. Figure 3.3(b) shows a zoom-in image of the minor loop at around 14 Oe with two distinct resistance states AP and P respectively. Note that the black line is a digitized version of the raw data. The sweep rate used for the minor loop measurement was 0.4 Oe/min. The MTJ under
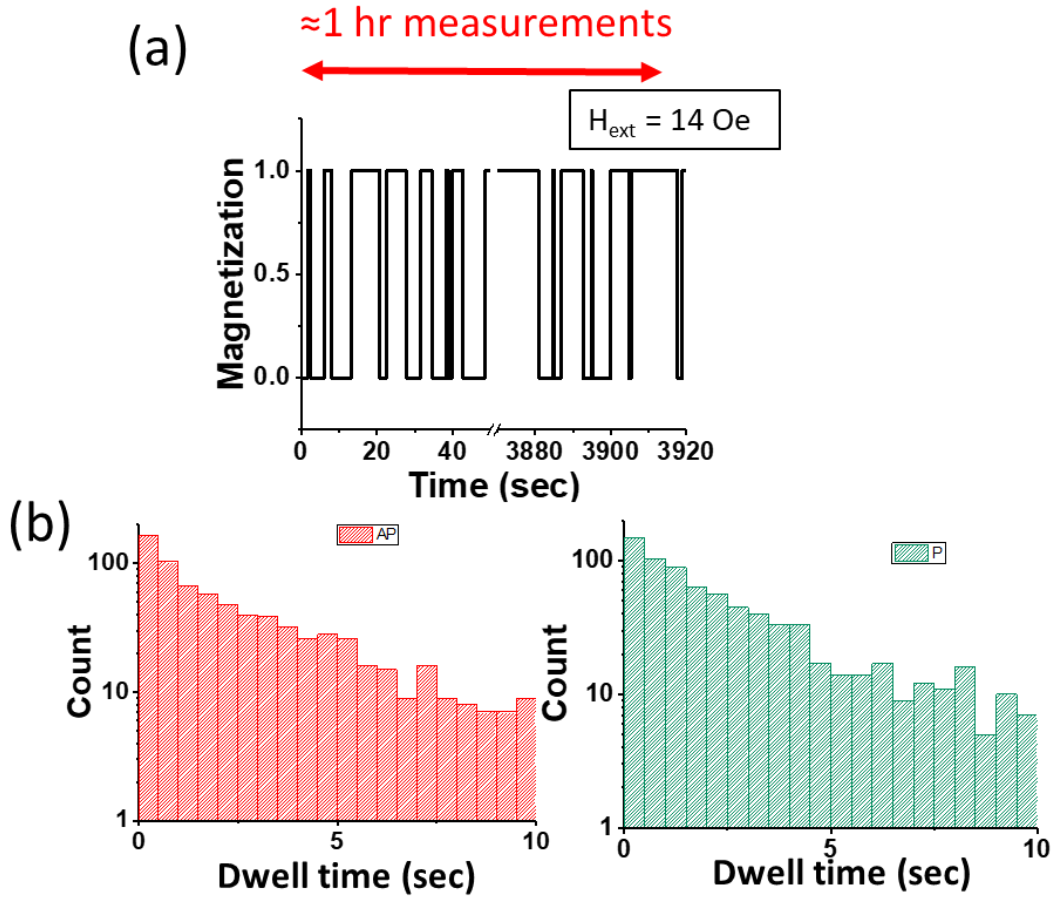
Figure 3.4: (a) Magnetization states obtained during near 1hr measurements at H_{ext}=14 Oe. (b) Obtained number of counts vs lifetime for AP (Red) and P (Green) states in semilog plot using measurement in (a). At H_{ext} = 14 Oe, sMTJ has equal characteristic lifetime for AP and P states. Copyright © [2019] IEEE.

investigation is in its P state for magnetic fields < 10 Oe and in its AP state for fields > 17 Oe. Random telegraphic switching between the AP and P state is expected to follow a Poisson distribution with respect to the dwell time, i.e. the time the MTJ stays in either of the two states and should exponentially decrease. To perform such a dwell time analysis, the MTJ resistance was characterized for over an hour at an external field of 14 Oe. Next, the magnetoresistance data are

digitized to +1 and 0 (Figure 3.4(a)) by applying a proper threshold operation to the TMR data as displayed in Figure 3.3(b). At an external field of 14 Oe, the probability for the MTJ to be in its AP versus P state is found to be ~50 %. Figure 3.4(b) displays the number of counts for a dwell time in a semi-logarithmic plot. From the linear fit to this plot a characteristic lifetime to find the MTJ in its P (τ_P) and AP (τ_{AP}) state of around 3 sec is found for both τ_P and τ_{AP}. Using this experimental finding, an energy barrier ($\Delta_{in-plane}$) of ~22 k_BT can be determined from $\tau = \tau_0 exp \left[\frac{\Delta_{in-plane}}{k_BT} \right]$. We also observed a clear temperature dependence of switching rates in our device as shown in Figure 3.5(a), (b) and (c) below. The average switching times of the device at 290 K, 300 K and 320 K are approximately 4 sec, 3 sec and 1.2 sec respectively.
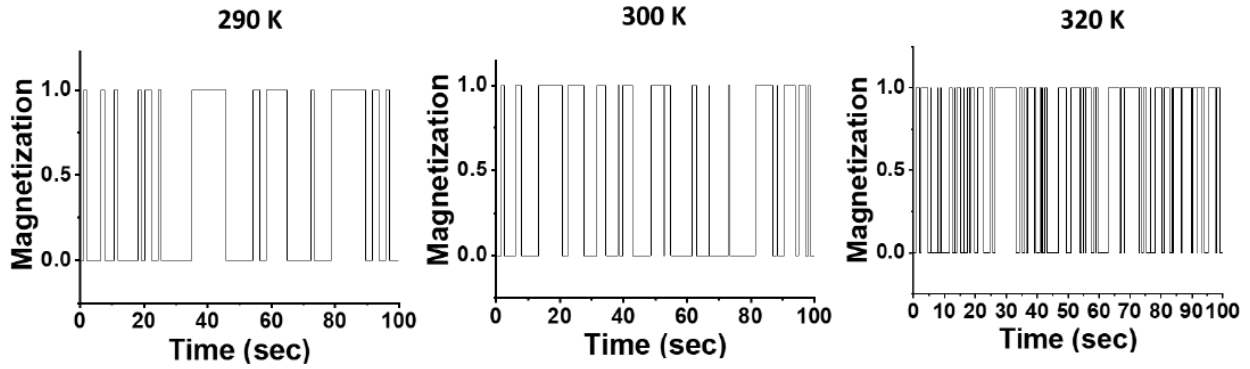
Figure 3.5: (a) Magnetization states obtained at H_{ext} =14 Oe for temperature of (a) 290 K (b) 300 K and (c) 320 K.

Next, tests from the National Institute of Standards and Technology (NIST) Statistical Test Suit (STS) [68] are performed based on the above experimental magnetization data that was used for the dwell time analysis in Figure 3.4(b) . Since, $\tau_P = \tau_{AP} = 3$ sec, magnetization states are read after each 6 sec (2τ) for the NIST tests. Note that some of the tests in the suit are not applicable due to the limited sample size (~650 samples) in our case. Table 3.1 shows the test name and the respective p-values obtained for the test on the raw data and after performing an XOR operation used to increase the Shannon entropy [80] and hence the randomness. If the obtained p-value is greater than 0.01, the sample is considered to have passed the test. As shown in table 2, already the raw data obtained from the magnetization states of our stochastic, i.e. MTJ with low thermal stability passes all the test performed (shown in green) except one (shown in red), while data after XOR

46

Table 3.1: NIST STS randomness test and results (p-values) obtained from measuring the MTJ with low thermal stability at 14 Oe (sample size~650 samples). If a p-value greater than 0.01 is obtained, the test has been successfully passed. Copyright © [2019] IEEE.

Randomness test name	P-value without XOR	P-value after XOR
Frequency test	0.272095	0.753684
Frequency test within block	0.651978	0.938924
Runs test	0.659677	0.100225
Longest runs test	0.002909	0.628936
Binary matrix rank test	0.375518	0.834948
Discrete Fourier transform	0.652767	0.087321
Serial test 1	0.010302	0.015907
Serial test 2	0.034779	0.068169
Approximate Entropy test	0.028691	0.025147
Cumulative sums test forward	0.509393	0.315833
Cumulative sums test backward	0.155112	0.168758

operations passes all the randomness tests performed. As discussed before, both: i) magnetic fields and ii) SOT can deterministically switch high barrier nano-magnets (see discussion around Figure 3.2). In the case of MTJ with low thermal stability, magnetic fields and SOT are thus expected to tune the probability of a low barrier MTJ to be found in its AP or P state. To increase the speed of telegraphic switching the temperature was raised to 320 K in this experiment. Next, the MTJ resistance was monitored while passing a DC current ranging from -250 μA to 200 μA through the Ta layer in the presence of a magnetic field of 14 Oe to compensate for the offset of the minor loop. Further optimization of the SAF layer will be required to remove such offset in the minor loop and achieve field-free operation in the future. The telegraphic switching of this MTJ for different DC currents flowing through the Ta layer is shown in Figure 3.5(a). The voltage drop across the MTJ is not affected by the DC currents flowing through the Ta layer due to the three-terminal nature of SOT devices. Only currents flowing through the MTJ determine the voltage drop across the MTJ, which is essential for a proper implementation of p-bits [5]. For positive DC currents the MTJ prefers to stay in its P state while negative DC currents result in a higher probability to find the system in its AP state. This preference is consistent with the deterministic switching of thermally

stable magnets (see Figure 3.2(c)) and agrees with the sign of the SOT generated by the Ta. Again, note that Oersted fields would result in exactly the opposite tuning compared to the SOT by the Ta layer.

(a)   **(b)**
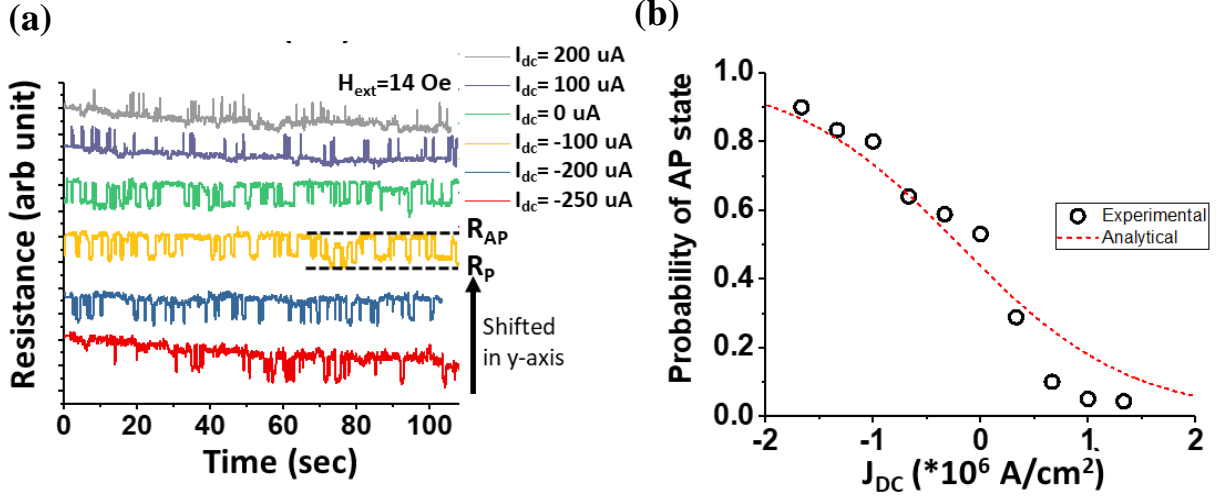
Figure 3.6: (a) MTJ with low thermal stability resistance data showing telegraphic switching between the AP and P state for H_{ext} = 14 Oe and different Idc flowing through the GSHE Ta layer. (b) The probability for the MTJ with low thermal stability to be found in its AP state versus current density flowing through Ta (black circles) based on data from (a) and expected probability obtained using the analytical expression eq. 3 (red curve). Copyright © [2019] IEEE.

Last, we want to compare our experimental results on the SOT impact with the expectation to find the system as a function of the current through the Ta layer in its AP state. For this, the resistance values obtained for various DC currents were digitized, and the probability of the MTJ to be in its AP state is calculated from the experimental data. Figure 3.5(b) shows this probability as a function of the amount of current flowing through the Ta Hall bar structure, clearly showing a sigmoidal shape, which starts saturating around 250 µA. This current corresponds to a density of $1.7 * 10^6$ A/cm². For MTJ with low thermal stability, the characteristic lifetime of the P or AP state in the presence of a spin current is given by[77][81],

$$\tau_{P,AP} = \tau_0 exp\left[\frac{\Delta_{in-plane}}{k_B T}\left(1 \mp \frac{J}{J_{c0}}\right)\right] \quad ....equation~(3)$$

where J_{c0} is the characteristic critical current density $J_{c0} = 3.46 * 10^7 \frac{A}{cm^2}$, which was calculated before, while $\Delta_{in-plane}$=22*k_BT. Hence, for the input current density J, the probability to find the MTJ in its AP state is given by $\frac{\tau_{AP}}{\tau_P + \tau_{AP}}$. The sigmoidal curve obtained from this analysis is plotted in Figure 3.5(b) and matches closely the experimentally obtained data. In conclusion, we

have successfully demonstrated that MTJs with low thermal stability are natural candidates as RNG, while spin currents can be used in an efficient way to tune such low barrier MTJs and hence provide a compact device that is capable to operate as a tunable RNG.

4. TOWARDS P-BITS WITH EMBEDDED MTJ

In previous chapter, we implemented p-bit using spin-orbit torque controlled low barrier MTJ. However, p-bit can also be implemented using 2-terminal MTJ with a randomly switching free layer connected to the drain of a conventional transistor (T). P-bit implemented using such 1T/1MTJ structure is analogous to the ones used in STT-MRAM technology and better alternative to p-bit implemented using SOT controlled low barrier MTJ. In this chapter, we will report progress made towards realization of such p-bit with on-chip 1T/1MTJ structure. We will first demonstrate successful fabrication of PMA-MTJ with high TMR. We will also show preliminary results on fabrication of MTJ and 2-D transistor on same chip and their integration in 1T/1MTJ structure.
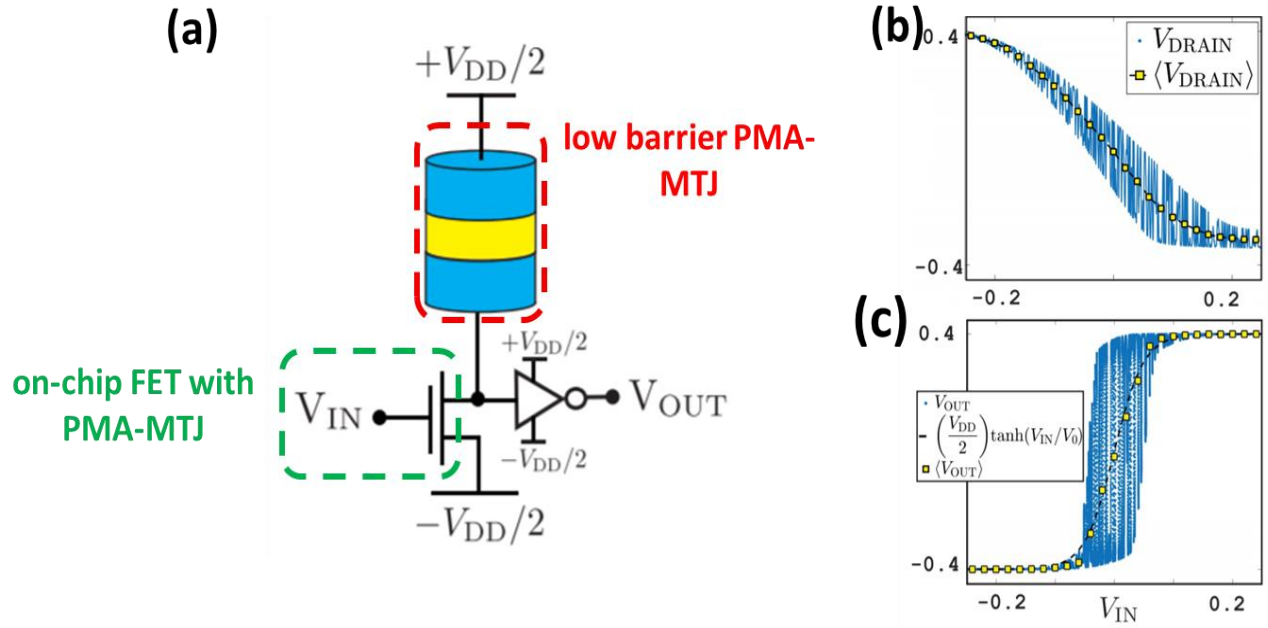
Figure 4.1: (a) P-bit with embedded MTJ. (b) Output voltage at the transistor-drain as a function of gate voltage (V_{in}). (c) Output voltage at the output node (V_{out}) as a function of gate voltage (V_{in}). (Adapted from [23]). Copyright © [2019] IEEE.

4.1   Introduction

One of the proposals for implementing p-bits consists of low barrier MTJ connected in series with transistor as shown in Figure 4.1 (a) which is similar to the structures used in STT-MRAM technology. In such structure, if conductance of transistor (NMOS) for $V_{in} = 0$ is similar to the conductance of MTJ, fluctuations in magnetization of low barrier MTJ will be converted to voltage fluctuations at the output (V_{out}). However, with $V_{in} < 0$, the transistor is OFF and V_{out} is pinned to $-V_{dd}/2$ independent of the magnetization fluctuation of the MTJ. On the other hand, with $V_{in} > 0$, the transistor is ON and V_{out} is pinned to $+V_{dd}/2$ independent of the magnetization fluctuation of the MTJ. Overall, average of fluctuating V_{out} ($<V_{out}>$) is sigmoidal function of Vin as shown in Figure 4.1 similar to a p-bit. To implement such p-bit, one requires low barrier MTJ with good TMR so that voltage fluctuation at the V_{drain} are large enough to be amplified by the inverter. To achieve such MTJ, we will first show successful fabrication of nanoscale stable PMA-MTJ with TMR > 60% and then study annealing recipe for PMA-MTJs as a tool to control it's magnetic anisotropy i.e. energy barrier. We also need on-chip transistor with conductance in ON state (G_{ON}) to be much larger than average conductance of MTJ and conductance in OFF state (G_{OFF}) to be much smaller than average conductance of MTJ. In section 4.4, we will demonstrate a 2-Dimentional transistor satisfying these conditions on same chip as PMA-MTJ. Essentially, in this chapter we have successfully implemented all the building blocks required for p-bits with embedded MTJs.

4.2   Fabrication of PMA-MTJ
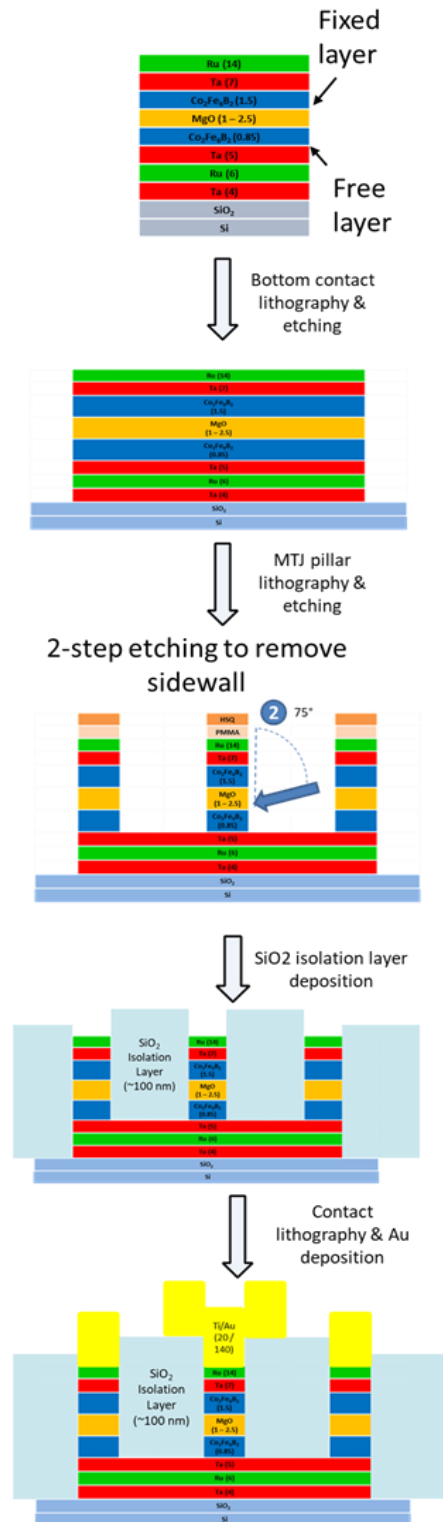
Figure 4.2: Process flow for fabrication of MTJs.

In previous chapter, we have demonstrated in-plane MTJ with small TMR of few percents. Low TMR results in low read-out voltages and hence limiting speed & size of p-bit circuits. Hence, we are developing fabrication recipes for nano-scale PMA-MTJs with high TMR capable of providing large read-out voltages. In this work, MTJ material stack (shown in Figure 4.2) provided by Prof. Weigang Wang from University of Arizona was used to fabricate PMA-MTJs. First PMMA-HSQ bilayer was spin-coated on MTJ stack films. The bottom contacts and the connecting bar are then written using E-beam lithography. With the protective PMMA-HSQ hard-cap in place, the sample is milled down to the lower SiO_2 surface. An O_2 etch is used for the PMMA while the
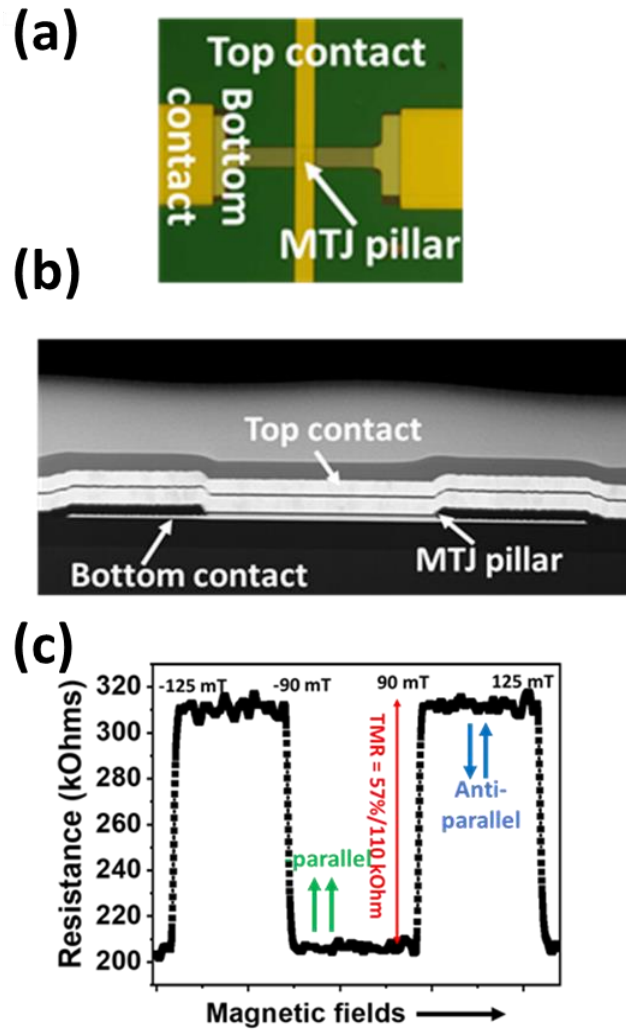
Figure 4.3: (a) & (b) Optical and cross-sectional TEM of PMA-MTJ. (c) Major loop of TMR with respect to out-of-plane magnetic field showing TMR of ~57%.

53

stack itself is milled using AJA ion miller (250V beam voltage, 70 mA beam current, 30° incident angle). The sample is rotated at 18rpm while milling occurs. The milling involves 30 second windows of actual milling and 1 minute intervals where the beam is off. Etched sample is placed in Remover PG at 80°C and then ultra-sonicated in acetone & IPA to remove the PMMA/HSQ hard-capping layer. Next, a PMMA-HSQ bilayer is spin-coated on the sample and patterned so as to protect what will be the bottom contacts and the MTJ, here a circular pillar in the middle of the bar. An O_2 etch is used for the PMMA layer while the stack itself is milled with Argon (with the same beam parameters as before). The MTJ pillar etch is carried out in two stages. Firstly, the stack is milled at 30° until the bottom contact Tantalum is reached. Secondly, a sidewall cleaning
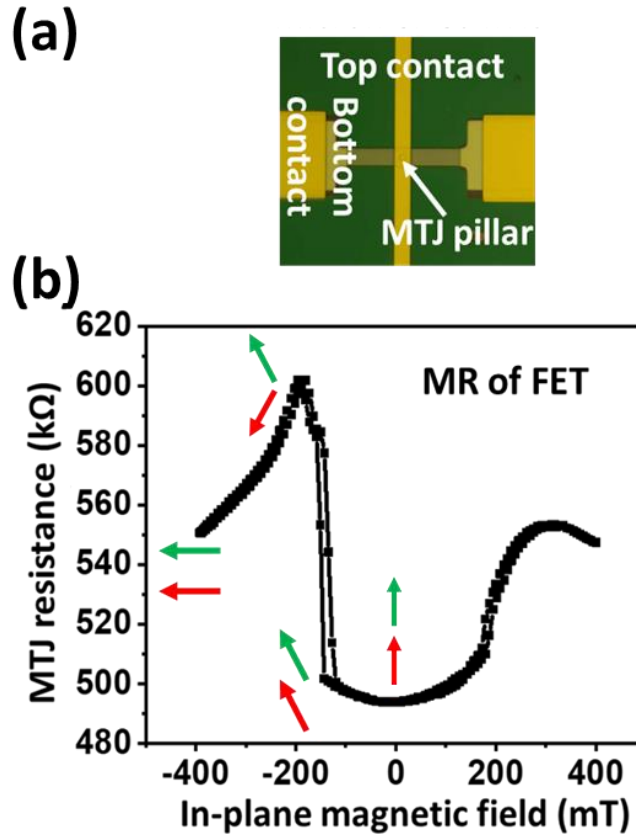
Figure 4.4: (a) Optical image of PMA-MTJ. (b) Magnetoresistance of MTJ in presence of in-plane magnetic fields.

etch is carried out at 75° for 30 seconds (with same beam parameters as previous stage). We have used end-point detection in the AJA tool, to precisely control etching thicknesses and developed 2-step (angled) etching process (as shown in Figure 4.2(c)) to remove side-wall deposited around

MTJ pillar. With the PMMA-HSQ hard capping layer still in place, an insulating layer of SiO2 is sputter deposited. The PMMA/HSQ bilayer (whose layer thicknesses are shown closer to scale in this graphic) is then lifted off by placing the sample in Remover PG at 80°C overnight. The sample is then ultra-sonicated in acetone & IPA to remove the PMMA/HSQ hard-cap. The lift off process leaves trenches in the deposited SiO2 layer, leaving the bottom contact pads and the top of the MTJ pillar exposed. Finally, A PMMA bilayer (consisting of A4-495 and A4-950 PMMA) is then spin-coated onto the sample. Metal contacts to MTJ pillar and bottom bar are defined using E-beam lithography and deposited using e-beam evaporator. Lift-off of the PMMA bilayer is done using the same lift-off process described previously. The last step is to anneal the finished devices for 30 minutes at 300°C. Optical and TEM images of fabricated MTJ are shown in Figure 4.3(a) & (b) while TMR vs out-of-plane magnetic field measurement is shown in Figure 4.3(c). Free layer in MTJ switches at magnetic field of ~90 mT while fixed layer switches at ~125 mT. Total TMR (R_{AP}-R_P/R_P) is approximately 57% while total resistance change (R_{AP}-R_P) is approximately 110 kOhm. Magnetoresistance of another MTJ in presence of in-plane magnetic field is shown in
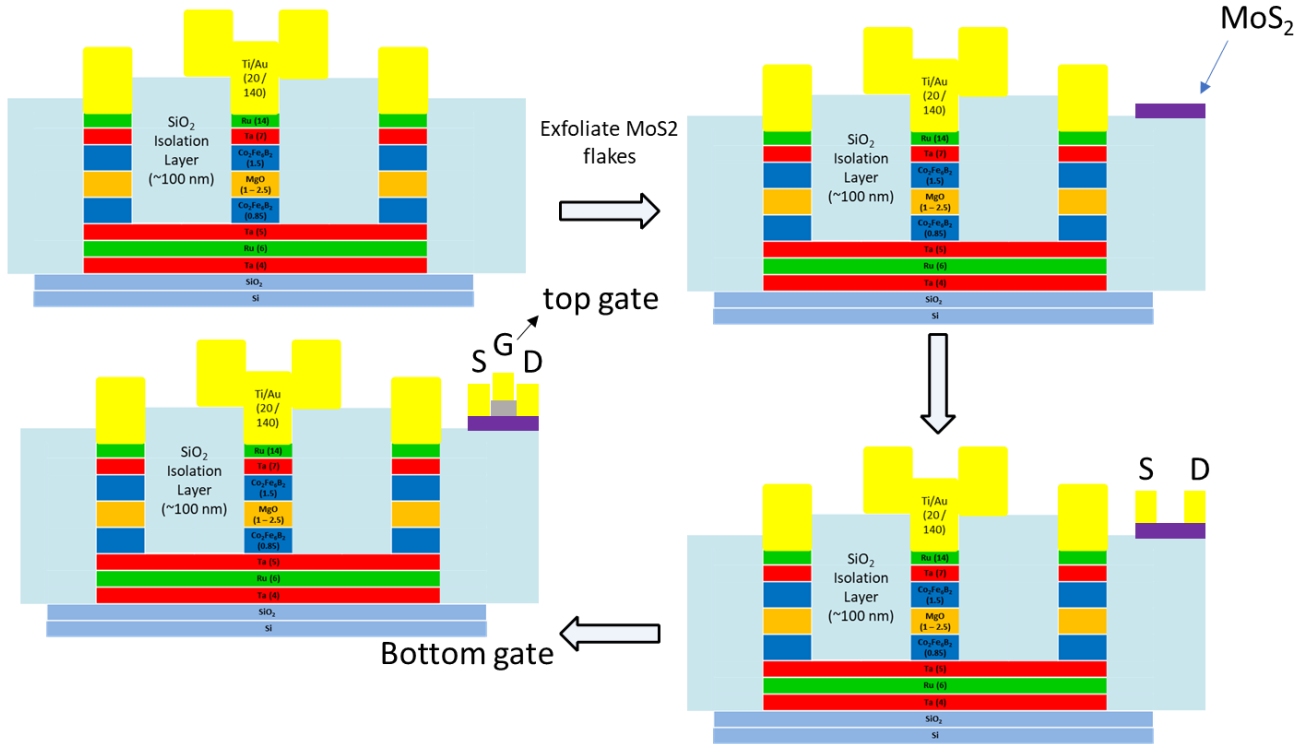
Figure 4.5: Process flow for fabrication of 2D-transistor on same chip as MTJs.

figure 4.4 (b).Having fabrication of MTJs under control, we can now build p-bits by scaling down the MTJ to nano-scale or by changing thickness of free layer in PMA-MTJ stacks.

4.3   MoS$_2$ transistor for in-chip p-bit

Our goal is to demonstrate p-bit with embedded MTJ using a low barrier PMA-MTJ and transistor built with 2D semiconductors such as MoS$_2$. Towards this goal, on the same Si/SiO2 substrate with PMA-MTJ demonstrated in previous section, we exfoliated thin flakes of MoS$_2$ and fabricated back-gated MoS$_2$ transistor with process flow shown in as shown in Figure 4.5. Exemplary transfer characteristic of such MoS$_2$ transistor shown in Figure 4.6(b). Fabricated MoS$_2$ transistor have drain current (I_{ds}) ON-OFF ratio of ~10^6 and ON-state conductance much larger
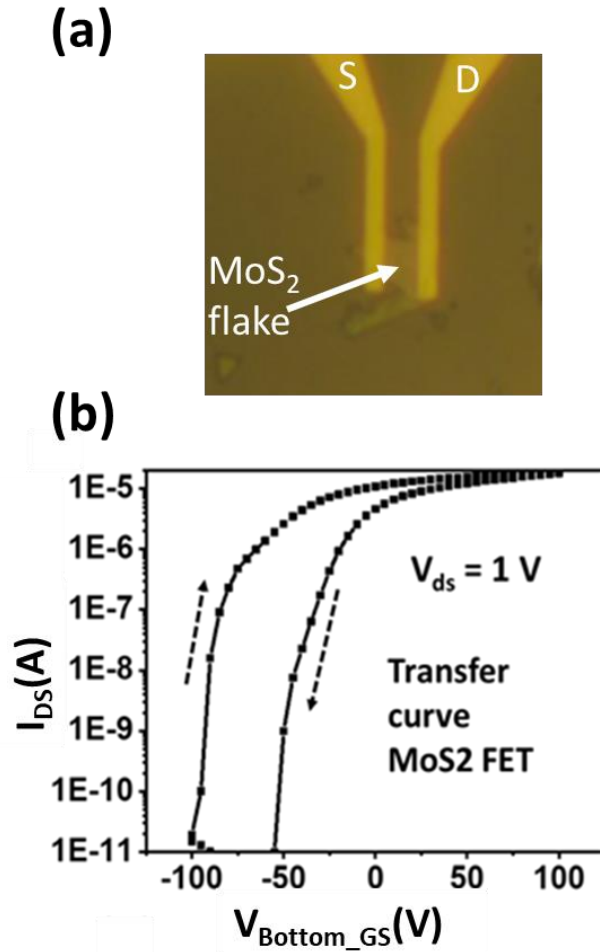
Figure 4.6: (a) Optical image of MoS$_2$ transistor and (b) transfer characteristic of MoS$_2$

56

than MTJ conductance and OFF-state conductance much smaller than the conductance of MTJ device shown in Figure 4.4 (a). Magnetoresistance of the MTJ in presence of in-plane magnetic field is shown in figure 4.4 (b). These conditions are essential for implementation of p-bit in 1T/1MTJ structure. Furthermore, we can electrically connect MTJ with MoS_2 transistor in series as shown in Figure 4.7(a) and characterize MR of 1-MTJ and 1-transistor system for different gate voltages. Figure 4.7(c) & (d) shows MR of the system for two gate voltages. Observed gate dependence of MR shows that MoS_2 (2-D material) is the working principal of p-bits with embedded p-bit. Future work will involve achieving low energy barrier MTJ in this 1T/1MTJ structure. In conclusion, we have successfully fabricated (high barrier) MTJ and MoS_2-transistor on same Si/SiO2 substrate and have shown magnetoresistance of 1-Transistor and 1-MTJ system, paving way to realize on-chip p-bits.
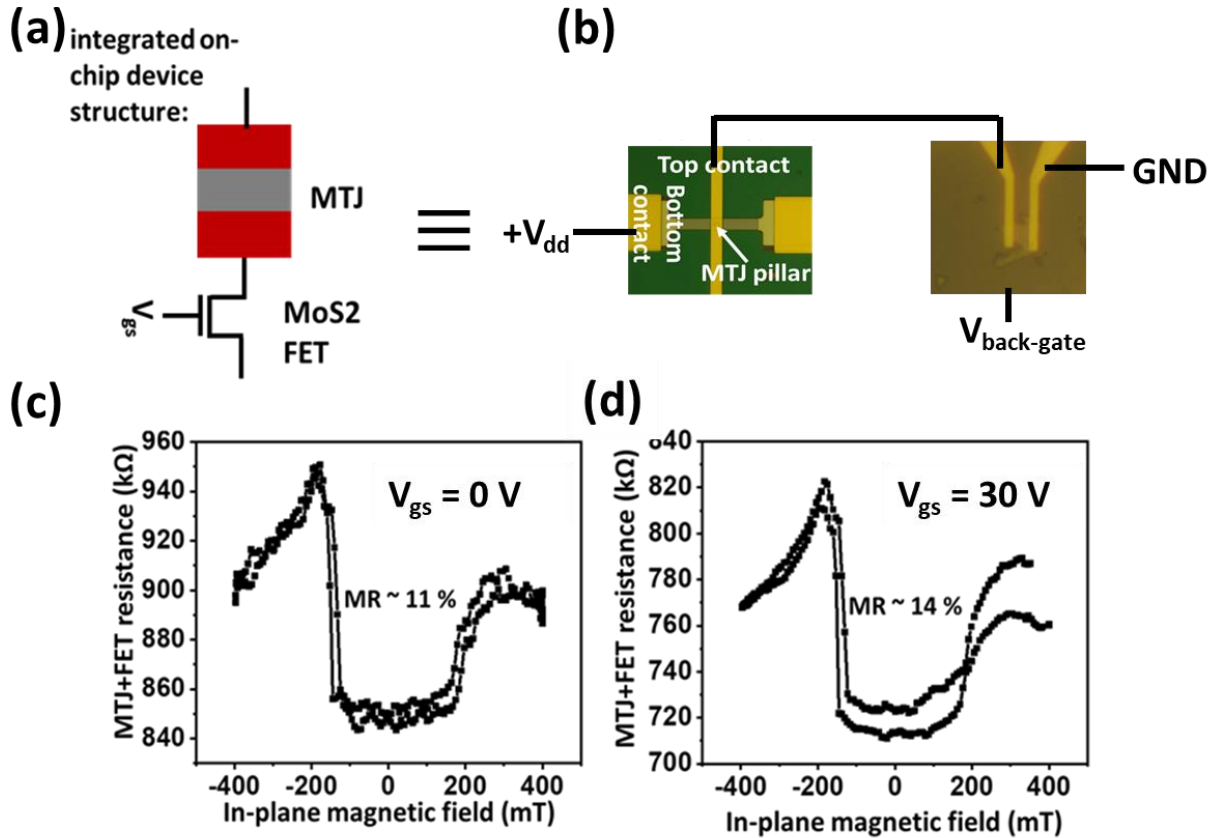
Figure 4.7: (a)&(b) Schematic & optical image of integrated 1T/1MTJ structure. (c)&(d) MR of the 1T/1MTJ structures in presence of in-plane magnetic fields for input gate voltages (V_{gs}) of 0 V and 30 V respectively.

4.4   Annealing to tune magnetic anisotropy of PMA

Having demonstrated on-chip 1T/1MTJ structure, next step towards realization of p-bit is to lower energy barrier of the MTJ in the 1T/1MTJ structure. In general, PMA-MTJs are preferred for STT-MRAM technology over in-plane MTJs due to their stability even for scaled devices down to few tens of nanometers. That is why implementing low barrier PMA-MTJ is challenging task. However, previous studies have shown that the magnetic anisotropy of PMA-MTJ which determines the energy barrier of the MTJ is function of thickness of ferromagnetic layer and annealing recipe. Hence, in this section, we will study how to control the magnetic anisotropy or energy barrier of PMA-MTJ by engineering thickness and annealing recipe of MTJs.
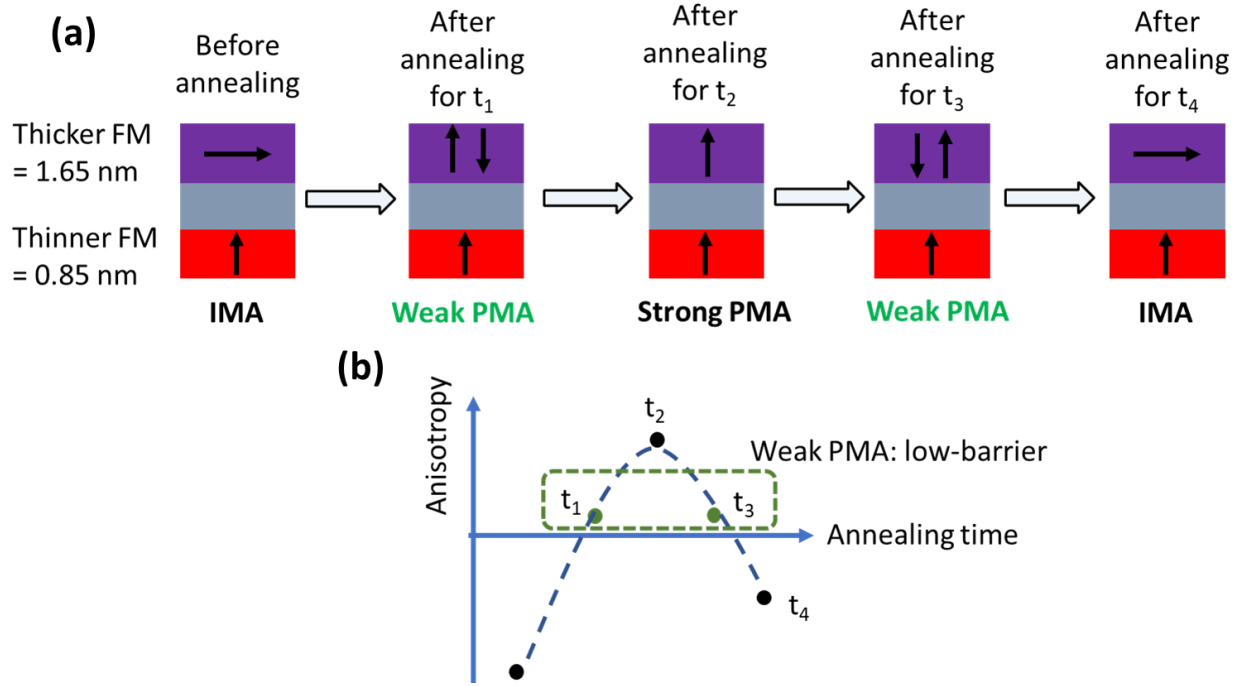
Figure 4.8: (a) Expected changes in the magnetic anisotropy of MTJ consisting of ferromagnets of thicknesses of 0.85 nm and 1.65 nm separated by MgO tunnel barrier with annealing. (b) Expected magnetic anisotropy of MTJ for different annealing times.

MTJ Stack used for this study was provided by Prof Weigang Wang's group and it consists of. Note that thickness of the free layer used in this stack is larger than that of previous stack used in section 4.2. For this thickness, free layer of the MTJ prefers to lie in-plane rather than out-of-plane without any annealing. However, by annealing the MTJs for time t_1, crystallization and defect reduction in the free layer and MgO results in weak perpendicular magnetic anisotropy in
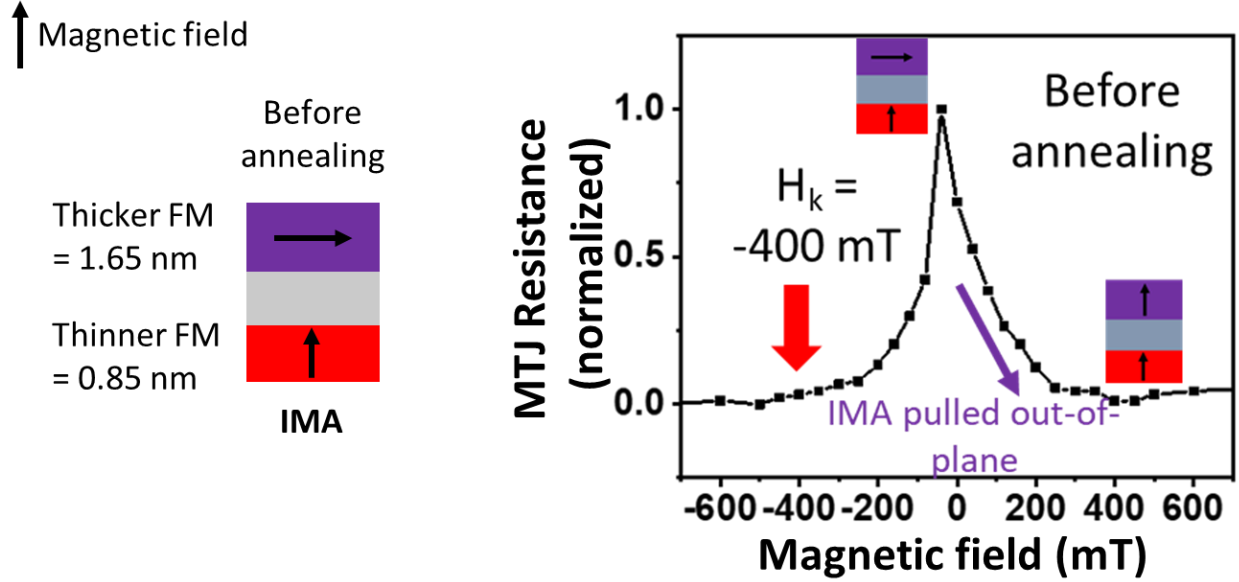
Figure 4.9: Magnetoresistance (MR) of MTJs annealed with respect to out-of-plane magnetic field before annealing. Red arrows show "saturation point" for MR, used for determining magnetic anisotropy of the free layer.

the free later (Figure 4.8(a)). At this juncture, the free layer is very close to transitioning from in-plane to out-of-plane. Further annealing for time t_2 should induce strong perpendicular magnetic anisotropy (H_k). However, any further annealing will result in degradation of H_k as shown in Figure 4.8(b). Hence, for annealing time t_1 and t_3, free layer of the MTJs will have weak H_k and low energy barrier. So, goal of the following experiments is to determine annealing times t_1 and t_3 which should give us low barrier MTJs. We fabricated MTJs of various sizes (from 500 nm to 4 um in diameter) using similar process flow used in the section 4.2. After fabrication of multiple samples with MTJs, rapid thermal annealing (RTA) was performed for 3 and 5 minutes. Next, major and minor loops of TMR with respect to out-of-plane magnetic field was measured for MTJs annealed for different time periods to determine H_k of the free layer. Since, free layer is in-plane before annealing, large out-of-plane magnetic field is required to pull magnetization of the free layer out-of-plane and is represented by the "saturation point" in MR curves in Figure 4.9(a). This out-of-plane magnetic field is the H_k (with a negative sign) of our free layer. Similarly, H_k of free layer was measured for samples annealed for time 3 mins, 5mins. After annealing for 5 mins, only 10 mT are sufficient to pull the magnetization of free layer out-of-plane (figure 4.10). This suggest free layer is very close to transitioning from in-plane to out-of-plane magnet. In figure 4.11, we

have plotted H_k with respect to annealing time. This plot suggests annealing time of 5-7 mins would be ideal to realize PMA-MTJs with weak anisotropy i.e. low energy barrier.
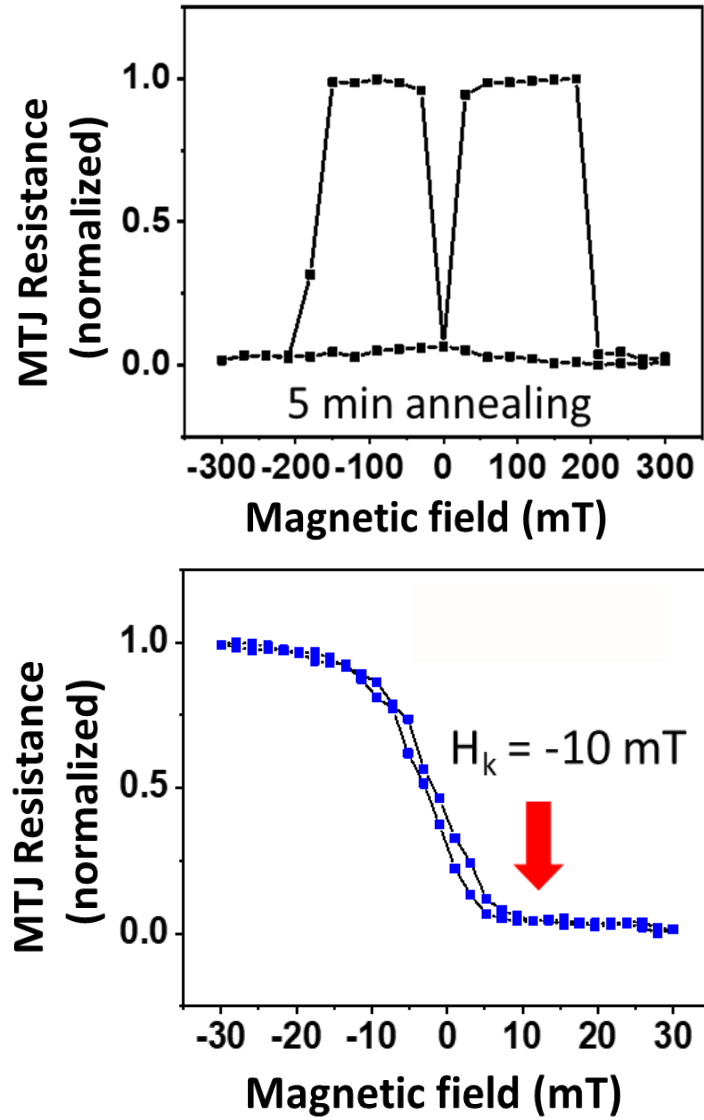
Figure 4.10: Magnetoresistance (MR) of MTJs with respect to out-of-plane magnetic field annealed for 5 mins
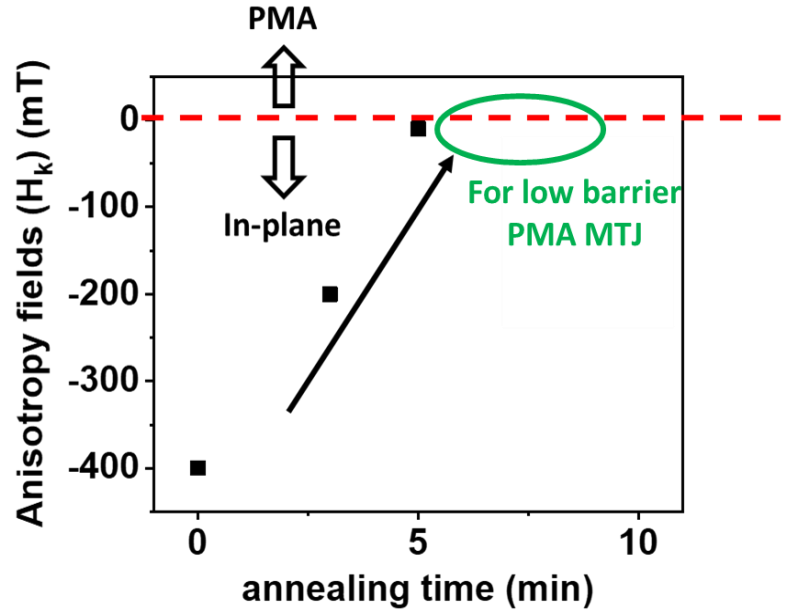
Figure 4.11: Annealing time dependent H_k of the free layer.

In conclusion, we have demonstrated on-chip 1T/1MTJ structure similar to a p-bit with embedded MTJ. Individual devices in the 1T/1MTJ structure satisfy conditions essential for implementation of p-bit such as MTJ with high TMR and 2D-transistor with large ON-OFF current ratio. We have also shown that by using engineered MTJ stack and modifying annealing recipe, one can achieve low barrier PMA-MTJ desired for p-bits.

5. COMPOUND SYNAPSE USING PROBABILISTIC SOT SWITCHING

Applications of PSL requires networks of p-bits connected via weighted interconnects. Hence, programmable non-volatile interconnects, similar to analog resistive cross-bar architectures (synaptic networks) commonly used for neuromorphic computing are required for realization of PSL. In this chapter, we will show analog-type synaptic behavior using stochastic SOT switching of stable/high-barrier nanomagnets paving a way to realize p-bit networks solely with MTJs integrated with CMOS devices. We utilize concept of compound synapses that consist of an ensemble of binary memory elements. Employing the probabilistic switching of individual memory elements, multilevel operation can be realized in a reproducible fashion. In fact, simulations of spiking neural networks (SNN)[82] using compound synapses from binary memory devices can elucidate the desired performance specifications. Moreover, experimental implementations based on an arrangement of parallel binary RRAM devices and simulations of convolutional neural networks (CNNs) [83] demonstrated multi-level operation of such compound synapse structures. Here, we utilize the intrinsic property of spin devices to exhibit thermally activated switching of their magnetization that is probabilistic in nature. We have built and characterized an array of nanomagnets with perpendicular shape anisotropy (PMA) located on a tantalum layer that acts as a spin Hall effect (SHE) channel. Probabilistic switching of the individual nanomagnets is used to realize our SOT synapse. Since an individual nanomagnet has a finite probability of switching for a properly chosen current pulse through the tantalum layer, the ensemble of nanomagnets shows a gradual increase (potentiation) or decrease (depression) in the total magnetization state similar to an analog memory element. While the observed potentiation and depression is non-linear in general due to the stochastic nature of our compound synapse, a modified pulse scheme, as discussed below, can be used to alleviate this issue.

5.1   Experimental Section

A Ta(5nm)/CoFeB(1nm)/MgO(2nm)/Ta(2nm) magnetic stack with perpendicular magnetic anisotropy (PMA) was deposited on a Si/SiO2 substrate using sputter deposition techniques. In the first e-beam lithography step, a Hall bar was patterned by etching through the entire Ta/CoFeB/MgO/Ta stack until the SiO2 substrate was reached using Ar ion milling. Subsequently, either a single nanomagnet or an ensemble of nanomagnets are patterned on the Hall bars and defined by etching through the top part of the material stack until the bottom Ta layer was reached. Finally, Ti/Au metal pads were deposited using a standard lift-off process, enabling contacts to the devices. To detect the magnetization state of the system, Anomalous Hall Effect (AHE) measurements were performed using a lock-in scheme after quasi-static pulses of 20 to 50 us in width were applied to switch the nanomagnets.
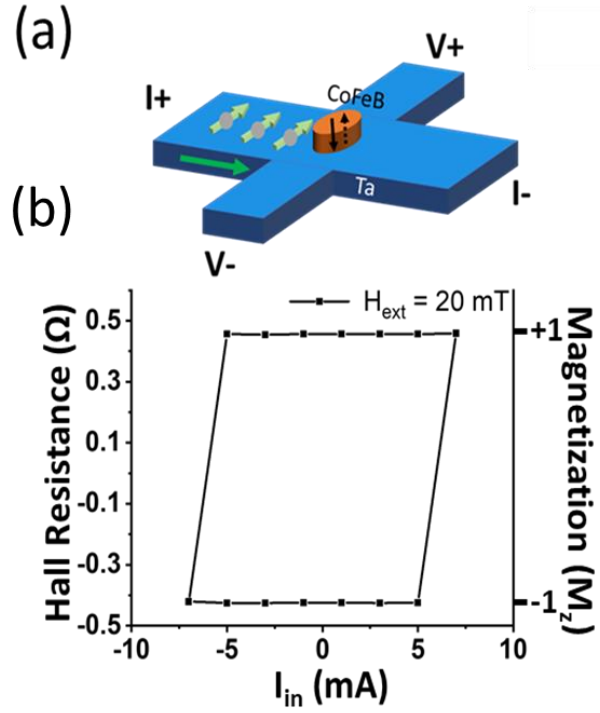
Figure 5.1: (a) Measurement set-up for SOT switching. (b) SOT switching of a single nanomagnet (binary memory unit).

5.2 Emulating synaptic behavior using probabilistic switching single nanomagnet

Figure 5.1(a) & (b) shows SOT switching of a fabricated Hall bar with a single nanomagnet using current pulses of 50 us width in the presence of an in-plane external field of 20 mT in the current direction. The Hall bar had a width of around 4 um and the nanomagnet on top is elliptical in shape with axes dimensions of 1 and 3 um respectively and the shorter axis in the current direction. Typically, an external magnetic field is required for SOT driven switching of PMA magnets to break the symmetry of the system [15]. To explore the probabilistic nature of SOT switching (as shown in figure 5.2(a)), we first apply a high negative current (RESET) pulse [width:
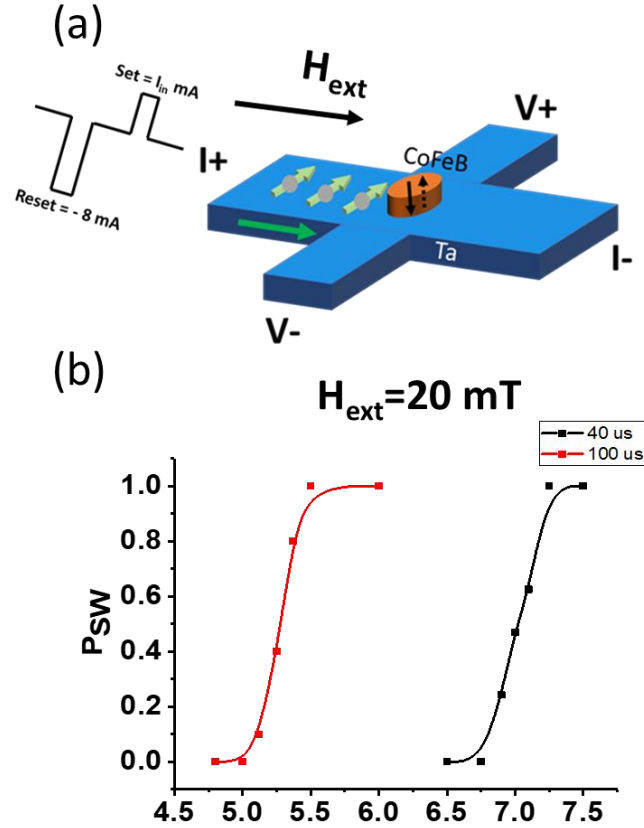
Figure 5.2: (a) Modified pulsed scheme to characterize probabilistic nature of SOT switching. (b) Switching probability (P_{sw}) curve for two different current pulse widths.

50 us] to deterministically switch the nanomagnet to its 0 state, followed by a positive current pulse with varying amplitude (SET) to probabilistically switch the nanomagnet to its +1 state.

Figure 5.2(b) depicts the average probability of switching. As expected, a higher SET current amplitude results in a higher probability of switching. In addition, measurements were also
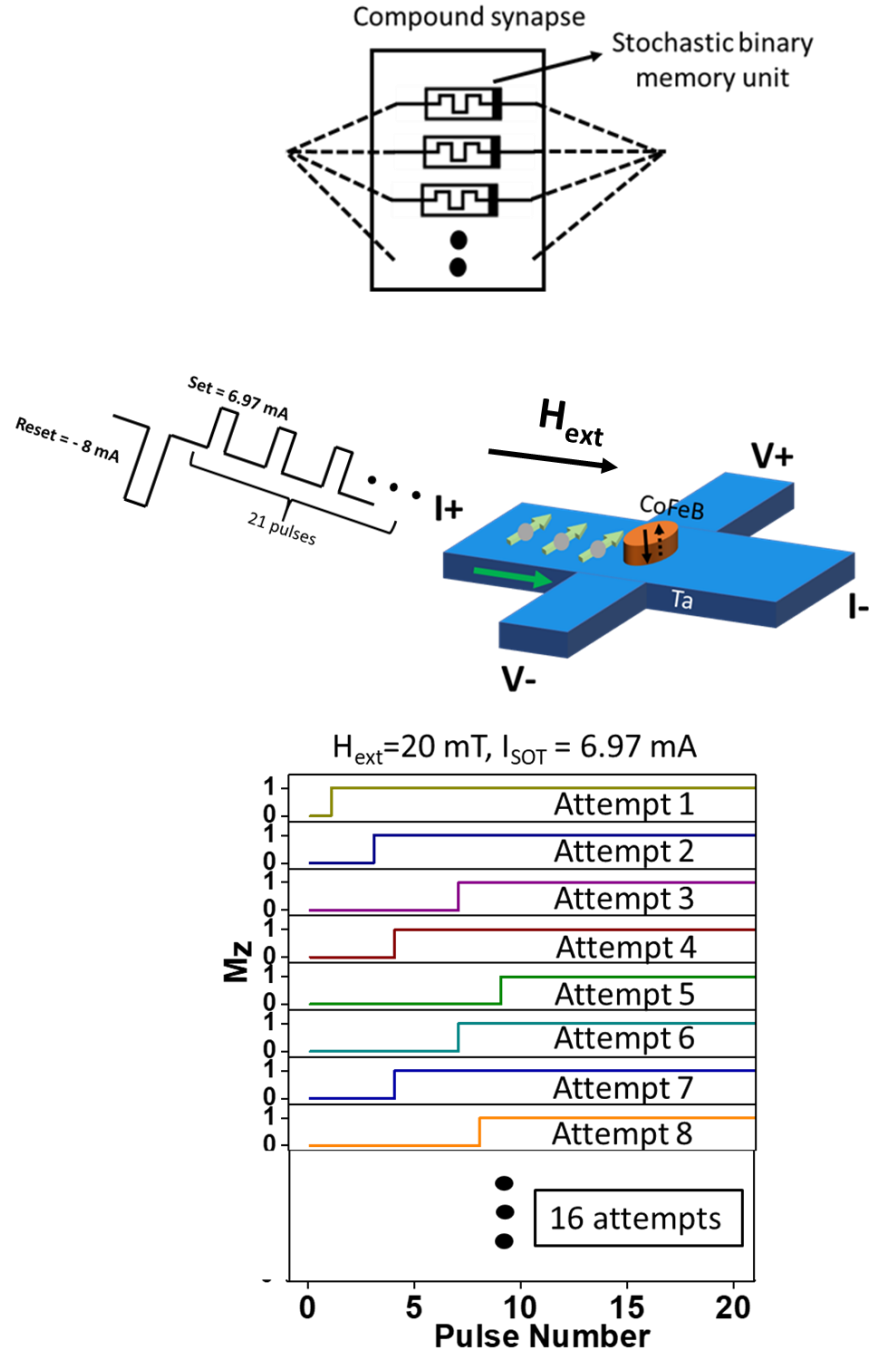
Figure 5.3: (a) Measurement scheme to emulate compound synapse using SOT device with single nanomagnet. (b) Compound synapse consisting multiple stochastic binary unit. (c) Experimental data on magnetization state with pulse number for measurement scheme shown in (a).

performed employing a pulse width of 20 us, which resulted in a similar trend but higher current requirements for the probabilistic switching, consistent with the expectations for thermally activated spin torque switching. Note that thermally activated switching of nanomagnets is inherently probabilistic in nature and occurs at nanosecond time scales, which implies that in principle even pulses with widths of nanoseconds are expected to allow for the above described observation.

An n-bit compound synapse can be realized using 2n such nanomagnets operating in the probabilistic switching regime and working in parallel or series (Figure 5.3(a)). To emulate a 4-bit synapse with the "one nanomagnet device", the device was first set to its -1 state as described before. Next, 20 SET pulses at a current level of 6.97 mA with a pulse width of 20 us were applied to the sample as shown in Figure 5.3(b). Note that this current level lies in the probabilistic switching regime of the nanomagnet shown in Figure 5.2(b). Due to the probabilistic nature of switching, the nanomagnet can switch to its +1 state during any of the 20 SET pulses and will remain in this +1 state for all subsequent SET pulses (Figure 5.3(c)), since the energetic barrier between the -1 and +1 state is of the order of $40k_BT$. Since a 4-bit compound synapse is an ensemble of such 16 devices, our experiment is repeated 16 times on the same device. In this way, instead of using an ensemble of 16 devices, we are able to use a single device to emulate the switching behavior of the ensemble. Figure 5.4 shows the outcome of this experiment. The number
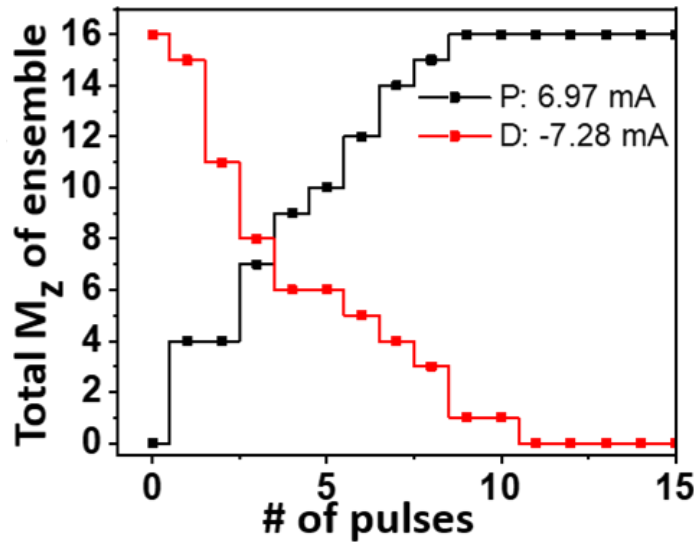
Figure 5.4: Experimental potentiation and depression curves derived using results shown in 5.3(c).

of nanomagnets switched is plotted versus the SET pulse number. The black line clearly illustrates the increasing probability of finding the one nanomagnet switched in all 16 repeated experiments in its +1 state. Such behavior is analogous to the potentiation (P) curve of an analog synapse where the conductance increases gradually with the number of input pulses. Similarly, depression (D) operation can be emulated with our "one nanomagnet device" when input current pulses of -7.28 mA are used – see red curve in Figure 5.4. Note that by using an MTJ structure instead of our nanomagnet, the plot in Figure 5.4 would result in an incremental change in conductance through the MTJ with the number of pulses instead of a change in anomalous Hall resistance, making the approach much more technology relevant and feasible.

5.3   Mathematical modeling of compound synapse

The P and D behavior of compound synapse can be captured using a simple mathematical model consisting of 16 independent binary variables, each having a finite probability of switching for a single pulse (p). During one cycle of potentiation and depression, each one of the 16 variables can probabilistically switch for each of the input pulse and the number of variables switched are plotted with respect to the number of input pulses. Grey lines in Figure 5.5(b) corresponds to individual P and D cycles while the red line in Figure 5.5(b) is average of 100 such cycles. P and D curves of compound synapse is nonlinear with respect to the pulse number but shows saturating behavior. Such non-linear behavior is observed even for analog type RRAM memristors due to characteristics of filaments formation. For neural networks, non-linear behavior has a detrimental effect on the accuracy of network and to improve the linearity, modified pulse-schemes are being explored. In such approach, instead of using identical pulses, pulses with either incremental pulse-width or pulse-amplitude (as shown in Figure 5.5(c)) are used. This approach has extra circuit-area, time and power cost associated with it compared to identical pulse scheme. We are exploring such a scheme for the compound synapse approach assuming probability of switching has sigmoidal dependency on the pulse-amplitude. Figure 5.5(d) shows mathematically expected potentiation and depression for incremental amplitude pulse scheme, which shows improved linearity.
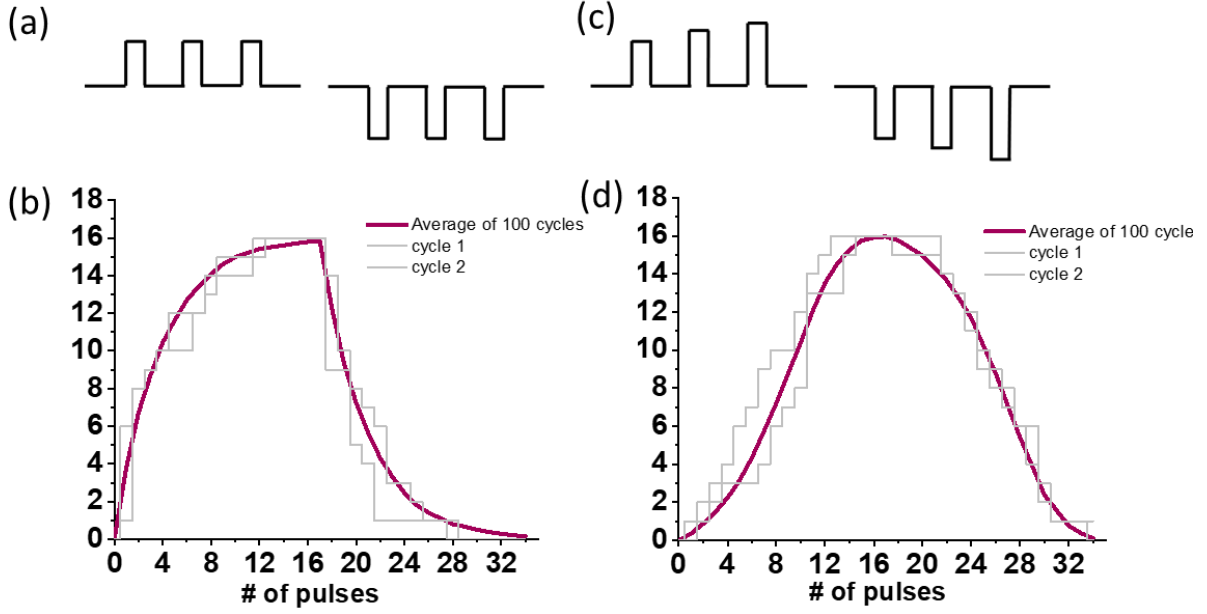
Figure 5.5: (a) Pulse scheme I: identical pulses. (b) Expected P and D curve for 100 cycles showing non-linearity. (c) Pulse scheme II: incremental pulses. (d) Expected P and D curve for 100 cycles with incremental pulse scheme showing better symmetry and linearity.

5.4 Demonstration of 4-bit compound synapse

Next, we have studied an actual 4-bit compound synapse. A cross shaped Hall bar structure from tantalum with 16 nanomagnets in the cross region was built (see SEM image of the device in Figure 5.6(a)). Figure 5.6(b) shows the anomalous Hall resistance versus perpendicular external magnetic field of the 16 nanomagnet device with resistance steps that correspond to the switching of individual nanomagnets. Each nanomagnet's switching causes a resistance change of around 110 mOhm ≈ 1.8 Ohm / 16. Due to variations in the coercive fields of the 16 nanomagnets as well as the stochastic nature of the nanomagnets' switching steps occur at slightly different magnetic fields. As in the previous experimental approach, the 16 nanomagnet device is initially put in its -1 state, before being subjected to 20 us pulses of identical amplitude (pulse scheme I). Figure 5.7 shows the resulting P curves for three different current levels in addition to one D curve, displaying very similar characteristics as Figure 5.4. As in the "one nanomagnet device" P and D curves of our compound synapse are nonlinear with respect to the pulse number and show a saturating behavior. Note that such non-linear behavior is also observed for analog type RRAM memristors due to the
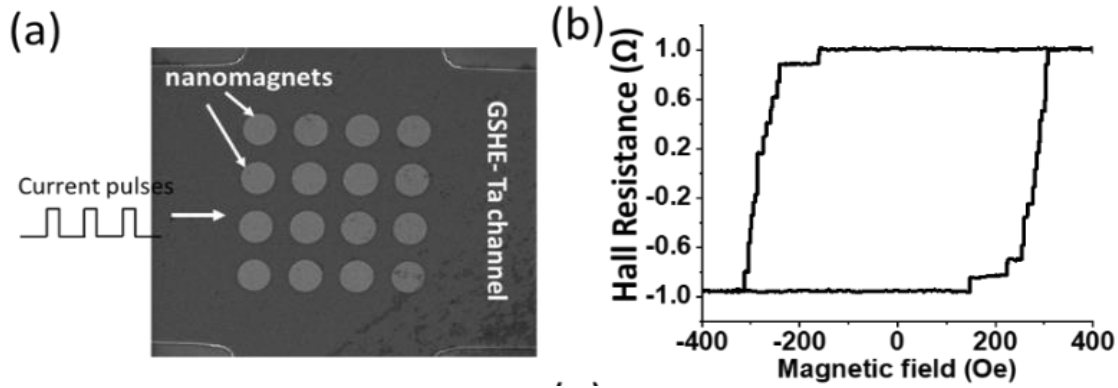
Figure 5.6: Scanning electron microscope (SEM) image of our SOT based synapse with 16 nanomagnets. (b) Anomalous Hall effect vs. out-of-plane magnetic field for the device showing 110 mOhm steps, corresponding to individual nanomagnet switching.

nature of filament formation and breaking during the SET and RESET process. For neural networks, a non-linear response of this type is in general undesirable, since it can have a detrimental impact on the accuracy of the network. To address this issue, researchers [18] have explored a modified pulse scheme in which, instead of using identical pulses, pulses with either
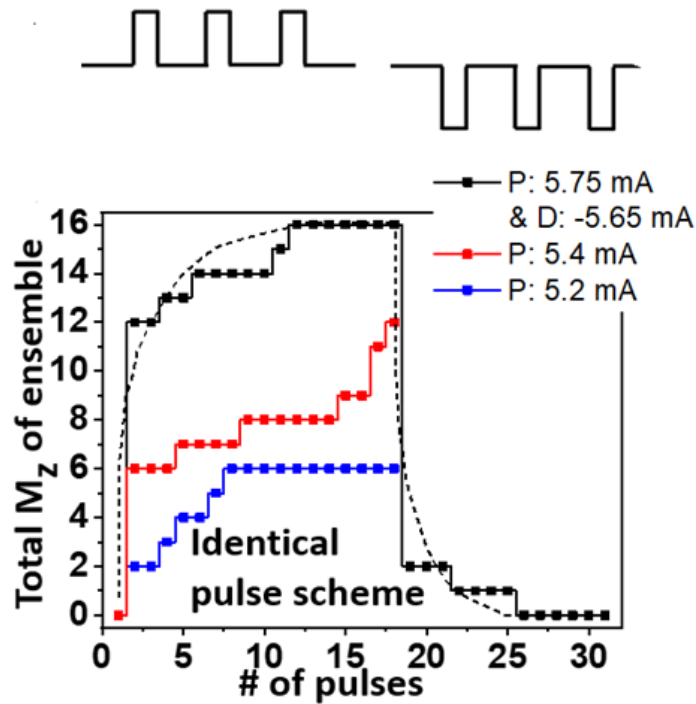
Figure 5.7: Potentiation and depression curve of the device using identical pulse scheme (pulse scheme I)

incrementally increasing pulse-width or pulse-amplitude are used. Figure 5.8 shows the result of adopting this modified pulse scheme for our 4-bit compound synapse. A significantly improved linear characteristic is experimentally obtained when increasing the current amplitude from 5 mA to 6 mA (P-curve) and decreasing it from -4.8 mA to -5.8 mA (D-curve) in steps of 0.05 mA (pulse scheme II). Note that for two sweeps (red and black curve in Figure 5.8) the magnetization change is not identical as individual nanomagnets' switching is stochastic in nature. However, the net magnetization of the magnet ensemble shows an overall improved linearity in the characteristics.
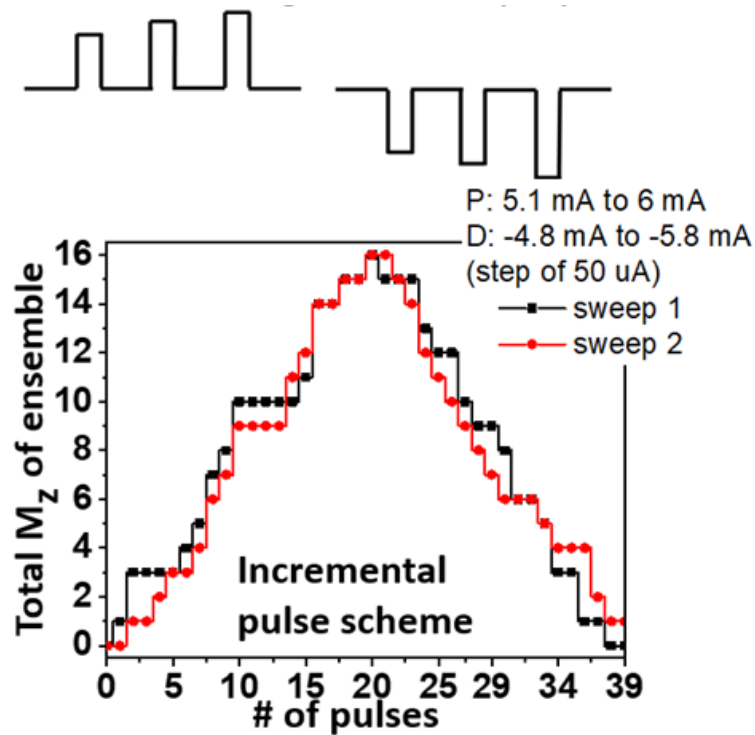
Figure 5.8: Potentiation and depression curve of the device using incremental pulse scheme (pulse scheme II).

5.5   Neural Network with p-bits and compound synapse
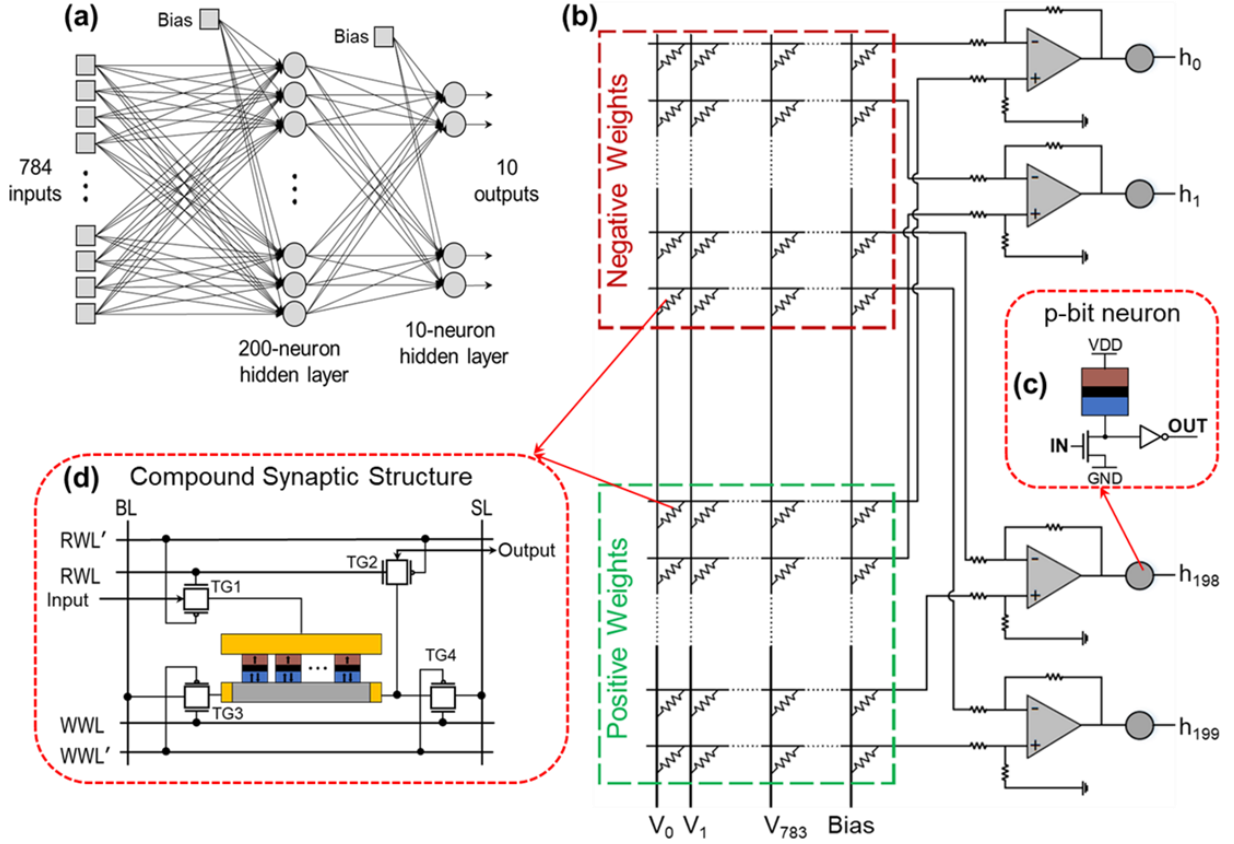
Figure 5.9: (a) Graph representation of the 784×200×10 DBN. (b) Equivalent circuit for the first layer with p-bits as neurons and (d) Compound synapse implemented with MRAM cells.

Demonstrated SOT-MRAM based compound synaptic structure can be used as part of a neural network (Deep Belief Network) that utilizes yet another MTJ based element, i.e. a p-bit (shown in Figure 5.9) [58] as a binary stochastic neuron. Prof. DeMara's group has explored the accuracy of such 784×200×10 DBN as shown in Figure 5.9 for MNIST pattern recognition, noting that the realization of a synaptic network with MRAM elements presents an attractive opportunity to build an all-MRAM based DBN. Figure 5.10 shows error rates of such network for various device parameters such as TMR, RA-product. It is worth noting that although our application-level simulation results have not considered the stochasticity in the compound synaptic structures, which would result in cycle-to-cycle variations of the P and D curves as shown in Figure 5.8, they help gaining insights into the dependence of network accuracy on device parameters such as TMR and
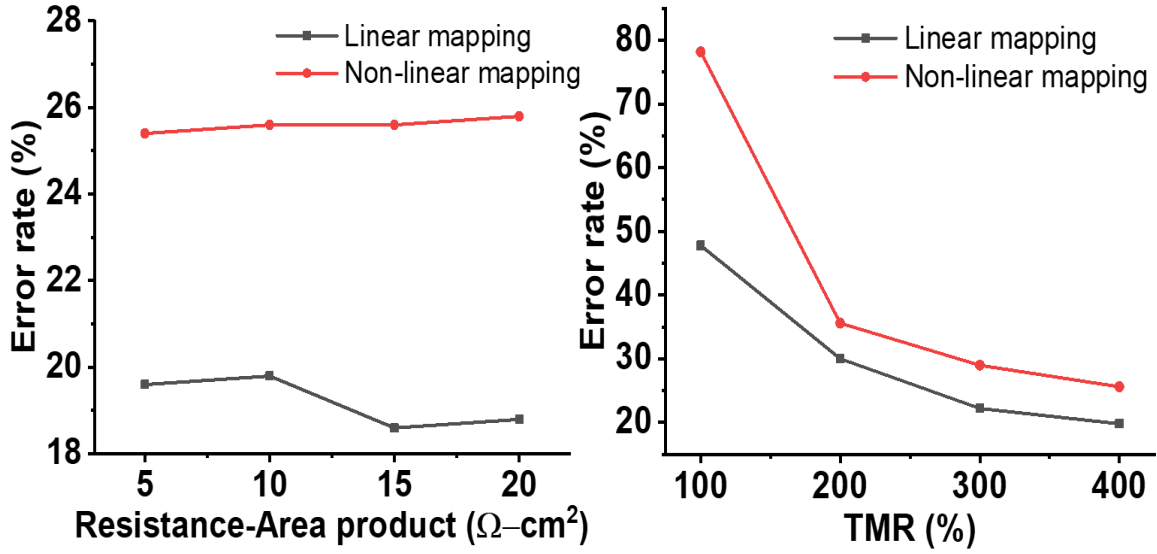
Figure 5.10: (a) Error rate versus resistance-area-product. (b) Error rate versus tunneling magneto resistance (TMR) for a 784×200×10 DBN with 4-bit compound synapses.

RA products as well as understanding the relation between error rates and bit-precision. For instance, a bit-precision of more than 4-bits is not required within the trained network, since the error rates will saturate for higher bit-precision values. Such findings are particularly important to guide future experiments, since the fabrication complexity of compound synaptic structures can significantly increase with larger bit-precision and TMR values. Finally, by comparing the non-linear and linear mapping realized by the identical (scheme I) and incremental (scheme II) pulse schemes, a significant decrease in the error rates for the linear mapping method compared to the non-linear mapping can be observed from Figure 5.10. This highlights the effectiveness of the incremental pulse scheme approach investigated herein. It is worth noting that while cycle-to cycle (C2C) variations induced by the natural stochasticity of our synapses may change the absolute error rate values reported here, the relative accuracy plotted in Figure 5.10 is important to understand the impact of the switching pulse schemes on the performance of the entire network. The obtained results highlight various opportunities for future work, such as: 1) investigating deeper neuromorphic architectures for large-scale applications, 2) leveraging the intrinsic stochasticity of the compound synapses to realize an energy-efficient training approach for quantized neural networks, or 3) applying multi-objective optimizations to tune the network

parameters by including device models in the simulation loop. It is also worthwhile noticing that the compound synaptic structure proposed here can readily be combined with other neuromorphic computing architectures as discussed in [84][85][86][28].

To verify the energy improvements of our compound synaptic structure over a CMOS-based weighted connection, we have utilized the energy consumption values reported in [23] and [24] to estimate the energy consumption for weighted sum operations in a 784×200×10 DBN using integer and floating-point (FP) multiplication and add (MAC) operations. As listed in Table I, the 4-bit compound synapse based DBN circuit can realize approximately two orders-of-magnitude energy improvements over their CMOS-based counterparts. It shall be considered that increasing the bit-precision in a compound synapse from 4-bit to 16-bit or 32-bit can result in higher energy consumptions. However, the increased energy values will be negligible compared to the significant energy reductions that are achieved compared to the integer and FP DBNs. On the other hand, it is shown in [24] that memory accesses normally consume more energy than arithmetic operations, while our proposed compound synapses also operate as memory cells, thus enabling in-memory computations which decreases the memory access energy consumptions to near-zero values, as listed in Table 5.1.

Table 5.1: Energy consumption comparison for weighted-sum operation in a 784×200×10 DBN.

Weighted Connections	Energy Consumption		
	MAC Operations	Memory Access per Instruction	
		Cache	DRAM
8-bit Integer [24]	0.036 μJ	100 pJ	1.3-2.6nJ
32-bit Integer [24]	0.51 μJ	100 pJ	1.3-2.6nJ
16-bit FP [24]	0.24 μJ	100 pJ	1.3-2.6nJ
32-bit FP [24]	0.73 μJ	100 pJ	1.3-2.6nJ
4-bit Compound Synaptic Structure	0.21 nJ	Near-Zero	

Finally, it shall be noted that here we have only focused on the energy consumption which can be realized by our compound synapses, while authors have shown in [19] that the p-bit based neuron can also contribute to several orders of magnitudes energy reduction with respect to previous energy-efficient CMOS-based activation functions for DBN structures.

In conclusion, we have experimentally demonstrated proof-of-concept 4-bit compound synapses using probabilistic spin-orbit torque switching. A modified incremental pulse scheme is shown to result in improved linearity of the synaptic behavior. Furthermore, circuit-level simulations of DBNs consisting of stochastic spin-torque devices, namely p-bits and compound synapses show that the linearity in the synaptic behavior and high TMR-values are crucial device parameters to achieve low error rates.

6. EFFICIENT SOT SWITCHING OF SEMICONDUCTING 2D FERROMAGNET

Most of the material in this chapter has been reprinted with permission from [87]: Ostwal, V., Shen, T., & Appenzeller, J. (2020). Efficient Spin-Orbit Torque Switching of the Semiconducting Van Der Waals Ferromagnet Cr2Ge2Te6. Advanced Materials, 32(7), 1906021. © 2020 WILEY-VCH Verlag GmbH & Co. KGaA, Weinheim

In this chapter, we show for the first time SOT manipulation of semiconducting 2D-FM $Cr_2Ge_2Te_6$ (CGT). Since discovery of ferromagnetism in 2D materials such as CGT in 2018, electrical characterization of their magnetization has proven to be difficult due to their semiconducting nature and low Curie temperature. Most of the studies on CGT have utilized MOKE[33][88] or MFM[89] to study its magnetic properties. A stack consisting of HMs such as Pt or W deposited on an insulating FM such as TMIG has shown to result in an induced anomalous Hall effect in the metal, thus providing an electrical path towards reading the magnetization of insulating FMs[90][91]. In fact, a recent study has used a similar approach to characterize a CGT/Pt heterostructure[92]. In this article, we utilize the induced AHE in Ta to study the magnetization properties of CGT for various thicknesses. For thinner CGT films, we show by means of AHE that the out-of-plane magnetization (m_z) can be switched with a combination of SOT and in-plane magnetic fields similar to field-assisted magnetization switching in conventional metallic HM/FM films such as Ta/CoFeB/MgO. Our key finding is that SOT currents required for manipulation of the magnetization in a CGT/Ta system are almost two orders of magnitude smaller than in conventional metallic HM/FM systems.
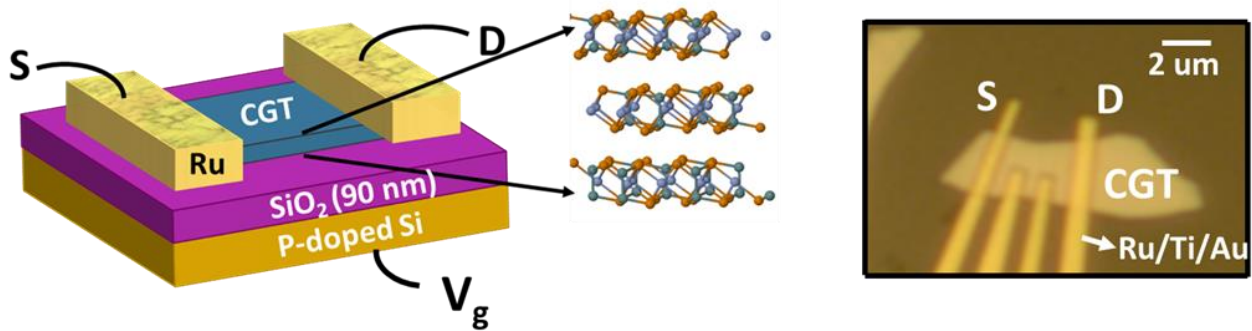
Figure 6.1: (a) 3D schematic of our back-gated FET with semiconducting CGT channel and Ru contacts. (b) Optical image of the actual device under investigation. © 2020 WILEY-VCH Verlag GmbH & Co. KGaA, Weinheim.

6.1 Electrical characterization of CGT

To study the electrical properties of CGT, back-gated field-effect transistor (FET) structures with a 90nm SiO_2 gate-oxide were fabricated using standard scotch-tape exfoliation techniques on commercially purchased crystals. Immediately before sputtering the electron beam lithography defined source and drain Ruthenium (Ru) contacts, the CGT surface in the contact regions was mildly etched using an Ar plasma to remove the top CGT natural oxide layer to improve the contact quality. A schematic representation of the device layout and an optical image of the device structure are shown in Figure 6.1(a) and (b). Large work function Ru contacts are chosen, since
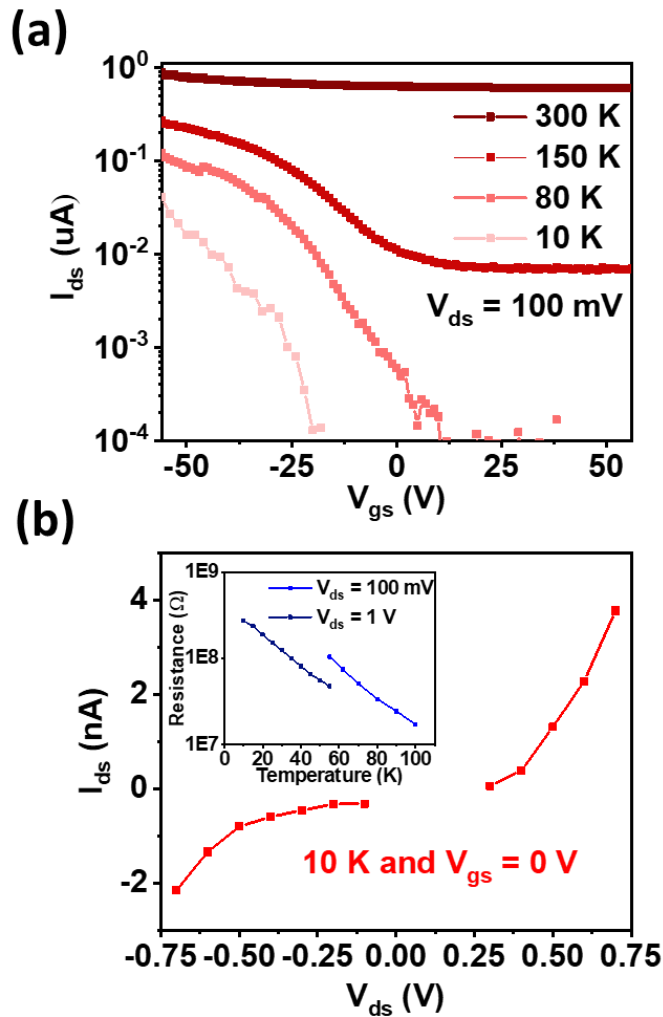
Figure 6.2: (c) Transfer characteristics of the device for temperatures of 10 K, 80 K, 150 K and 300K for V_{ds}=100 mV. (d) Non-linear I_{ds}-V_{ds} characteristics at 10 K for V_{gs}=0 V. (Inset: Temperature dependence of 2-terminal resistance of the device at V_{gs}=0 V. © 2020 WILEY-VCH Verlag GmbH & Co. KGaA, Weinheim.

transport in CGT is dominated by hole conduction through the p-branch [93][88]. Figure 6.2(a), shows transfer characteristics of the device for $V_{ds} = 100$ mV for temperatures ranging from 10K to 300 K. A low on/off drain current (I_{ds}) ratio is observed in transfer characteristics at room temperature. However, at lower temperatures this ratio improves significantly. At 10 K, an on/off current ratio of $\sim 5*10^3$ is obtained for $V_{ds} = 0.7$. Note that such poor transfer characteristics at room temperature are consistent with previous reports of similar CGT FETs[5][11]. We suspect that the poor gate control at high temperatures is a result of oxidation of the top surface, which may result in the formation of a shunting channel. Figure 6.2(b) displays non-linear I_{ds}-V_{ds} characteristics that are expected in Schottky barrier dominated transistors. Moreover, the inset of Figure 6.2(b) shows the temperature dependent 2-terminal resistance of a CGT-FET at $V_{gs} = 0$ V for $V_{ds} = 100$ mV and
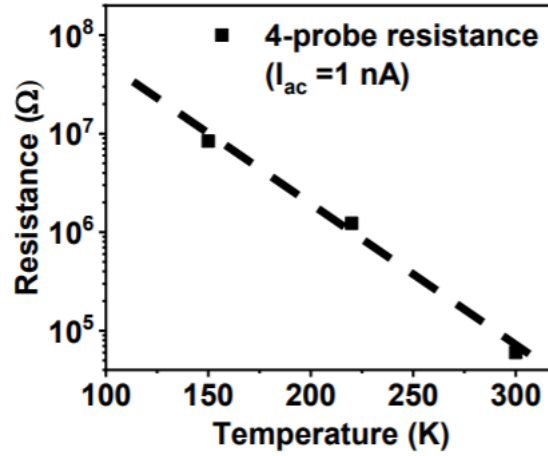
Figure 6.3: Temperature dependence of CGT 4-probe resistance measured using a Keithely 6221 as AC current source and an SR830 lock-in set-up: Since the input impedance of the SR830 is 10 MOhm, 4-probe measurements were not performed at lower temperature. © 2020 WILEY-VCH Verlag GmbH & Co. KGaA, Weinheim.

1V. The observed exponential dependence of resistance on temperature is consistent with the semiconducting nature of CGT. Note that 4-probe resistance measurements as a function of temperature (Figure 6.3) show a similar exponential trend as the 2-terminal resistance in our FET structure, indicating that the temperature dependent behavior of the Schottky barriers is indeed not dominating the observed trends in case of the inset of Figure 6.2(b).

6.2   Anomalous Hall Effect in CGT/Ta heterostructure

Next, we have performed temperature dependent Hall resistance measurements on the CGT/Ta heterostructure to study the magnetic properties of CGT. First, CGT flakes of various thicknesses are exfoliated onto a Si/SiO$_2$ substrate with 90 nm SiO$_2$. To avoid oxidation of the CGT flakes during the fabrication process, air exposure was limited to a few minutes after exfoliation and before the sample was mounted into the vacuum chamber for Ta deposition using a method similar to the one reported in [92]. In addition, a mild Ar plasma clean was performed to remove any oxide layer before depositing 5 nm of Ta using a magnetron sputtering tool (details
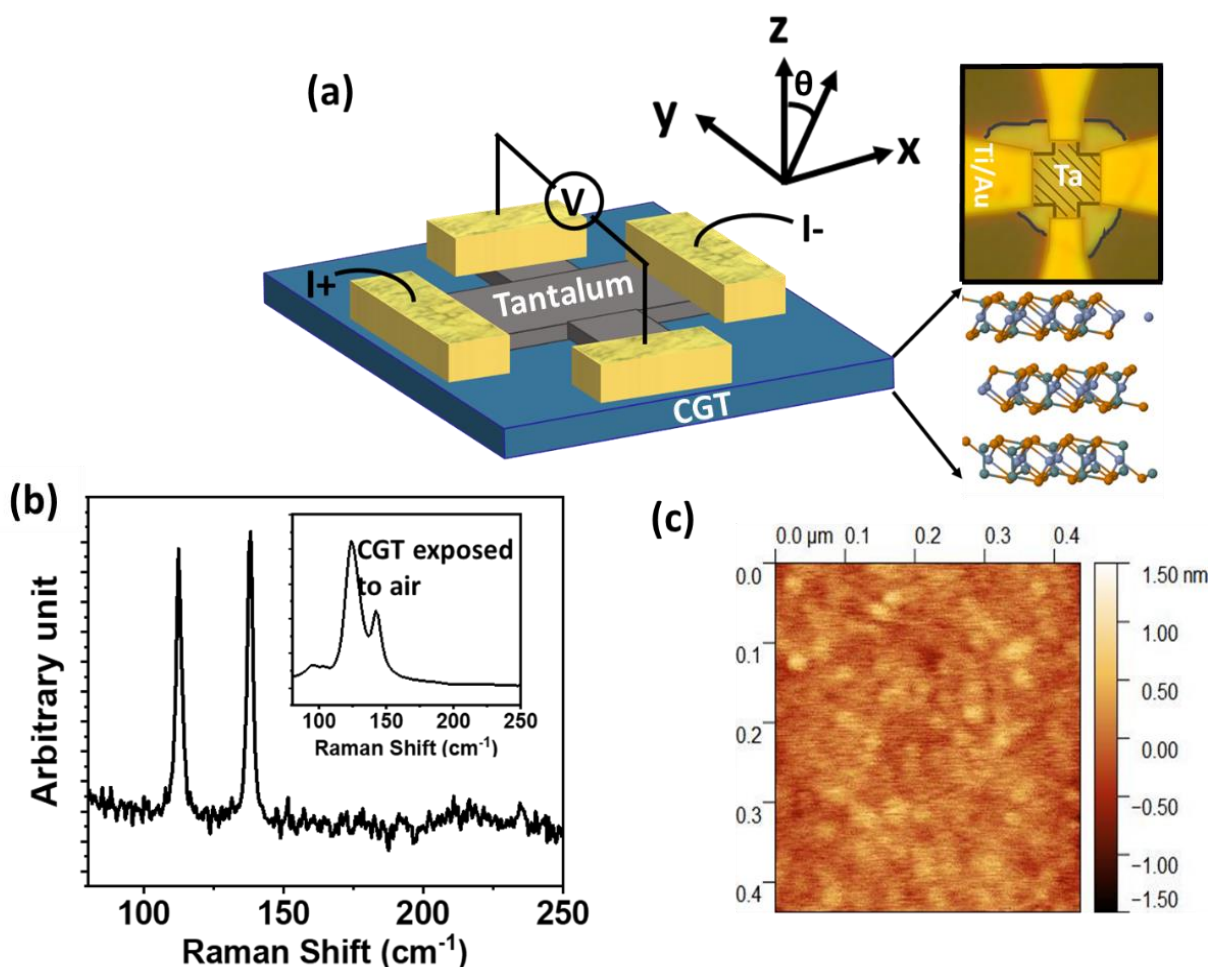
Figure 6.4: (a) 3D schematic and optical image of a fabricated Hall bar device from a CGT/Ta heterostructure and measurement set-up. (b) Raman spectrum of the CGT/Ta heterostructure device. (Inset: Raman spectrum of a CGT flake that was exposed to air). (c) Atomic force microscopy image of the device surface showing sub-nanometer roughness. © 2020 WILEY-VCH Verlag GmbH & Co. KGaA, Weinheim.

are described in the experimental section). The actual Ta-Hall bar structures on the CGT were fabricated using e-beam lithography on a negative resist and Ar ion milling. Since the CGT thickness varies from flake to flake, etching was stopped just after etching the Ta layer, rather than etching the entire CGT areas, which are located outside the Ta-Hall bar masks. Since CGT is highly insulating at low temperatures for $V_{gs} = 0V$ if compared to Ta, current will pass exclusively through the patterned Ta-Hall bar. Finally, Ti/Au contacts were defined using a standard e-beam
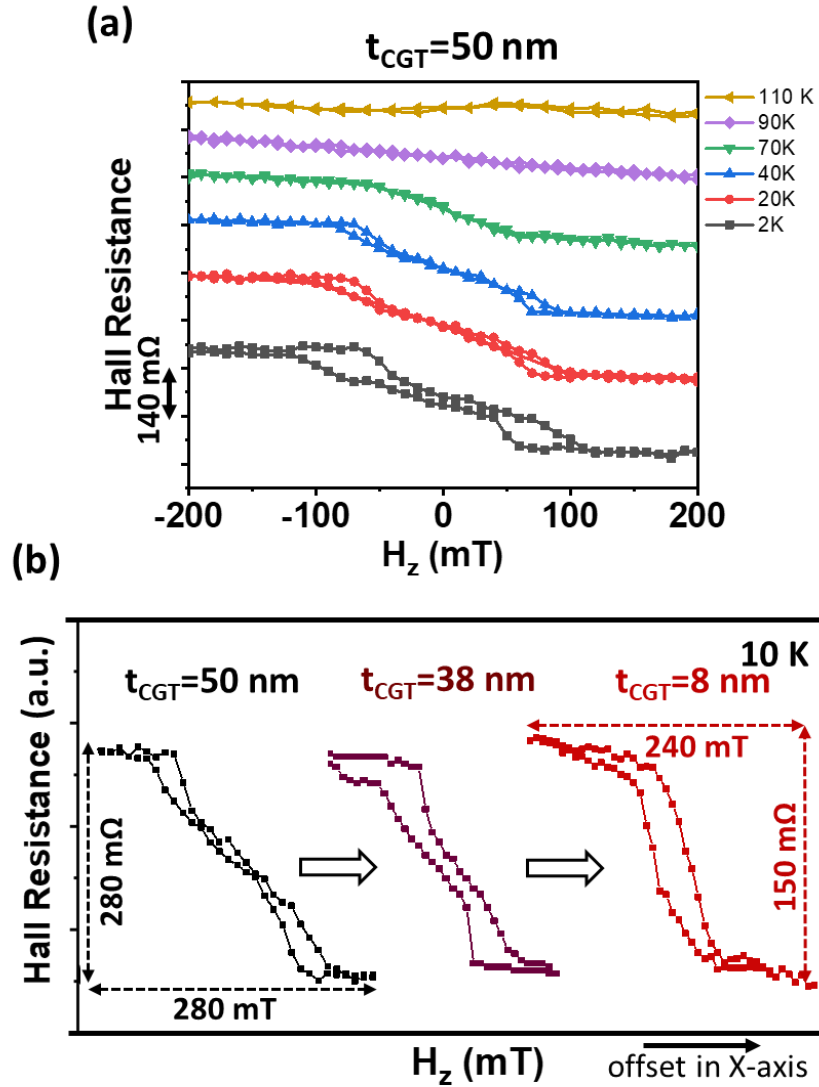
Figure 6.5: (a) Temperature dependent Hall resistance of the Hall bar device consisting 50 nm thick CGT with out-of-plane magnetic field. Anomalous Hall effect start to emerge around 70 K, near Curie temperature of CGT. (b) Normalized R_{AHE} of for three different thicknesses of CGT. © 2020 WILEY-VCH Verlag GmbH & Co. KGaA, Weinheim.

lithography and lift-off process. Figure 6.4(a) shows the measurement set-up and a representative optical image of a device. Temperature dependent Hall resistance measurements under out-of-plane (oop) magnetic fields (H_z) were performed using an excitation AC current (I_{ac}) of 10 uA and a lock-in set-up. Raman spectroscopy data were gathered to confirm the quality of the CGT films. Unlike the Raman spectra reported previously for CGT FETs, which were exposed to air [93], the Raman spectra of our CGT/Ta Hall bar devices (with 50 nm CGT) show sharp peaks at approximately 112 cm^{-1} and 138 cm^{-1} (see Figure 6.4(b)), consistent with previously reported Raman spectra on single crystal CGT [94][95]. The surface roughness of the fabricated devices is in the sub-nanometer range (Figure 6.4(c)) even after the Ta deposition, further highlighting the process control achieved. Figure 6.5(a) shows the Hall resistance versus H_z for a Hall bar device from a 50 nm thick CGT flake. As apparent from fig. 6.5(a), the anomalous Hall resistance (R_{AHE}), i.e. the out-of-plane magnetization (m_z) starts to emerge at around 70 K, near the expected Curie temperature of CGT[88][96]. Lower temperatures result in a larger hysteresis. However, even at 2K the magnetization remanence remains almost zero. Similar measurements were performed on devices from thinner CGT films (t_{CGT}). Normalized R_{AHE} curves at 10 K for t_{CGT} = 50 nm, 38 nm and 8 nm are displayed in Figure 6.5(d). If compared with the CGT (50 nm)/Ta heterostructure (device #1), the R_{AHE} of a CGT (38 nm)/Ta heterostructure (device #2) and a CGT (8 nm)/Ta heterostructure (device #3) show progressively larger remanences with a much squarer shaped hysteresis as expected for a magnet with perpendicular magnetic anisotropy (PMA). Such thickness dependent magnetization curves have been observed previously using MOKE [88] and are here obtained using electrical measurements similar to [92].

6.3   SOT switching of CGT

Having demonstrated the PMA behavior of thin CGT flakes at low temperatures, we are in a position to explore the feasibility of SOT switching by means of currents through the Ta-layer in contact with the semiconducting magnet. When current is passed through a heavy metal that exhibits GSHE such as Ta using a configuration as displayed in Figure 6.6(a), spins generated at the interface are oriented in the y-direction and hence on their own cannot deterministically switch m_z due to symmetry reasons. However, an in-plane magnetic field applied along the current direction (H_x) can break the symmetry of the system and spin orbit torque can be utilized to deterministically switch m_z in this case. Hence, when the magnetic field is swept in the current

direction (H_x) in the presence of a negative or positive DC current a clockwise or counterclockwise hysteresis loop of m_z results respectively [31][97] analogous to a charge current sweep under positive or negative magnetic fields H_x [16]. On the other hand, the same charge currents are not expected to result in any hysteresis loop if a magnetic field H_y is applied perpendicular to the current direction for our PMA magnet with its magnetization in the z-direction. Last, a current polarity independent hysteresis loop is expected if a magnetic field H_z is swept, a field that is in the same direction as the magnetization of the PMA magnet.

Exactly these three sets of experiments are displayed in Figure 6.6(b), (c) and (d). The Hall resistance of device #3 (AFM image is shown in Figure 6.6(a)) was measured at 10K with an I_{ac}=4 uA, using a lock-in set-up in the presence of DC currents (I_{dc}) of different magnitude and polarization. Magnetic fields are swept in the x-, y-, and z-direction respectively as discussed above. The observed behavior is largely consistent with the expressed expectations under different magnetic field and charge current conditions. As shown in Figure 6.6(c), while sweeping H_x, R_{AHE} (i.e. m_z) switching loops are observed even in the absence of H_z and the polarity of the switching loops is reversed between I_{dc}=+100 uA and −100 uA. Note that the counterclockwise and clockwise switching under positive and negative charge currents, respectively, is opposite compared to Ta/CoFeB [16] and W/CoFeB [98] systems due to an inversion of the stacking sequence of HM and FM layers. Our observations are also consistent with the observed SOT switching in a $Tm_3Fe_5O_{12}$/Tungsten (TMIG/W) heterostructure as reported before [9], since W in their experiments and Ta in our experiments exhibit a spin Hall angle with the same polarity. On the other hand, no such R_{AHE} loops are observed while sweeping H_y (Figure 6.6(d)).
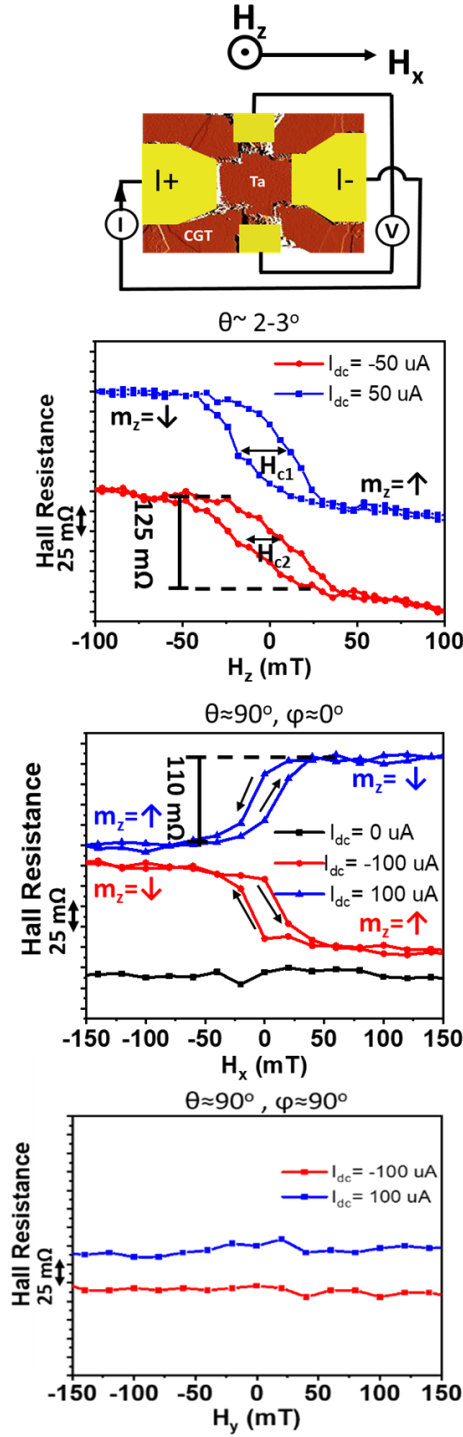
Figure 6.6: (a) AFM image of device #3 (b) Hall resistance versus H_z measured at I_{ac}= 4 uA using a lock-in set-up for I_{dc}=+/-50 uA. (c) Hall resistance versus H_x measured at I_{ac} = 4 uA using a lock-in set-up for I_{dc}=+/-100 uA. (d) Hall resistance versus H_x measured ath I_{ac}= 4 uA using a lock-in set-up for I_{dc}= +/-100 uA. All measurements were performed at 10K. © 2020 WILEY-VCH Verlag GmbH & Co. KGaA, Weinheim.

Moreover, while we do not observe a change in the polarity of hysteresis loop when scanning H_z under different current polarities, we did notice a change of the coercive field under these two different DC currents. This effect has been discussed before in references [16] and [17] that attribute their observation to a slight misalignment of the external magnetic field relative to the intended z-orientation. A small misalignment of $\theta \sim 2\text{-}3^o$ that results in a small magnetic field component in the x-direction (which is unintentional in our custom-built probe for the PPMS system) is sufficient to explain the change in coercivity. Such a change in coercivity is a manifestation of damping-like torque which is expected from the GSHE in 5 nm thick Ta films. We have estimated the spin-orbit field of the heterostructure using this coercivity change for +50 and -50 uA, based on the method described in ref [31][97]. In general, to study effective SOT fields in metallic bilayers of HM/FM stacks under excitation of AC currents (I_w), the second harmonic of the Hall voltage (V_{2w}) is measured. However, for our HM/insulating-FM system
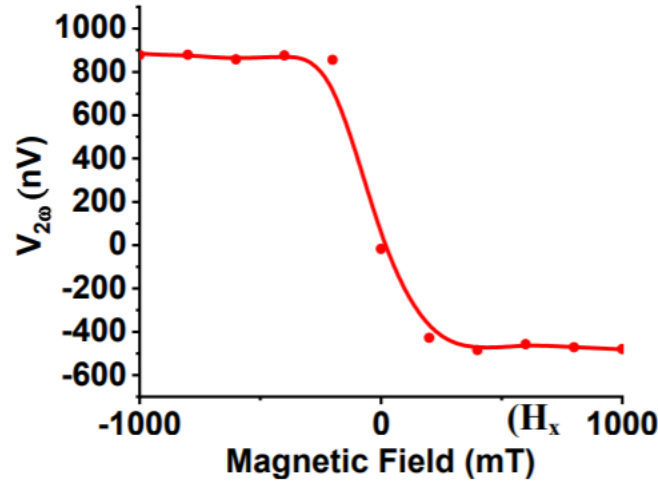
Figure 6.7: In-plane magnetic field dependence of second harmonic of Hall voltage.

comparatively large thermoelectric effects such as the spin Seebeck effect dominate V_{2w}. This is the reason why we observe in our heterostructure a sigmoidal shape of V_{2w} with respect to an in-plane magnetic field (H_x) (Figure 6.7), similar to what has been previously reported for a TMIG/Pt system [99]. Such a sigmoidal dependence is expected due to larger spin Seebeck effect compared to the signal generated from effective SOT fields in our heterostructure. Note that the presence of contributions from thermoelectric effects does not imply the absence of contributions from

effective spin-torque fields. However, distinguishing these two components is challenging due to the magnitude of the thermoelectric effects in our sample.
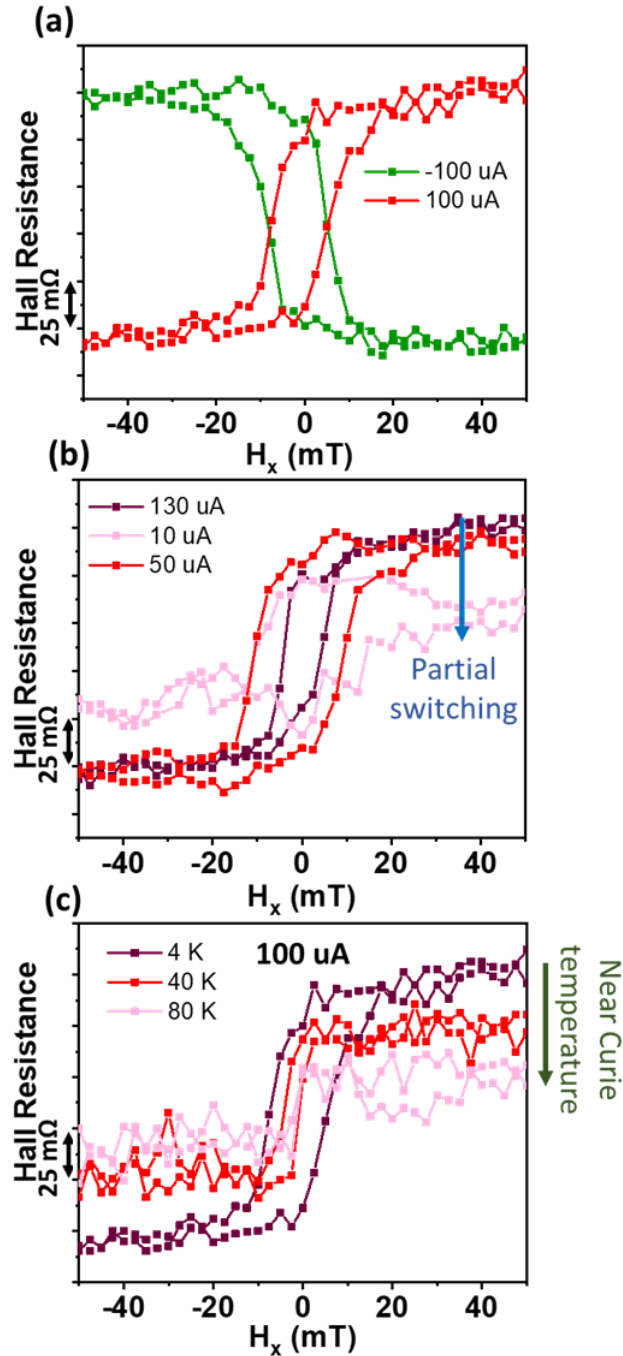
Figure 6.8: (a) Field assisted SOT switching of out-of-plane magnetization with I_{dc}= +/- 100 uA at 4K. (b) I_{dc} dependent field assisted SOT switching at 4K. (c) Temperature dependent field assisted SOT switching at T=4 K, 40 K and 80 K. © 2020 WILEY-VCH Verlag GmbH & Co. KGaA, Weinheim.

Hence, we have focused our experiments on the direct observation of SOT switching rather than analyzing effective SOT fields. The sum of these experimental findings unambiguously proves the successful SOT switching in a Ta/CGT heterostructure that is reported here for the first time. Next, we are interested in exploring how efficient the charge-to-spin conversion in our Ta/CGT stacks is in comparison to the reported SOT switching in other heterostructures. Figure 6.8 shows device characteristics of yet another Ta/CGT device. As in the case discussed in the context of Figure 6.5(c), clear SOT switching with the expected reversal of the hysteresis loop is observed in Figure 6.8(a) when sweeping H_x under positive and negative charge current polarities at 4K. Moreover, as expected from previous studies [91], higher charge currents require smaller H_x and vice versa to change the magnetization of our CGT magnet with PMA (see Figure 6.7(b)). Note that too small I_{dc}-values result in incomplete (partial) reversal of the magnetization direction since in a large FM with a size of a few μm^2, such as in our experiment, SOT switching is driven by domain nucleation [64][65][102]. To further evaluate the SOT switching, we have also characterized device#4 for temperatures of 40K and 80 K. Since the magnetization switching of our micro-scale device is a thermally assisted process (along with a lowered magnetic anisotropy at higher temperatures), we expect easier magnetization switching, i.e. lower in-plane fields required for switching at higher temperatures. This behavior is observed in Figure 6.8(c) for a constant current of 100 uA. At 80 K, a negligible R_{AHE} loop is observed due to the loss of ferromagnetism near the Curie temperature of CGT.

Plotting the actual I_{dc} and critical H_x-fields for complete switching allows creating a switching phase diagram – Figure 6.9(a) that shows the typical diamond shape [98]. Current and magnetic field value pairs outside the diamond guarantee SOT switching. In the presence of an in-plane field of approximately 20 mT an I_{dc}-value of 50 uA, which corresponds to a current density of around $5*10^5$ A/cm^2 is sufficient to switch m_z. Fig. 6.9(b) puts our experimental findings on SOT switching into the context of previously reported data on other hetero stacks. It is apparent that metallic heavy metal/ ferromagnet (HM/FM) heterostructures such as Ta/CoFeB [16] or Pt/FGT [103][104] require in general high critical current densities of around 10^7 A/cm^2 for field-assisted SOT switching as a result of current shunting through the magnet and large M_s-values of the magnets used. On the other hand, integration of insulating FMs such as TMIG [90] or usage of TI
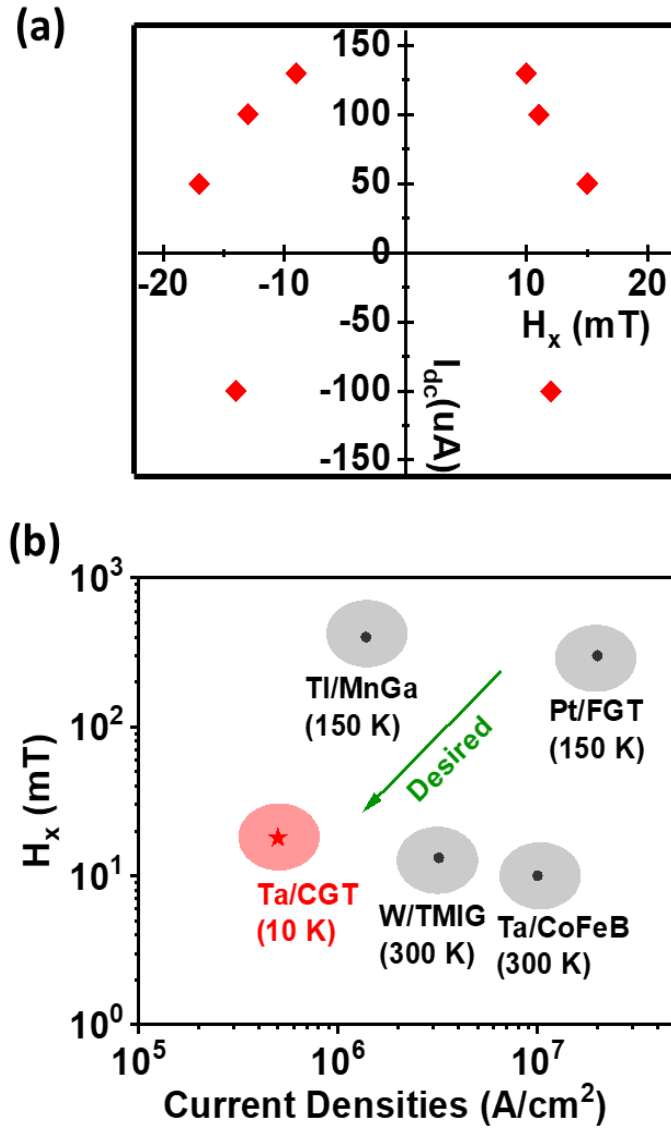
Figure 6.9: (a) Phase diagram of m_z for applied I_{dc} and H_x. (b) Required current densities and in-plane fields for SOT switching of previously reported magnetic heterostructure. © 2020 WILEY-VCH Verlag GmbH & Co. KGaA, Weinheim.

as GSHE material that exhibits large spin Hall angles [31] can reduce the required critical current densities to ~10^6 A/cm^2. Here, using semiconducting 2D-FM CGT, we have shown that even lower critical current densities of ~$5*10^5$ A/cm^2 can be sufficient for field-assisted SOT switching. Low coercivity and remanence in the magnetization loops of CGT films (Figure 6.4(b)) suggest that domain nucleation is easier for CGT films if compared to ferromagnets such as CoFeB or TMIG

which show sharp switching at coercivity. We believe that this could be one of the possible reasons for the low current densities required for SOT switching in our experiments. However, out-of-plane fields required for magnetization saturation are not small (around 50 mT as shown in fig. 6.5(b)) which suggest even though nucleation is easier, SOT switching of total magnetization would require substantial effective fields and further investigation is required to understand SOT switching mechanism in these micron-scale devices.

7. SUMMARY

This thesis presents experimental demonstrations of novel spin devices essential building blocks for implementation of Probabilistic Spin Logic (PSL) [4, 101] to solve a wide variety of problems such as pattern recognition, optimization, Bayesian inference etc. First, we experimentally demonstrated a new type of stochastic spin device with unique properties such as a current controlled probabilistic binary output and input-output isolation. Essentially, such device is a Binary Stochastic Neuron (BSN) also referred to as a p-bit in the context of PSL. Using these stochastic spin devices, we built a directed network in which the probability of the output node is a function of the input node and the weighted connection between them. This experimental demonstration shows the potential of stochastic spin devices as building blocks for PSL i.e. networks with probabilistic outcomes.

Next, device components required for PSL namely p-bits and weighted interconnects are realized using devices similar to the ones used in Magnetic Random Access Memory (MRAM) technology. We have used random telegraphic hopping of magnetization in low barrier in-plane MTJ to generate binary random numbers. In a spin-orbit torque (SOT)-MRAM type device, we have shown that SOTs can tune magnetization hopping of low barrier MTJ, creating a compact tunable random number generator (RNG). Such 3-terminal SOT device additionally provide decoupled input & output paths and hence satisfies all the requirements of p-bits. P-bits can also be built simply by combining a low barrier MTJ with a transistor closely resembling the 1T/MTJ structure commonly used for STT-MRAM applications. The individual modules for such p-bit – a MTJ with high TMR and 2D transistor with desired ON/OFF currents – were fabricated and integrated on same chip. It was also shown that annealing time used during fabrication of MTJs can tune the magnetic anisotropy of MTJs to achieve low barrier required for p-bits. We also proposed and experimentally demonstrated a new SOT-MRAM based compound synapse which can be used as a weighted interconnect in PSL. In this synapse, we used stochastic spin–orbit-torque (SOT) switching of an ensemble of stable nanomagnets that are located on one shared spin Hall effect (SHE) material channel (Ta) to mimic synaptic behavior i.e. potentiation and depression. Total magnetization of the ensemble shows a gradual increase (potentiation) or decrease (depression) when subjected to series of input SOT pulses. By using a properly chosen pulse scheme, we are able to demonstrate linear potentiation and depression in the synapse, as required

for many neuromorphic architectures. Circuit simulations of deep belief network (DBN) consisting of p-bits based neurons and compound synapses show capabilities of performing pattern recognition tasks on MINIST datasets.

Finally, we have explored novel 2-Dimensional Ferromagnets (2D-FMs) for their applications in future spintronics devices. In conclusion, by integrating semiconducting 2D-FMs and HMs with high SOC, we have demonstrated strong spin-orbit torque effects in CGT/Ta heterostructures. We have experimentally demonstrated that out-of-plane magnetization of CGT can be manipulated by flowing a charge current through Tantalum, in the presence of an in-plane magnetic field. Current densities as low as $5*10^5$ A/cm2 are sufficient for SOT switching in the presence of in-plane fields of 20 mT. Spin-torque switching as demonstrated here along with the previously explored gate voltage manipulation of 2D semiconducting FMs may enable novel van der Waals heterostructures for the realization of novel low power spintronic devices for memory and logic applications.

REFERENCES

[1]   S. E. Thompson and S. Parthasarathy, "Moore's law: the future of Si microelectronics," *Mater. Today*, vol. 9, no. 6, pp. 20–25, 2006.

[2]   Samuel K. Moore, "Another Step Toward the End of Moore's Law," *IEEE Spectrum,* pp. 9–10, 2019.

[3]   M. Waldrop, "More than moore," *Nature*, vol. 530, p. 145, 2016.

[4]   D. Reinsel, J. Gantz, and J. Rydning, "The Digitization of the World - From Edge to Core," *Fram. Int. Data Corp.*, vol. 2018, no. November, p. US44413318, 2018.

[5]   D. Reinsel, J. Gantz, and J. Rydning, "The Digitization of the World from Edge to Core," *Int. Data Corp. Rep.*, no. November, 2018.

[6]   M. I. Jordan and T. M. Mitchell, "Machine learning: Trends, perspectives, and prospects," vol. 349, no. 6245, 2015.

[7]   J. Von Neumann, *The computer and the brain*. Yale University Press, 2012.

[8]   EDITORIAL, "Big data needs a hardware revolution," *Nature*, vol. 541, pp. 133–134, 2015.

[9]   S. Khoram, Y. Zha, J. Zhang, and J. Li, "Challenges and opportunities: From near-memory computing to in-memory computing," *Proc. Int. Symp. Phys. Des.*, vol. Part F1271, pp. 43–46, 2017.

[10]   and J. C. M. N. Baibich, J. M. Broto, A. Fert, F. Nguyen Van Dau, F. Petroff, P. Etienne, G. Creuzet, A. Friederich, "Giant Magnetoresistance of (001)Fe/(001)Cr Magnetic Superlattices," *Phys. Rev. Lett.*, vol. 61, no. 001, pp. 2472–2475, 1988.

[11]   S. Datta and B. Das, "Electronic analog of the electro-optic modulator," *Appl. Phys. Lett.*, vol. 56, no. 7, pp. 665–667, 1990.

[12]   M. Bowen *et al.*, "Large magnetoresistance in Fe/MgO/FeCo(001) epitaxial tunnel junctions on GaAs(001)," *Appl. Phys. Lett.*, vol. 79, no. 11, pp. 1655–1657, 2001.

[13]   M. Gajek *et al.*, "Spin torque switching of 20 nm magnetic tunnel junctions with perpendicular anisotropy," *Appl. Phys. Lett.*, vol. 100, no. 13, pp. 1–4, 2012.

[14]   S. Ikeda *et al.*, "A perpendicular-anisotropy CoFeB-MgO magnetic tunnel junction," *Nat. Mater.*, vol. 9, no. 9, pp. 721–724, 2010.

[15]   S. Bhatti, R. Sbiaa, A. Hirohata, H. Ohno, S. Fukami, and S. N. Piramanayagam, "Spintronics based random access memory: a review," *Mater. Today*, vol. 20, no. 9, pp. 530–548, 2017.

[16] L. Liu *et al.*, "Spin-Torque Switching with the Giant Spin Hall Effect of Tantalum," *Science (80-.).*, vol. 336, pp. 555–558, 2012.

[17] A. Sengupta and K. Roy, "Encoding neural and synaptic functionalities in electron spin: A pathway to efficient neuromorphic computing," *Appl. Phys. Rev.*, vol. 4, no. 4, 2017.

[18] K. Y. Camsari *et al.*, "From Charge to Spin and Spin to Charge: Stochastic Magnets for Probabilistic Switching," *Proc. IEEE*, vol. 108, no. 8, pp. 1322–1337, 2020.

[19] R. Zand, K. Y. Camsari, S. Datta, and R. F. Demara, "Composable Probabilistic Inference Networks Using MRAM-based Stochastic Neurons," *arXiv*, vol. 15, no. 2, 2018.

[20] B. Sutton, K. Y. Camsari, B. Behin-aein, and S. Datta, "Intrinsic optimization using stochastic nanomagnets," *Sci. Rep.*, vol. 7, 2017.

[21] R. Faria, K. Y. Camsari, and S. Datta, "Implementing Bayesian networks with embedded stochastic MRAM," *AIP Adv.*, vol. 8, no. March 2018, p. 045101, 2018.

[22] K. Y. Camsari, R. Faria, B. M. Sutton, and S. Datta, "Stochastic p-bits for invertible logic," *Phys. Rev. X*, vol. 7, no. 3, pp. 1–19, 2017.

[23] K. Y. Camsari, S. Salahuddin, and S. Datta, "Implementing p-bits with Embedded MTJ," *IEEE Electron Device Lett.*, vol. 38, no. 12, pp. 1767–1770, 2017.

[24] O. Hassan, R. Faria, K. Y. Camsari, J. Z. Sun, and S. Datta, "Low barrier magnet design for efficient hardware binary stochastic neurons," *IEEE Magn. Lett.*, vol. 10, p. 4502805, 2019.

[25] J. Kaiser, A. Rustagi, K. Y. Camsari, J. Z. Sun, S. Datta, and P. Upadhyaya, "Subnanosecond Fluctuations in Low-Barrier Nanomagnets," *arXiv*, vol. 10, no. 1, p. 1, 2019.

[26] M. Cubukcu *et al.*, "SOT-MRAM 300mm integration for low power and ultrafast embedded memories K.," *IEEE Trans. Magn.*, vol. 54, no. 4, pp. 81–82, 2018.

[27] D. Zhang *et al.*, "Energy-efficient neuromorphic computation based on compound spin synapse with stochastic learning," *Proc. - IEEE Int. Symp. Circuits Syst.*, vol. 2015–July, pp. 1538–1541, 2015.

[28] A. Mondal and A. Srivastava, "In-situ Stochastic Training of MTJ Crossbar based Neural Networks," *Proc. Int. Symp. Low Power Electron. Des.*, p. 51, 2018.

[29] & A. J. Ostwal, Vaibhav, Zand Ramtin, DeMara Ron, "A Novel Compound Synapse Using Probabilistic Spin–Orbit-Torque Switching for MTJ-Based Deep Neural Networks," *IEEE J. Explor. Solid-State Comput. Devices Circuits Receiv.*, vol. 5.2, no. September 2019, pp. 182–187, 2020.

[30] A. Hirohata, W. Frost, M. Samiepour, and J. Y. Kim, "Perpendicular magnetic anisotropy in Heusler alloy films and their magnetoresistive junctions," *Materials (Basel).*, vol. 11, no. 1, pp. 1–18, 2018.

[31] H. D. K. Nguyen, U. Yugo, and N. H. Pham, "A conductive topological insulator with large spin Hall effect for ultralow power spin–orbit torque switching," *Nat. Mater.*, vol. 17, pp. 808–813, 2018.

[32] C. Song, B. Cui, F. Li, X. Zhou, and F. Pan, "Recent progress in voltage control of magnetism: Materials, mechanisms, and performance," *Prog. Mater. Sci.*, vol. 87, pp. 33–82, 2017.

[33] C. Gong *et al.*, "Discovery of intrinsic ferromagnetism in two-dimensional van der Waals crystals," *Nature*, vol. 546, pp. 265–269, 2017.

[34] E. Barré *et al.*, "Spatial Separation of Carrier Spin by the Valley Hall Effect in Monolayer WSe2 Transistors," *Nano Lett.*, 2019.

[35] W. Yan *et al.*, "Long Spin Diffusion Length in Few-Layer Graphene Flakes," *Phys. Rev. Lett.*, vol. 117, no. 14, pp. 1–6, 2016.

[36] RadisavljevicB *et al.*, "Single-layer MoS2 transistors," *Nat. Nanotechnol.*, vol. 6, no. 3, pp. 147–150, 2011.

[37] S. B. Desai *et al.*, "MoS2 transistors with 1-nanometer gate lengths," *Science (80-.).*, vol. 354, no. 6308, pp. 99–102, 2016.

[38] F. Zhang *et al.*, "Electric-field induced structural transition in vertical MoTe 2 - and Mo 1– x W x Te 2 -based resistive memories," *Nat. Mater.*, vol. 18, no. 1, pp. 55–61, 2019.

[39] T. Song *et al.*, "Giant tunneling magnetoresistance in spin-filter van der Waals heterostructures," *Science (80-.).*, vol. 360, no. 6394, pp. 1214–1218, 2018.

[40] F. Liu *et al.*, "Room-temperature ferroelectricity in CuInP 2 S 6 ultrathin flakes," *Nat. Commun.*, vol. 7, pp. 1–6, 2016.

[41] M. Bonilla *et al.*, "Strong roomerature ferromagnetism in VSe2 monolayers on van der Waals substrates," *Nat. Nanotechnol.*, vol. 13, no. 4, pp. 289–293, 2018.

[42] C. Gong *et al.*, "Discovery of intrinsic ferromagnetism in two-dimensional van der Waals crystals," *Nature*, vol. 546, no. 7657, pp. 265–269, 2017.

[43] B. Huang *et al.*, "Layer-dependent ferromagnetism in a van der Waals crystal down to the monolayer limit," *Nature*, vol. 546, no. 7657, pp. 270–273, 2017.

[44] Z. Fei *et al.*, "Two-dimensional itinerant ferromagnetism in atomically thin Fe3GeTe2," *Nat. Mater.*, vol. 17, no. 9, pp. 778–782, 2018.

[45] Z. Zhang, J. Shang, C. Jiang, A. Rasmita, W. Gao, and T. Yu, "Direct Photoluminescence Probing of Ferromagnetism in Monolayer Two-Dimensional CrBr 3," *Nano Lett.*, vol. 19, no. 5, pp. 3138–3142, 2019.

[46] S. Wu *et al.*, "The direct observation of ferromagnetic domain of single crystal CrSiTe3," *AIP Adv.*, vol. 8, no. 5, pp. 1–6, 2018.

[47] Y. P. F. & G. E. Ivan A. Verzhbitskiy, Hidekazu Kurebayashi, Haixia Cheng, Jun Zhou, Safe Khan, "Controlling the magnetic anisotropy in Cr2Ge2Te6 by electrostatic gating," *Nat. Electron.*, vol. 3, pp. 460–465, 2020.

[48] Z. Wang, D. Sapkota, T. Taniguchi, K. Watanabe, D. Mandrus, and A. F. Morpurgo, "Tunneling Spin Valves Based on Fe3GeTe2/hBN/Fe3GeTe2 van der Waals Heterostructures," *Nano Lett.*, vol. 18, no. 7, pp. 4303–4308, 2018.

[49] S. Jiang, L. Li, Z. Wang, J. Shan, and K. F. Mak, "Spin tunnel field-effect transistors based on two-dimensional van der Waals heterostructures," *Nat. Electron.*, vol. 2, no. 4, pp. 159–163, 2019.

[50] X. Li, J. T. Lü, J. Zhang, L. You, Y. Su, and E. Y. Tsymbal, "Spin-Dependent Transport in van der Waals Magnetic Tunnel Junctions with Fe3GeTe2 Electrodes," *Nano Lett.*, vol. 19, no. 8, pp. 5133–5139, 2019.

[51] V. Ostwal, P. Debashis, R. Faria, Z. Chen, and J. Appenzeller, "Spin-torque devices with hard axis initialization as Stochastic Binary Neurons," *Sci. Rep.*, vol. 8, no. 1, pp. 1–8, 2018.

[52] V. Quang Diep, B. Sutton, B. Behin-Aein, and S. Datta, "Spin switches for compact implementation of neuron and synapse," *Appl. Phys. Lett.*, vol. 104, no. 22, 2014.

[53] Y. Shim, S. Chen, A. Sengupta, and K. Roy, "Stochastic Spin-Orbit Torque Devices as Elements for Bayesian Inference," *Sci. Rep.*, vol. 7, no. 1, pp. 1–9, 2017.

[54] R. Faria, K. Y. Camsari, and S. Datta, "Implementing Bayesian networks with embedded stochastic MRAM," *AIP Adv.*, vol. 8, no. 4, 2018.

[55] B. Behin-Aein, V. Diep, and S. Datta, "A building block for hardware belief networks," *Sci. Rep.*, vol. 6, no. July, pp. 1–10, 2016.

[56] Y. Shim, A. Jaiswal, and K. Roy, "Ising computation based combinatorial optimization using spin-Hall effect (SHE) induced stochastic magnetization reversal," *J. Appl. Phys.*, vol. 121, no. 19, 2017.

[57] P. Debashis, R. Faria, K. Y. Camsari, J. Appenzeller, S. Datta, and Z. Chen, "Experimental demonstration of nanomagnet networks as hardware for Ising computing," *Tech. Dig. - Int. Electron Devices Meet. IEDM*, p. 34.3.1-34.3.4, 2017.

[58] K. Y. Camsari, R. Faria, B. M. Sutton, and S. Datta, "Stochastic p-bits for invertible logic," *Phys. Rev. X*, vol. 7, 2017.

[59]   D. Vodenicarevic *et al.*, "Low-Energy Truly Random Number Generation with Superparamagnetic Tunnel Junctions for Unconventional Computing," *Phys. Rev. Appl.*, vol. 8, no. 5, pp. 1–9, 2017.

[60]   A. Mizrahi *et al.*, "Neural-like computing with populations of superparamagnetic basis functions," *Nat. Commun.*, vol. 9, no. 1, pp. 1–11, 2018.

[61]   M. Bapna and S. A. Majetich, "Current control of time-averaged magnetization in superparamagnetic tunnel junctions," *Appl. Phys. Lett.*, vol. 111, no. 24, 2017.

[62]   M. Sharad, C. Augustine, G. Panagopoulos, and K. Roy, "Spin-Based Neuron Model with Domain Wall Magnets as Synapse," *IEEE Trans. Nanotechnol.*, vol. 11, no. c, pp. 843–853, 2012.

[63]   L. Liu, C. Pai, Y. Li, H. W. Tseng, D. C. Ralph, and R. A. Buhrman, "Spin-Torque Switching with the Giant Spin Hall Effect of Tantalum," *Science (80-.).*, vol. 336, pp. 555–559, 2012.

[64]   I. M. Miron *et al.*, "Perpendicular switching of a single ferromagnetic layer induced by in-plane current injection.," *Nature*, vol. 476, pp. 189–193, 2011.

[65]   Y. Kim, X. Fong, and K. Roy, "Spin-Orbit-Torque-Based Spin-Dice : A True Random-Number Generator," *IEEE Magn. Lett.*, vol. 6, pp. 1–4, 2015.

[66]   D. Bhowmik, L. You, and S. Salahuddin, "Spin hall effect clocking of nanomagnetic logic without a magnetic field," *Nat. Nanotechnol.*, vol. 9, pp. 59–63, 2014.

[67]   V. Ostwal, A. Penumatcha, Y. M. Hung, A. D. Kent, and J. Appenzeller, "Spin-orbit torque based magnetization switching in Pt/Cu/[Co/Ni]5multilayer structures," *J. Appl. Phys.*, vol. 122, no. 21, 2017.

[68]   L. E. Bassham *et al.*, "A statistical test suite for random and pseudorandom number generators for cryptographic applications," *Spec. Publ. (NIST SP) - 800-22 Rev 1a*, 2010.

[69]   A. Fukushima *et al.*, "Spin dice: A scalable truly random number generator based on spintronics," *Appl. Phys. Express*, vol. 7, no. 8, 2014.

[70]   W. Scott, D. E. Nikonov, J. Jeffrey, I. A. Young, and B. Heard, "Hybrid Piezoelectric-Magnetic Neurons : A Proposal for Energy- Efficient Machine Learning," *Proc. ACMSE 2018 Conf. ACM.*, pp. 3–7, 2018.

[71]   A. Sengupta, S. H. Choday, Y. Kim, and K. Roy, "Spin orbit torque based electronic neuron," *Appl. Phys. Lett.*, vol. 106, no. 14, p. 143701, 2015.

[72]   K. Kim, J. Kim, J. Yu, J. Seo, J. Lee, and K. Choi, "Dynamic energy-accuracy trade-off using stochastic computing in deep neural networks," *Proc. 53rd Annu. Des. Autom. Conf. - DAC '16*, no. 1, pp. 1–6, 2016.

[73] V. Ostwal and J. Appenzeller, "Spin-Orbit Torque-Controlled Magnetic Tunnel Junction with Low Thermal Stability for Tunable Random Number Generation," *IEEE Magn. Lett.*, vol. 10, 2019.

[74] Y. M. Lee, J. Hayakawa, S. Ikeda, F. Matsukura, and H. Ohno, "Giant tunnel magnetoresistance and high annealing stability in CoFeB/MgO/CoFeB magnetic tunnel junctions with synthetic pinned layer," *Appl. Phys. Lett.*, vol. 89, 2006.

[75] A. V Penumatcha *et al.*, "Spin-torque switching of a nano-magnet using giant spin hall effect Spin-torque switching of a nano-magnet using giant spin hall effect," *AIP Adv.*, vol. 5, 2015.

[76] J. Z. Sun, "Spin-current interaction with a monodomain magnetic body: A model study," *Phys. Rev. B*, vol. 62, pp. 570–578, 2000.

[77] M. Bapna and S. A. Majetich, "Current control of time-averaged magnetization in superparamagnetic tunnel junctions," *Appl. Phys. Lett.*, vol. 111, 2018.

[78] M. Cecot *et al.*, "Influence of intermixing at the Ta/CoFeB interface on spin Hall angle in Ta/CoFeB/MgO heterostructures," *Sci. Rep.*, vol. 7, 2017.

[79] S. V. Aradhya, G. E. Rowlands, J. Oh, D. C. Ralph, and R. A. Buhrman, "Nanosecond-Timescale Low Energy Switching of In-Plane Magnetic Tunnel Junctions through Dynamic Oersted-Field-Assisted Spin Hall Effect," *Nano Lett.*, vol. 16, pp. 5987–5992, 2016.

[80] C. Shannon, "A mathematical theory of communication," *Bell Syst. Tech. J.*, vol. XXVII, 1948.

[81] W. F. Brown, "Thermal fluctuations of a single-domain particle," *Phys. Rev.*, vol. 34, 1963.

[82] J. Bill and R. Legenstein, "A compound memristive synapse model for statistical learning through STDP in spiking neural networks," *Front. Neurosci.*, vol. 8, no. DEC, pp. 1–18, 2014.

[83] E. Vianello *et al.*, "HfO$_2$-Based OxRAM Devices as Synapses for Convolutional Neural Networks," *IEEE Trans. Electron Devices*, vol. 62, no. 8, pp. 2494–2501, 2015.

[84] D. Zhang *et al.*, "All Spin Artificial Neural Networks Based on Compound Spintronic Synapse and Neuron," *IEEE Trans. Biomed. Circuits Syst.*, vol. 10, no. 4, pp. 828–836, 2016.

[85] C. Gamrat *et al.*, "Spin-Transfer Torque Magnetic Memory as a Stochastic Memristive Synapse for Neuromorphic Systems," *IEEE Trans. Biomed. Circuits Syst.*, vol. 9, no. 2, pp. 166–174, 2015.

[86] D. Zhang, L. Zeng, and J.-O. Klein, "Stochastic Spintronic Device based Synapses and Spiking Neurons for Neuromorphic Computation," *IEEE/ACM Int. Symp. Nanoscale Archit.*, pp. 173–178, 2016.

[87]   V. Ostwal, T. Shen, and J. Appenzeller, "Efficient Spin-Orbit Torque Switching of the Semiconducting Van Der Waals Ferromagnet Cr2Ge2Te6," *Adv. Mater.*, vol. 32, no. 7, pp. 1–7, 2020.

[88]   Z. Wang *et al.*, "Electric-field control of magnetism in a few-layered van der Waals ferromagnetic semiconductor," *Nat. Nanotechnol.*, vol. 13, pp. 554–559, 2018.

[89]   T. Guo *et al.*, "Multiple structure and symmetry types in narrow temperature and magnetic field ranges in two-dimensional Cr2Ge2Te6 crystal," *arXiv*, p. 1803.06113, 2018.

[90]   Q. Shao *et al.*, "Role of dimensional crossover on spin-orbit torque efficiency in magnetic insulator thin films," *Nat. Commun.*, vol. 9, p. 3612, 2018.

[91]   C. O. Avci *et al.*, "Current-induced switching in a magnetic insulator," *Nat. Mater.*, vol. 16, pp. 309–314, 2017.

[92]   M. Lohmann *et al.*, "Probing Magnetism in Insulating Cr 2 Ge 2 Te 6 by Induced Anomalous Hall Effect in Pt," *Nano Lett.*, vol. 19, pp. 2397–2403, 2019.

[93]   W. Xing *et al.*, "Electric field effect in multilayer Cr 2 Ge 2 Te 6 : a ferromagnetic 2D material," *2D Mater.*, vol. 4, p. 024009, 2017.

[94]   A. Milosavljević *et al.*, "Evidence of spin-phonon coupling in CrSiTe3," *Phys. Rev. B*, vol. 98, no. 10, p. 104306, 2018.

[95]   Y. Tian, H. Ji, R. J. C. L. D. Alegria, J. R. Petta, and K. S. Burch, "Polarized Temperature Dependent Raman Study of Bi2Te3-Cr2Ge2Te6 heterostructure and the Ferromagnetic Insulator Cr2Ge2Te6," *arXiv*, p. 1410.1898, 2014.

[96]   M. Mogi *et al.*, "Ferromagnetic insulator Cr 2 Ge 2 Te 6 thin films with perpendicular remanence," *APL Mater.*, vol. 6, p. 091104, 2018.

[97]   P. Li *et al.*, "Spin-orbit torque-assisted switching in magnetic insulator thin films with perpendicular magnetic anisotropy," *Nat. Commun.*, vol. 7, p. 12688, 2016.

[98]   Q. Hao and G. Xiao, "Giant Spin Hall Effect and Switching Induced by Spin-Transfer Torque in a W/Co40Fe40 B20/MgO Structure with Perpendicular Magnetic Anisotropy," *Phys. Rev. Appl.*, vol. 3, p. 034009, 2015.

[99]   C. O. Avci *et al.*, "Current-induced switching in a magnetic insulator," *Nat. Mater.*, vol. 16, p. 309–314 (supplementary information), 2017.

[100] J. Cao *et al.*, "Spin orbit torques induced magnetization reversal through asymmetric domain wall propagation in Ta/CoFeB/MgO structures," *Sci. Rep.*, vol. 8, no. 1, p. 1355, 2018.

[101] S. Woo, M. Mann, A. J. Tan, L. Caretta, and G. S. D. Beach, "Enhanced spin-orbit torques in Pt/Co/Ta heterostructures," *Appl. Phys. Lett.*, vol. 105, no. 21, p. 212404, 2014.

[102] O. J. Lee *et al.*, "Central role of domain wall depinning for perpendicular magnetization switching driven by spin torque from the spin Hall effect," *Phys. Rev. B - Condens. Matter Mater. Phys.*, vol. 89, no. 2, p. 024418, 2014.

[103] X. Wang *et al.*, "Current-driven magnetization switching in a van der Waals ferromagnet Fe3GeTe2," *arXiv*, p. 1902.05794, 2019.

[104] M. Alghamdi *et al.*, "Highly efficient spin-orbit torque and switching of layered ferromagnet Fe3GeTe2," *arXiv*, p. 1903.00571, 2019.

VITA

Vaibhav Ostwal completed his B.Tech. and M.Tech. degrees in Electrical Engineering with specialization in Microelectronics from Indian Institute of Technology, Bombay in 2015. He received "Outstanding Dual Degree Thesis Award" for his Master's thesis. He then started pursuing doctoral studies in school of Electrical and Computer Engineering at Purdue University, working with Prof. Joerg Appenzeller. His research focuses on the experimental demonstration of novel spin-devices for implementation of unconventional computing. He also works on 2D material-based devices for logic and memory applications. He is a recipient of Bilsland Dissertation Fellowship for Doctoral study. In summer 2018, he worked as a device engineering intern at Western Digital in 3D NAND technology.

PUBLICATIONS

1. V. Ostwal, T. Shen, J. Appenzeller, "Highly efficient spin-orbit switching of semiconducting van der Walls ferromagnet $Cr_2Ge_2Te_6$", Advanced Materials 32.7, 1906021 (2020)

2. T. Shen*, V. Ostwal*, K.Y. Camsari, J. Appenzeller, "Demonstration of a strain-mediated magnetoelectric write and read unit in a $Co_{60}Fe_{20}B_{20}/Pb(Mg_{1/3}Nb_{2/3})_{0.7}Ti_{0.3}O_3$ heterostructure", Nature Scientific Reports, 10.1, 10791 (2020) (*equal contributing authors)

3. P. Debashis*, V. Ostwal*, R. Faria, S. Datta, J. Appenzeller and Z. Chen, "Hardware implementation of Bayesian networks with stochastic spintronic devices", Nature Scientific Reports, 10, 16002 (2020) (*equal contributing authors)

4. K. Camsari, P. Debashis, V. Ostwal, A. Z. Pervaiz, T. Shen, Z. Chen, S. Datta, J. Appenzeller, "From charge to spin and spin to charge: Stochastic magnets for probabilistic switching", Proceedings of the IEEE, 108.8, pp. 1332-1337 (2020)

5. V. Ostwal, R. Zand, R. DeMara, J. Appenzeller, "Novel compound synapse using probabilistic spin-orbit-torque switching for MTJ based deep neural networks", IEEE Journal on Exploratory Solid-State Computational Devices and Circuits 5.2, pp. 192-187 (2019)

6. V. Ostwal and J. Appenzeller, "Spin-orbit torque-controlled magnetic tunnel junction with low thermal stability for tunable random number generation", IEEE Magnetics Letters 10, pp.1-5 (2019)

7. V. Ostwal, P. Debashis, R. Faria, Z. Chen, J. Appenzeller, "Spin-torque devices with hard axis initialization as Stochastic Binary Neurons", Nature Scientific Reports 8.1 (2018), 16689

8. R. Zhou, V. Ostwal, J. Appenzeller, "Vertical versus Lateral Two-Dimensional Heterostructures: On the Topic of Atomically Abrupt p/n-Junctions", Nano letters 17.8, 4787-4792 (2018)

9. V. Ostwal, A. Penumatcha, Y. Hung, A. Kent, J. Appenzeller, "Spin-Orbit Torque based magnetization switching in Pt/Cu/[Co/Ni]*5 multilayer structures", Journal of Applied Physics 122.21, 213905 (2017)